Master of Science Thesis

The Flow Topology of the Ahmed Body in Cross-Wind

An Experimental Investigation
by means of Robotic Volumetric PIV

D. Giaquinta
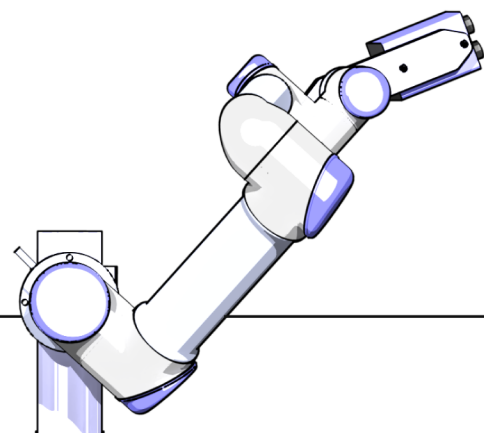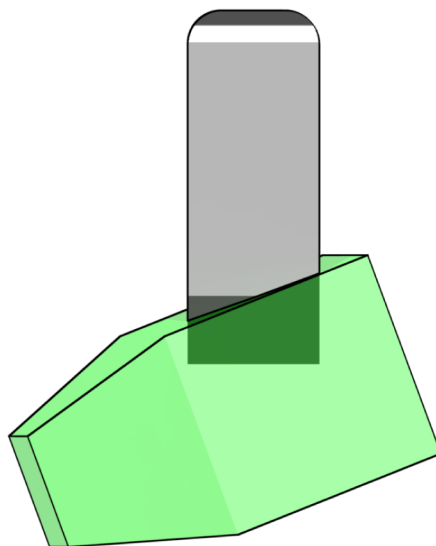
TUDelft

The Flow Topology of the Ahmed Body in Cross-Wind

An Experimental Investigation
by means of Robotic Volumetric PIV

Master of Science Thesis

For obtaining the degree of Master of Science in Aerospace Engineering
at Delft University of Technology

D. Giaquinta

March 23, 2018

Faculty of Aerospace Engineering · Delft University of Technology

Delft University of Technology

DELFT UNIVERSITY OF TECHNOLOGY
DEPARTMENT OF AERODYNAMICS

The undersigned hereby certify that they have read and recommend to the Faculty of Aerospace Engineering for acceptance the thesis entitled **"The Flow Topology of the Ahmed Body in Cross-Wind"** by **D. Giaquinta** in fulfillment of the requirements for the degree of **Master of Science**.

Dated: March 23, 2018

Supervisors:

_____
Dr. Andrea Sciacchitano

_____
Prof.Dr Fulvio Scarano

_____
Prof.Dr.Ing. Georg Eitelberg

_____
Dr. Gandert Van Raemdonck

Preface

As this thesis represents my last challenge as a TU Delft student about to move towards the next chapter of his life, I would like to thank the people whose help contributed to the achievement of this milestone. The past few years, indeed, often tough albeit incredibly rewarding, did considerably contribute to my development, both from a professional and, most importantly, from a personal point of view. Because of this, I am deeply grateful to some of the people I have crossed path with during this journey and to those who always supported me, no matter the distance.

The first person I would like to thank is my supervisor *Dr. Andrea Sciacchitano*. Not only for giving me the opportunity of being involved in such unique project but also for the guidance he always provided me with whenever I needed an advice. Despite these few words cannot do justice to his contribution to the present nine-months work, I am happy to say I consider him the best supervisor I could have wished for. *Edoardo* is the second person who considerably supported me during this work, constantly and patiently providing his impressive technical expertise. I cannot thank him enough for the time he dedicated me but rest assured I will not forget how indispensable his contribution has been. My deepest gratitude goes to *Prof.Dr. Fulvio Scarano* as well, for his enthusiasm, his precious feedback and, among the other things, for trusting me with a thrilling project such as the DNW-Airbus experiment. Among the friends who helped me out before, during and after my experimental campaign I would like to mention *Giggi, Mario, Luca, Jan, Peppe, Frank* and *Stefano*. Moreover, this achievement would have been not possible without the help of *Peter Duyndam, Frits Donker Duyvis, Nico van Beek* and *Colette Russo*.

I would need an entire chapter for describing how essential my new friends "*from Delft*" have been during these years and then, a chapter for each of them to do justice to our friendship. I won't dwell on the unforgettable memories we made together and all the fun we had, let me just say I sincerely would not have made it without your support, and I mean it. Thank you *Fil, Ed* and *Tom* for all the projects we worked on together and the fun we had: we are a great team. Thank you *Dario* for, among the other things, your revised version of "*El mismo sol*". Thank you *Tillini* for your valuable graphic design tips but, most importantly, for your omnipresent smile. Thank you *Argilla* for your positiveness, I never thought I could miss you dancing Britney Spears on a Sunday morning but it actually happened. *Andre, Tea* and *Fra*, thank you for the good time we had together and for always being there, even with the smallest everyday gesture (like a paracetamol pill, *Tea*). Among the friends back home, I would like to mention *Eggi, Nata, Manlio, Chiaretta, Tinki, Germana* and *Serena*: the idea of being back and spending some time together constantly motivated me throughout this journey and gave me the strength to carry on, no matter what.

Moreover, although few lines cannot express the value of a constant and daily support, I

would like to thank my girlfriend *Simo* whom affection, esteem and encouragement did alleviate the stress of the last months, being a priceless contribution to the fulfilment of this achievement.

Finally, I owe a special thank you to my parents for giving me the opportunity to study in Delft and, in particular, to my mother, the most important person in my life, for constantly supporting me in any possible and conceivable way.

Daniele Giaquinta
Delft, March 2018

Abstract

The near wake of the Ahmed reference body in the presence of steady cross-wind is investigated experimentally by means of large-scale three-dimensional Particle Image Velocimetry (PIV). A novel experimental technique is employed which exploits coaxial imaging and illumination while relying on Helium Filled Soap Bubble (HFSB) seeding as well as on robotic actuation. A 50% replica of the Ahmed body with a 25° slant angle is, therefore, considered in different configurations, among which the headwind condition and two different yaw angles, $\beta_1 = +4°$ and $\beta_2 = +8°$. A height-based Reynolds number of 1.15×10^5 is chosen together with an airspeed of 12 m/s and the Open Jet Facility (OJF) Wind Tunnel of TU Delft is employed to perform the experiment.

The relevance of the proposed work lies in the importance of experimental data concerning the Ahmed reference body as well as in the shortage of it with respect to the cross-wind case. The Ahmed body, indeed, once studied to improve the understanding of the flow field generated by road vehicles and to achieve a substantial drag reduction, is nowadays used as Computational Fluid Dynamics (CFD) benchmark and validation tool for automotive applications.

To the best of the author's knowledge, no work is present in the literature which investigates the flow field around the Ahmed body by means of three-dimensional quantitative measurement techniques such as the employed robotic volumetric velocimetry. The proposed study is, therefore, expected to be a significant contribution to the body of knowledge, supplying new valuable data to be used for validation purposes and to inspire future works.

Table of Contents

List of Figures

List of Tables

Nomenclature

Acronyms

CCD   Charge-Coupled Device

CMOS Complementary Metal–Oxide–Semiconductor

CPU   Central Processing Unit

CVV   Coaxial Volumetric Velocimetry

DES   Detached-Eddy Simulation

DOF   Depth Of Field

DSR   Dynamic Spatial Range

DVR   Dynamic Velocity Range

FOV   Field Of View

FSU   Fluid Supply Unit

HFSB Helium-Filled Soap Bubbles

HPF   High Pass Filter

IPR   Iterative Particle Reconstruction

LDA   Laser Doppler Anemometry

LES   Large-Eddy Simulation

MART Multiplicative Algebraic Reconstruction Technique

OJF   Open Jet Facility

PIV   Particle Image Velocimetry

PTU   Programmable Time Unit

PTV   Particle Tracking Velocimetry

RAM   Random Access Memory

RANS   Reynolds-Averaged Navier-Stokes

SSD   Solid State Disk

STB   *Shake The Box*

VG   Vortex Generator

Symbols

$\bar{\sigma}_u$	Average standard deviation of the velocity u resulting from CVV measurements	[-]
$\bar{u}$	Mean of the velocity u	[m/s]
β	Cross-wind angle	[°]
β	Tomographic aperture angle	[°]
δ^*	Boundary layer displacement thickness	[mm]
Δ_p	STB maximum allowed particle shift	[px]
δ_p	Average free-stream particle displacement between two consecutive frames	[px]
Δ_x	Displacement in X-direction non-dimensionalized with H	[-]
Δ_y	Displacement in Y-direction non-dimensionalized with H	[-]
Δ_y	Displacement in Z-direction non-dimensionalized with H	[-]
$\delta_{.95}$	Boundary layer thickness at 95% of free-stream velocity	[mm]
Δ_{Γ_x}	Streamwise vorticity variation	[-]
Δ_{ω_x}	Streamwise vorticity variation	[-]
Δ_{px}	Pixel pitch of the camera sensor	[μm]
$\dot{V}_s$	Volumetric flow rate of the seeded region	[cm^3/s]
ϵ_x	Triangulation uncertainty in X-direction	[mm]
ϵ_y	Triangulation uncertainty in Y-direction	[mm]
ϵ_z	Triangulation uncertainty in Z-direction	[mm]
Γ	Non-dimensional vorticity index	[-]
λ	Light wavelength	[nm]
μ	Dynamic viscosity	[m^2/s]

ω	Vorticity	[s^{-1}]
ω_x	Streamwise vorticity	[s^{-1}]
$\boldsymbol{\nabla u}$	Velocity gradient tensor	[s^{-1}]
$\boldsymbol{\Omega}$	Antisymmetric part of the gradient tensor	[s^{-1}]
$\boldsymbol{S}$	Symmetric part of the gradient tensor	[s^{-1}]
ρ_f	Fluid density	[kg/m^3]
ρ_p	Particles density	[kg/m^3]
ρ_∞	Free-stream density	[kg/m^3]
σ_u	Standard deviation of the velocity u	[-]
θ	Boundary layer momentum thickness	[mm]
θ_{vol}	Laser light expansion angle	[°]
ε_u	Uncertainty of the velocity measurement	[-]
ε_Δ	STB allowed triangulation error	[px]
φ	Slant angle	[°]
φ_M	Higher critical slant Angle	[°]
φ_m	Lower critical slant angle	[°]
$\vec{x}_{cor}$	Centre of rotation coordinates with respect to camera reference system XYZ$_{camera}$	[mm]
A_s	Cross-sectional area of the seeded volume inside the settling chamber	[cm^2]
b	Camera sensor depth	[bit]
C_D	Drag coefficient	[-]
C_L	Lift coefficient	[-]
C_N	Yawing moment coefficient	[-]
C_p	Pressure coefficient	[-]
C_Y	Side force coefficient	[-]
C_{HFSB}	HFSB seeding concentration	[bubbles/cm^3]
D	Aperture diameter of the lens	[mm]
d_0	Object distance	[m]

D_F	Far limit of the DOF	[cm]
d_i	Image distance	[m]
D_N	Near limit of the DOF	[cm]
d_p	Particle diameter	[μm]
d_z	Reconstructed in-depth particle size	[μm]
d_τ	Particle image diameter	[μm]
f	Focal length	[mm]
$f_{\#}$	Lens aperture, F-stop (f-number)	[-]
f_{ac}	Acquisition frequency	[Hz]
H	Reference length, height of the Ahmed body	[mm]
H_d	Hyperfocal distance	[mm]
H_{BL}	Boundary layer shape factor	[-]
I_p	Scattered light intensity collected by the camera system	[W/m^2]
I_{min}	Minimum particle image intensity detectable	[counts]
k	Coverage factor	[-]
L_x	Width of measurement volume	[cm]
L_y	Height of measurement volume	[cm]
l_{bin}	Bin characteristic length	[-]
l_{px}	Pixel size	[mm]
M	Magnification factor	[-]
N	Number of samples	[-]
P	Static Pressure	[Pa]
ppp	Particles per pixel	[-]
Q	Second invariant of the velocity gradient tensor	[s^{-2}]
Re	Reynolds number	[-]
St	Strouhal number	[-]
T_{ac}	Acquisition period	[s]

U_s	Flow speed inside the settling chamber	[m/s]
U_∞	Free-stream velocity	[m/s]
U_{slip}	Slip velocity	[m/s]
V_R	CVV probe velocity perturbation in radial direction	[-]
V_τ	CVV probe velocity perturbation in tangential direction	[-]
z_f	Focal plane distance	[mm]
z_{max}	Upper limit of measurement volume	[cm]
z_{min}	Lower limit of measurement volume	[cm]

Part I

Introduction, Robotic Volumetric Velocimetry and Experimental Setup

1

Introduction and Literature

In this chapter the Ahmed body is introduced from a historical point of view, highlighting its importance with respect to the first attempt of reducing the aerodynamic drag of roads vehicles. Moving from the first pioneering studies and the main references to a wider literature, the relevance of the Ahmed body to present times is explained. Following this preliminary part, the objectives of the thesis are presented, together with two research questions whose aim is to lead the author during the proposed investigation. Finally, the structure of the thesis is briefly outlined.

Contents

1.1   Introduction

The interest of both the automotive industry and research community on the aerodynamics of road vehicles arose during the 70s as the result of a global oil crisis which widely affected Western European countries as well as the United States. In 1973 indeed, and, again, in 1979, during the two so-called "*Oil Crises*", the fuel cost alarmingly increased which in turn generated, among the other things, a shared interest in improving the efficiency of ground transportation (Hucho, 1978). At that time, however, most of the research concerning aerodynamics was focused on aeronautical applications, which translation into automotive field proved not to be straightforward and, sometimes, even misleading. The flow field resulting from a bluff body operating in ground effect like a road vehicle, indeed, can be radically different from the one generated by a streamlined wing. The wake of a car, for instance, can show both almost axis-symmetric and quasi-two-dimensional separation areas as well as fully three-dimensional separations along with strong counter-rotating vortices. Moreover, in a somehow paradoxical way, especially true for an aeronautical engineer, an increase in separation could lead to a substantial drag reduction. Given the complexity of the problem as well as the need for addressing it quickly, it, therefore, appeared convenient to both the automotive industry and the research community to join forces (Sovran et al., 1978). A posthumous review on this topic by both the aforementioned authors (Hucho & Sovran, 1993), estimated the engine power required by a mid-size car to overcome the aerodynamic drag during Highway cruising in excess of 50% of the total power. The aerodynamic drag, therefore, resulted still of great interest with respect to the fuel economy of common road vehicles.

1.2   Literature

1.2.1   The Ahmed Body and the Aerodynamic Drag of Road Vehicles

As introduced before, because of both high fuel costs and the global energy situation, the main goal of researchers was to improve the understanding of aerodynamically generated drag for road vehicles, aiming at a substantial drag reduction to considerably increase the efficiency of ground transportation. The first effort in this sense can be found in the proceedings containing the papers and oral discussions presented at the *Symposium on Aerodynamic Drag Mechanisms of Bluff Bodies and Road Vehicles* held in 1976 at the General Motors Research Laboratories in Warren, Michigan (Sovran et al., 1978). Of great interest among such papers, the opening one, titled *The Aerodynamic Drag of Cars. Current Understanding, Unresolved Problems, and Future Prospects* Hucho (1978). The paper focused on the aerodynamic drag of cars from a practitioner's perspective, starting from the contemporary understanding of the involved mechanisms. A survey investigating a total of 86 European passenger cars produced during the antecedent decade highlighted a remarkable variance in drag in spite of similar car shapes. The drag coefficient C_D varied between 0.37 and 0.52, with an average representative value of roughly 0.46. The authors considered the achievement of a drag coefficient equal to 0.30 feasible, which in turn would have produced a 15% fuel saving. When introducing the mechanisms of air drag, particular importance was drawn on the rear-end of the cars and different kinds of contours were identified - hatchback, notchback and fastback (see figure 1.1). Two different kinds of sepa-

ration could be distinguished, depending on the geometry of the rear, and in particular on the slant angle φ, defined as the angle between the horizontal plane and the rear-window (see figure 1.2). The detachment of the flow can take place straight after the roof trailing edge, showing a quasi-two-dimensional recirculation inside the wake, generating a so-called squareback-type flow field and, despite the size of the recirculation, showing a moderate drag. Such flow field occurs for slant angles φ greater than a certain critical value, approximately $\varphi > 30°$. The other possible separation pattern is instead highly three-dimensional. Two counter-rotating longitudinal vortices are shed from the slant side edges, driven by the lower pressure on the top and on the rear of the car. The resulting downwash between the vortices reattaches the flow on the slant surface and therefore decreases the size of the separated region. The two vortices, named C-pillar vortices, resemble the flow field generated by a delta wing at high angle-of-attack and,

(a) Hatchback

(b) Notchback

(c) Fastback
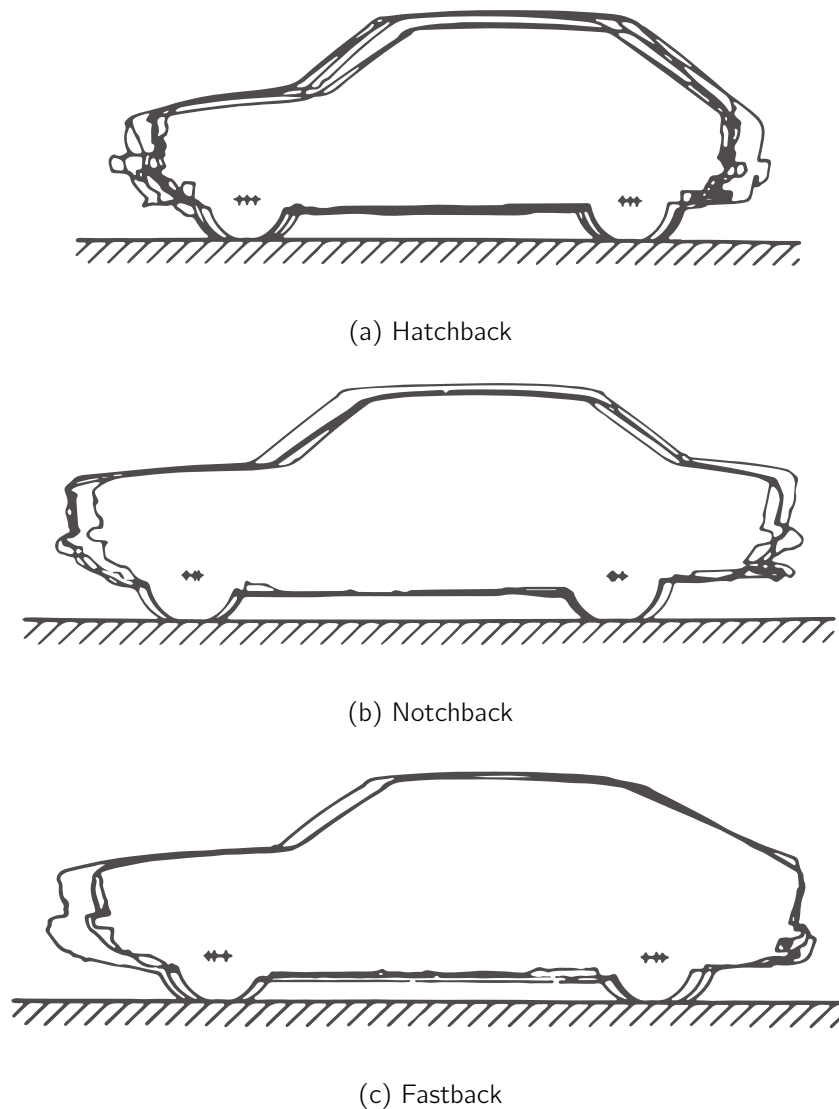
Figure 1.1: Centreline cross-sections of European cars (Hucho, 1978).

despite the smaller separation, the drag is higher due to the low pressure induced by the vortices and keeps increasing with increasing φ, together with the strength of the two longitudinal vortices. The described flow pattern occurs for slant angles smaller than $30°$. Decreasing the slant angle the strength of the vortices decreases, decreasing the so-called vortex drag and ultimately the total drag (see figure 1.2). A minimum is reached around $\varphi \approx 15°$, configuration therefore named 'fastback' (see figures 1.2 and 1.3). A further decrease of the slant angle finally reverts to a squareback-type geometry and flow field. Finally, around the critical value of $\varphi \approx 30°$, the flow field switches continuously from a fastback to a squareback-type flow regime. The paper also describes an interesting drag breakdown, introducing the differences with the aeronautical
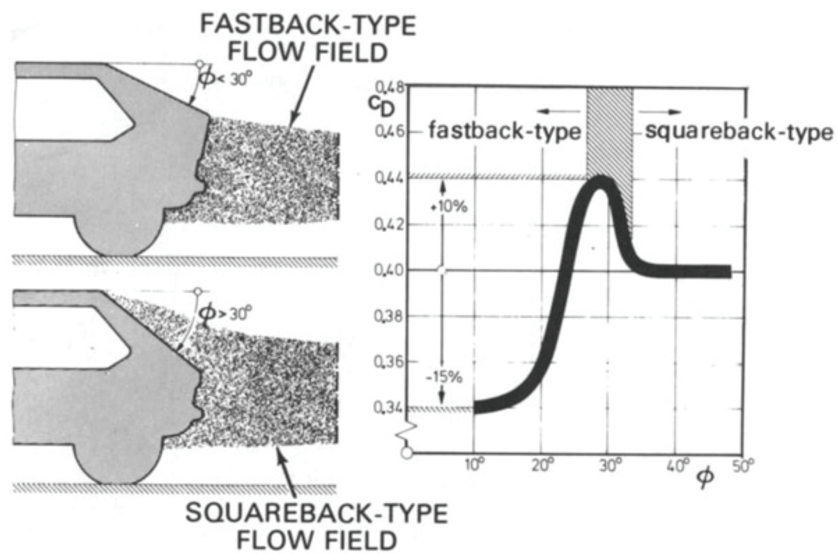
Figure 1.2: Influence of rear-end inclination angle on drag coefficient, C_D, separation line, and wake formation (Hucho, 1978).
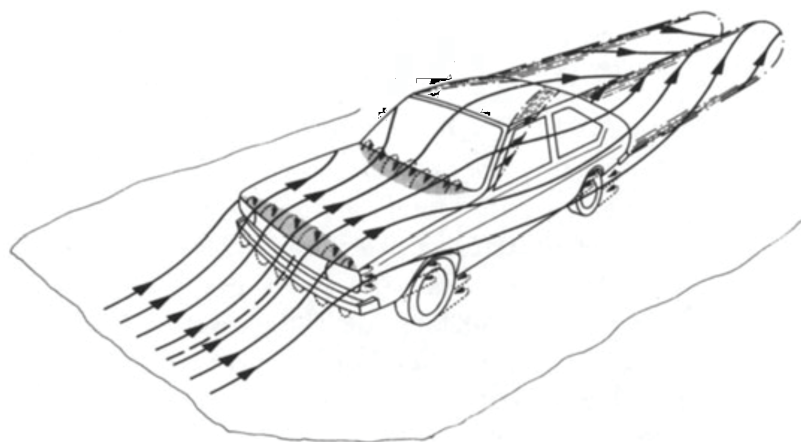
Figure 1.3: Flow field around a fastback car, front three-quarter view (scheme) (Hucho, 1978).

field with respect to pressure, skin friction and induced drag. Of great interest, some considerations on the latter. Indeed, despite the possible presence of a flow field resembling the one generated by a low aspect ratio wing, for the studied case of bluff bodies close to the ground, no relation between the lift and the drag appears to exist. The term *induced drag*, of aeronautical derivation, was therefore substituted with *vortex drag* and would have been dealt with in more details during the symposium.

Another paper of relevance, found in the same proceedings, is titled *The Effect of Base Slant on the Flow Pattern and Drag of Three-dimensional Bodies with Blunt Ends*, from Morel & Sovran (1978). The authors, again, identified two different flow patterns, illustrated in figure 1.4, one similar to the one found behind axisymmetric bodies without slant, with a quasi-two-dimensional separation (a), and another highly three-dimensional with the presence of both recirculation and two longitudinal vortices (b). A maximum in drag coefficient is observed for the range of slant angles where a switch from one flow field to the other takes place and this is associated with the identification of a so-called 'critical geometry'. Other than studying an axisymmetric body with varying the base slant angle, the authors proposed a very simplified vehicle-like body, illustrated in figure 1.5 (a), which would have greatly inspired Ahmed a few years later. Among the interesting results obtained on such model, the fact that the lift has an even more noticeable variation with changing the slant angle. A positive C_L was expected "*as the slant exposes an upward projection of the low-pressure after body surface*" (Morel & Sovran, 1978). However, the lift coefficient exceeding the C_D in the proximity of the critical slant angle was unexpected. The paper also shows the two possible bi-stable pressure patterns on the slanted-surface for the same critical afterbody geometry in ground proximity. Although the presence of the downwash induced by the vortices reattaches the flow on the slant and an increase in base pressure may be expected, just the opposite is true. Not only the vortices induce very high local suction but also in the centreline, far away from the low pressure of the cores, the overall pressure is lower if compared to the quasi-two-dimensional flow pattern, as illustrated by figure 1.5 (b). Moreover, when interrogated on the nature of the generated drag, whether induced and lift-related, the authors clarified their point of view. If integrating both the pressure distribution and the surface shear stresses on the car, the total drag exerted on the vehicle is obtained. The rotational energy contained within the vortices is part of the overall drag and

(a) Quasi-axisymmetric Separation Pattern   (b) 3D Separation Pattern
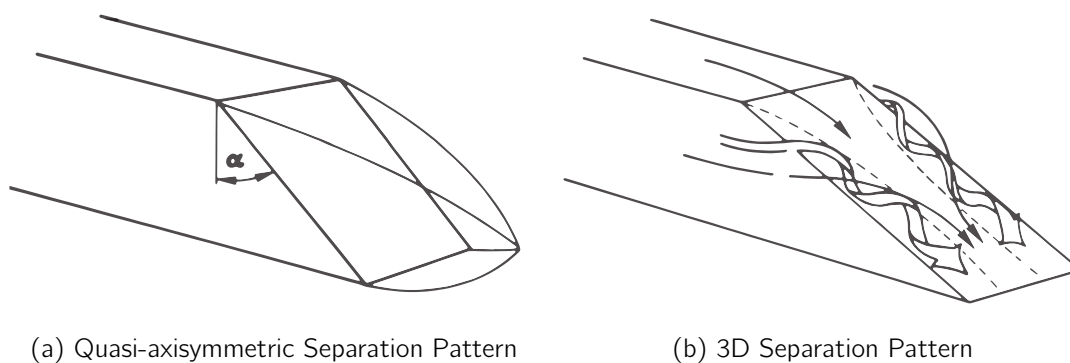
Figure 1.4: Two types of separated-flow pattern on a slanted base (Morel & Sovran, 1978).

(a) Experimental arrangement   (b) Pressure distribution
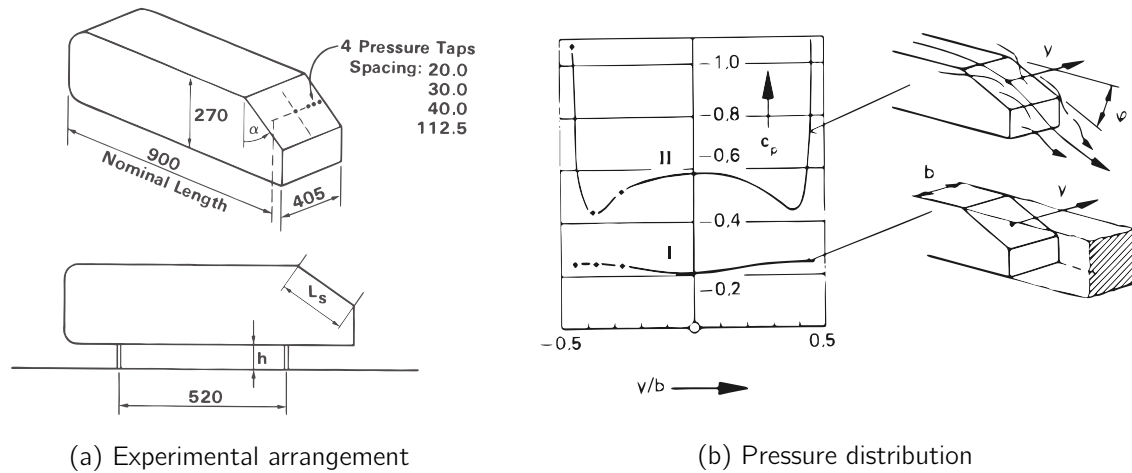
Figure 1.5: Vehicle-like body geometry and pressure distribution over its slant for the two flow regimes; flow regime I, $\varphi > 30°$: quasi-two-dimensional separation; flow regime II, $\varphi < 30°$: three-dimensional separation with the formation of C-pillar vortices (Morel & Sovran, 1978).

should not be added to the one just obtained. This can be seen as in contrast to the common aeronautical approach where profile drag, integral of pressure and shear stresses, is evaluated in a somehow two-dimensional way and then the inviscid induced drag is added.

A few years later, inspired by the pioneering work of Morel & Sovran (1978), Ahmed published a paper titled *Some salient features of the time-averaged ground vehicle wake* (Ahmed et al., 1984) which is, still today, considered a milestone in the study of road vehicles aerodynamics. Being at that time already clear the convenience of a somehow common research framework, a standard simplified reference body needed to be introduced which could generate an aerodynamic flow field representative of the one of different cars. As mentioned above, a first vehicle-like simplified bluff body with interchangeable bases of various slant angles was firstly introduced by Morel & Sovran (1978) and after some iterations it became the reference for the automotive field, being named "Ahmed reference body" after his designer (Ahmed et al., 1984). Ahmed, indeed, defined the dimensions and proportions of a reference model which would have been intensively studied in the coming years. The scheme of the model can be appreciated, as presented in the original paper, in figure 1.6. The length, width and height of the model are respectively 1044 mm, 389 mm and 288 mm, while the length of the slanted surface remains constant and equal to 222 mm, no matter the slant angle. The front of the body is rounded in order to avoid separation while the body itself is supported by 4 circular stilts which generate a clearance from the ground of 50 mm. The length-based Reynolds number of the experiments was 4.29×10^6 and a great variety of slant angles have been investigated. In agreement with Hucho (1978) and Morel & Sovran (1978), two main flow patterns were identified, delimited by a lower and an upper threshold values for the slant angle, $\varphi_m = 12°$ and $\varphi_M = 30°$ respectively. Two-dimensional flow is generated for slant angle values lower than φ_m which becomes highly three-dimensional when the slant angle is increased in the range between φ_m and φ_M. As previously highlighted, the flow then reverts to a two-dimensional pattern for values of φ greater than φ_M,
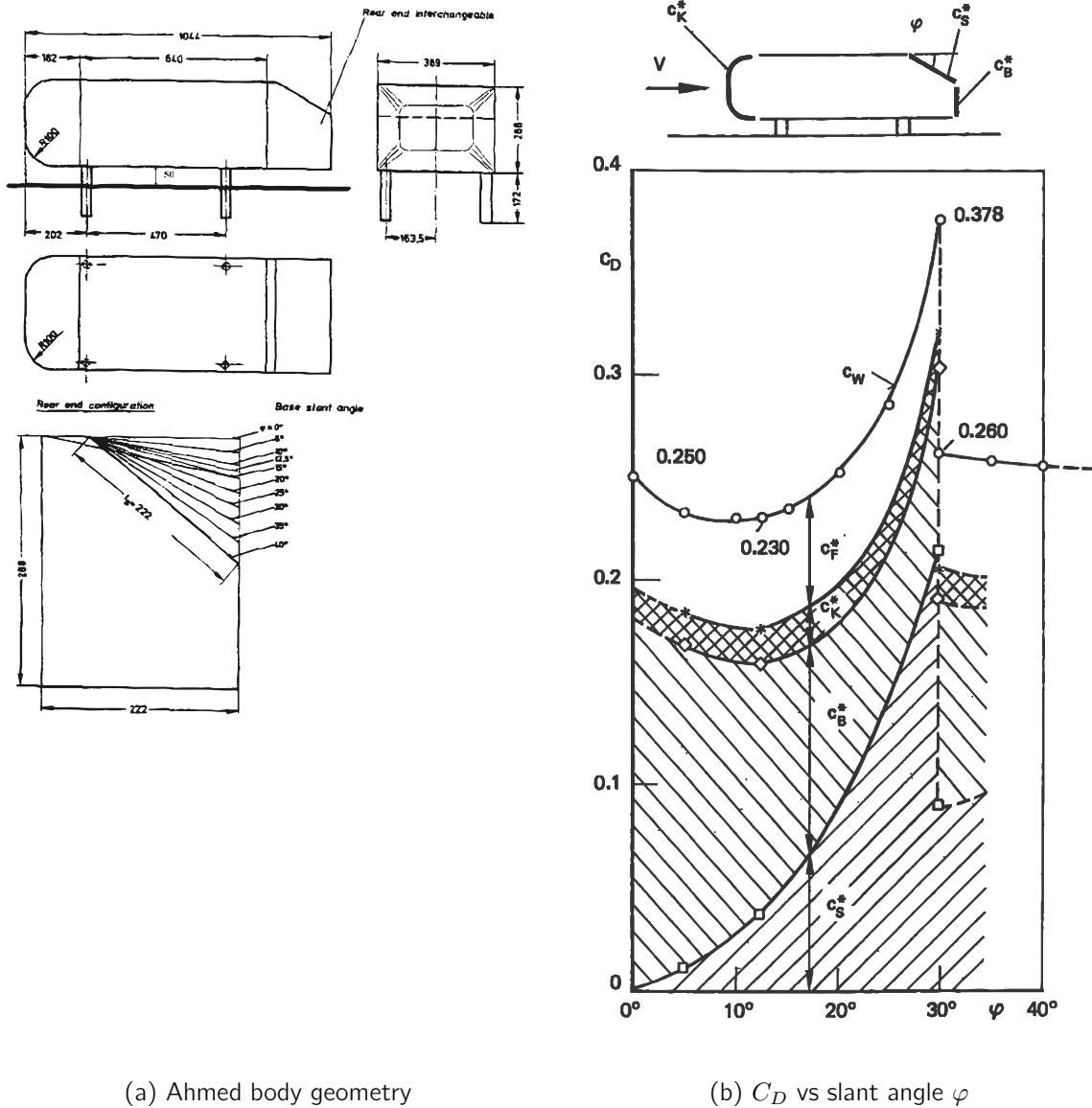
(a) Ahmed body geometry

(b) C_D vs slant angle φ

Figure 1.6: Ahmed body geometry (a) and influence of slant angle φ on overall drag (Ahmed et al., 1984).

until the geometry resembles a square-back rear-end. Other than the drag coefficient evolution with varying the slant angle reported in figure 1.6, the paper offers very effective two and three-dimensional flow field topology description. Figure 1.7, indeed, depicts the aforementioned flow behaviour obtained with varying the slant angle φ. For slant angles smaller than φ_m (a,b) the flow coming from the roof remains attached to the slant and does separate over the back-facing surface, also called *base*. The flow from the two side walls, as well as the one from the top and bottom surfaces, does roll up on the base generating the toroidal vortex system depicted in figure 1.8 (a). This three-dimensional structure looks like two counter-rotating vortices in
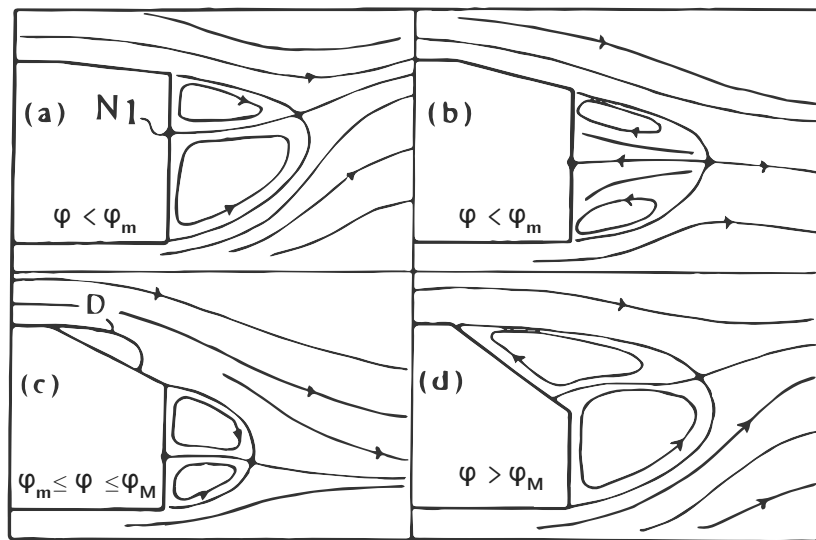
Figure 1.7: Different flow topologies of the wake of the Ahmed body in the symmetry plane with varying the slant angle (Ahmed et al., 1984).

(a) Quasi-2D wake

(b) Fully 3D wake
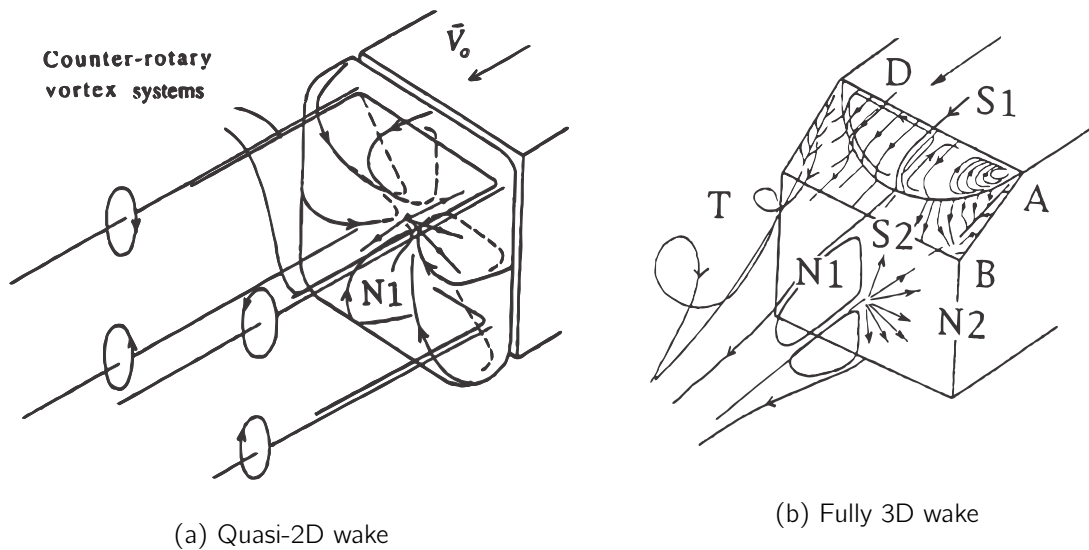
Figure 1.8: Different flow topologies of the wake of the Ahmed body, three-dimensional representation (Ahmed et al., 1984).

the symmetry plane, defining a so-called recirculation zone and inducing low pressures on the base. Moreover, the streamlines influenced by the toroid do converge into a singular point, namely, the attachment node N1. When the slant angle increases above the lower critical angle φ_m (c), the flow becomes highly three-dimensional, displaying two longitudinal counter-rotating vortices. Such vortices are driven by the low pressure on the rear of the model which rolls up the flow coming from the side walls after it separates at slant side-edges (separation line

AB of figure 1.8 (b)). At the same time, on the slant surface, an open separation bubble appears whose extension is limited by the downwash generated by the two longitudinal vortices, promoting flow reattachment. As the slant angle further increases beyond the upper critical angle φ_M (d), the flow separates at the slant leading edge and the vortex system reverts to the quasi-two-dimensional flow pattern described above (a,b). It is interesting to notice how the attachment point N1 moves downward on the base surface when increasing the slant angle and how this is associated with a downward curvature of the streamlines (lift generation). As said before, when the critical slant angle φ_M is reached (d), the flow field reverts to a quasi-two-dimensional separation, resembling the squareback configuration (a), also in terms of streamline pattern. For the sake of completeness, and, since of relevance to the present work, a detail of the three-dimensional flow field generated for slant angles ranging between φ_m and φ_M (c) is depicted in figure 1.8. Despite a similar highly three-dimensional configuration, in the first case (a), a slant angle of approximately 15° does not separate the flow coming from the roof, being also helped in turning the slant leading edge by the downwash induced by the two side vortices. The combination of still weak side vortices and the absence of the slant separation bulb explains the minimum in drag found for such fastback configuration and reported in figure 1.6. With increasing the slant angle, however, the slant separation bubble appears, but the flow still manages to reattach before the slant trailing edge because of a stronger downwash. The high suction induced by the now stronger side vortices is responsible for the high drag typical of such configuration.
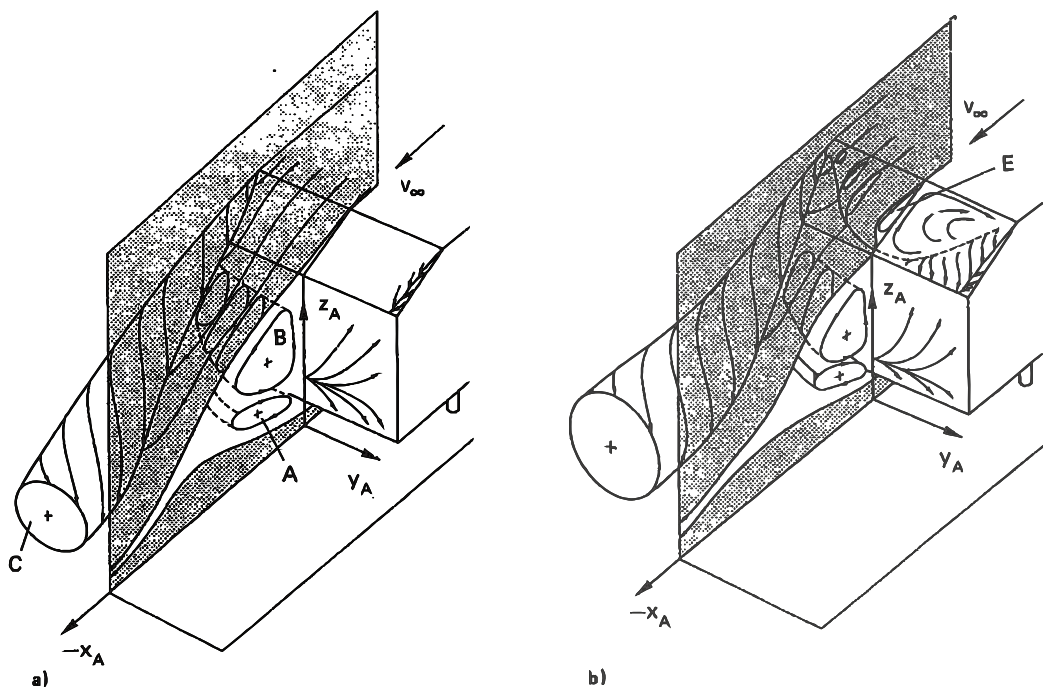
Figure 1.9: Vortex system for a fastback Ahmed body with: a) low drag coefficient, b) high drag coefficient with $\varphi = 30°$ (Ahmed et al., 1984).

Several years after the work of Ahmed et al. (1984), Laser Doppler Anemometry (LDA) was used as main measurement technique by Lienhart & Becker (2003) in a comprehensive study to investigate both the velocity in the symmetry plane and the wake downstream the Ahmed model. The aim of the work was mainly to "*supply a detailed data set acquired under well-defined boundary conditions to be used as reference data for numerical simulations in general and the validation and verification of refined turbulence models in particular*" (Lienhart & Becker, 2003). Two slant angles have been investigated, namely 25° and 35°. Besides LDA, also hot-wire was used to measure the boundary layer on the symmetry plane and static pressure measurements over the rear part of the body were carried out as well, together with smoke and oil flow visualization. All the data from the experiment has been made available to the research community and it has become a reference for all the following studies, both experimental and computational. For the sake of completeness, the most representative results are reported below. Static pressure measurements on the two models are plotted in figure 1.10 and, as expected, for the 25° configuration the high-suction footprint of the vortices close to the slant side-edge is evident. The velocity vectors and the turbulent kinetic energy in the symmetry plane are shown for both the 25° and 35° configurations in figure 1.11 and 1.12, respectively. As expected, again, the first image shows a predominantly attached flow on the slant surface, differently from the following case. Finally, figure 1.13 and 1.14 show the development of the wake through four cross-planes behind the model for both the slants. Again, if in the former the presence of the two longitudinal vortices is very clear and persistent, in the latter the wake proves to be immediately separated and in good approximation two-dimensional, as expected.
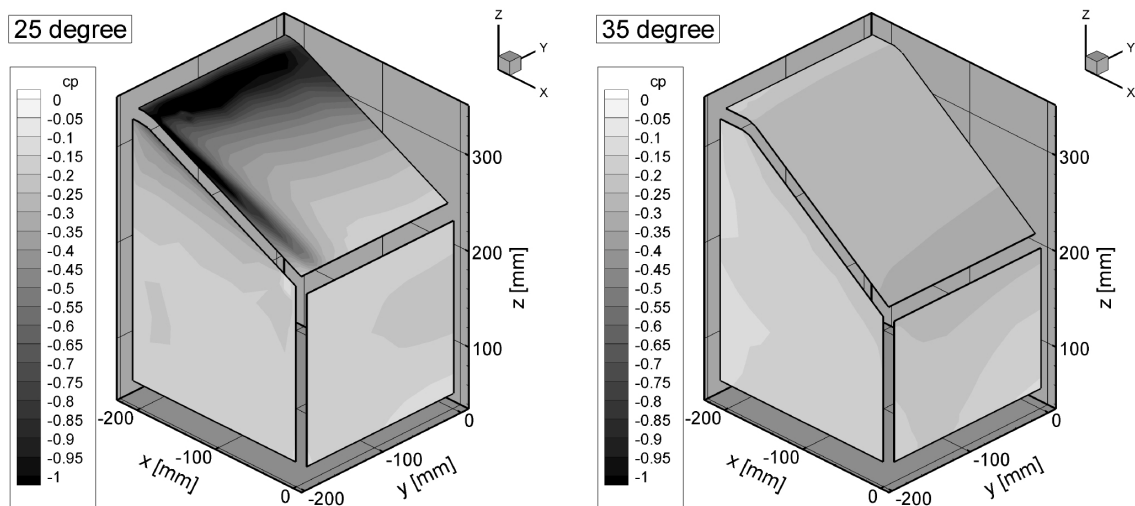
Figure 1.10: Pressure distributions on the rear of the 25° and the 35° slant model (Lienhart & Becker, 2003).
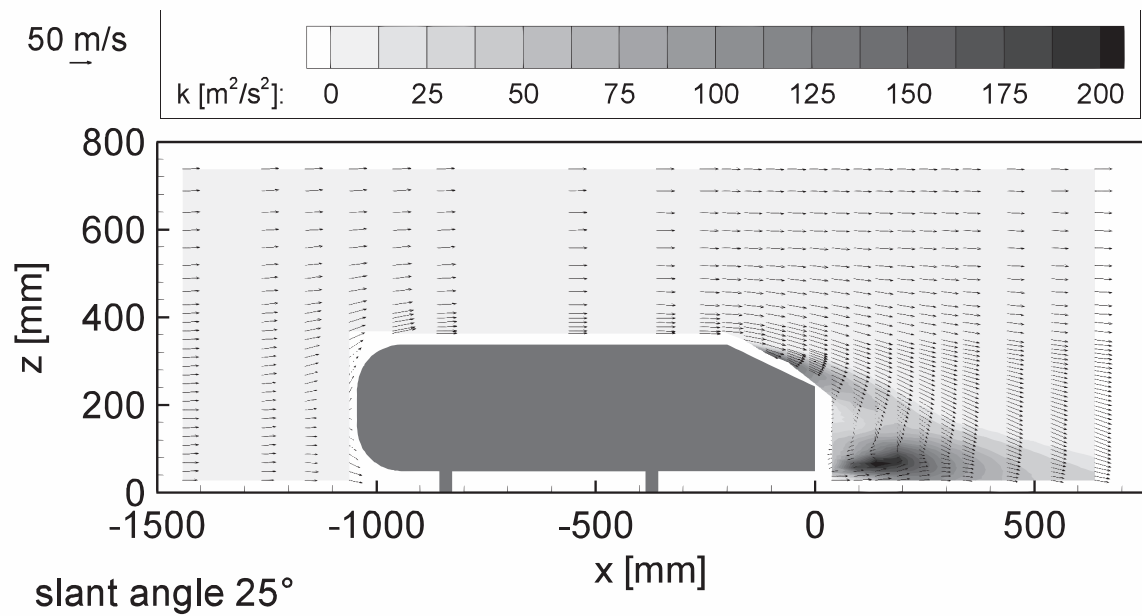
Figure 1.11: Velocity vectors and turbulent kinetic energy in the symmetry plane for a 25° slant angle (Lienhart & Becker, 2003).
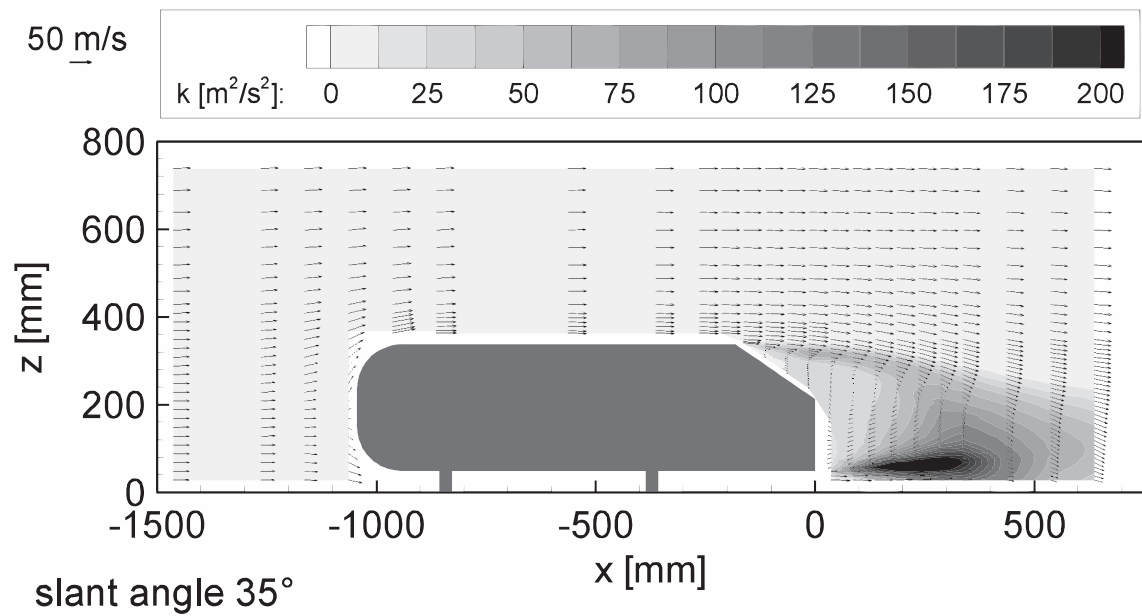
Figure 1.12: Velocity vectors and turbulent kinetic energy in the symmetry plane for a 35° slant angle (Lienhart & Becker, 2003).
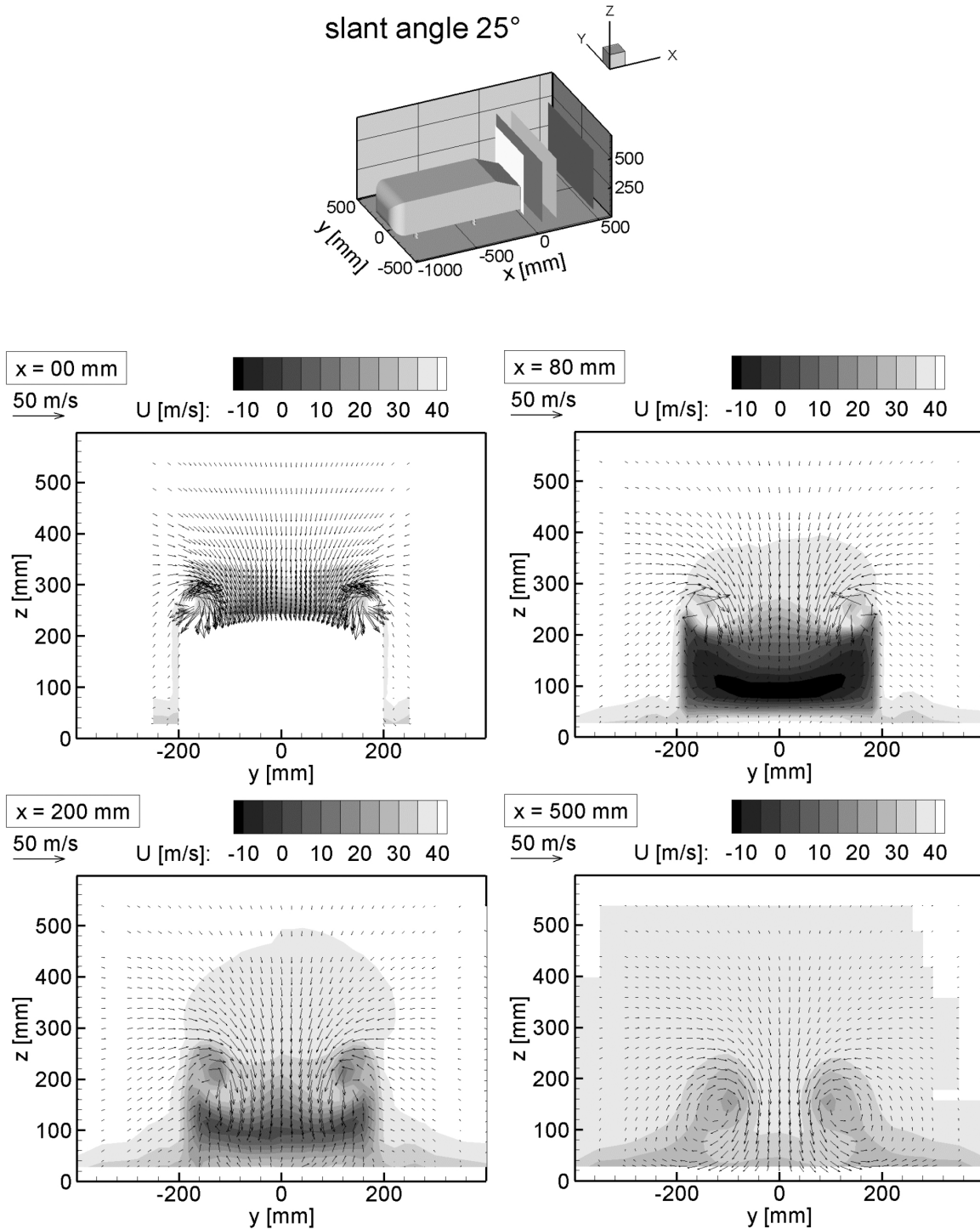
Figure 1.13: Development of the wake behind the 25° slant model (Lienhart & Becker, 2003).
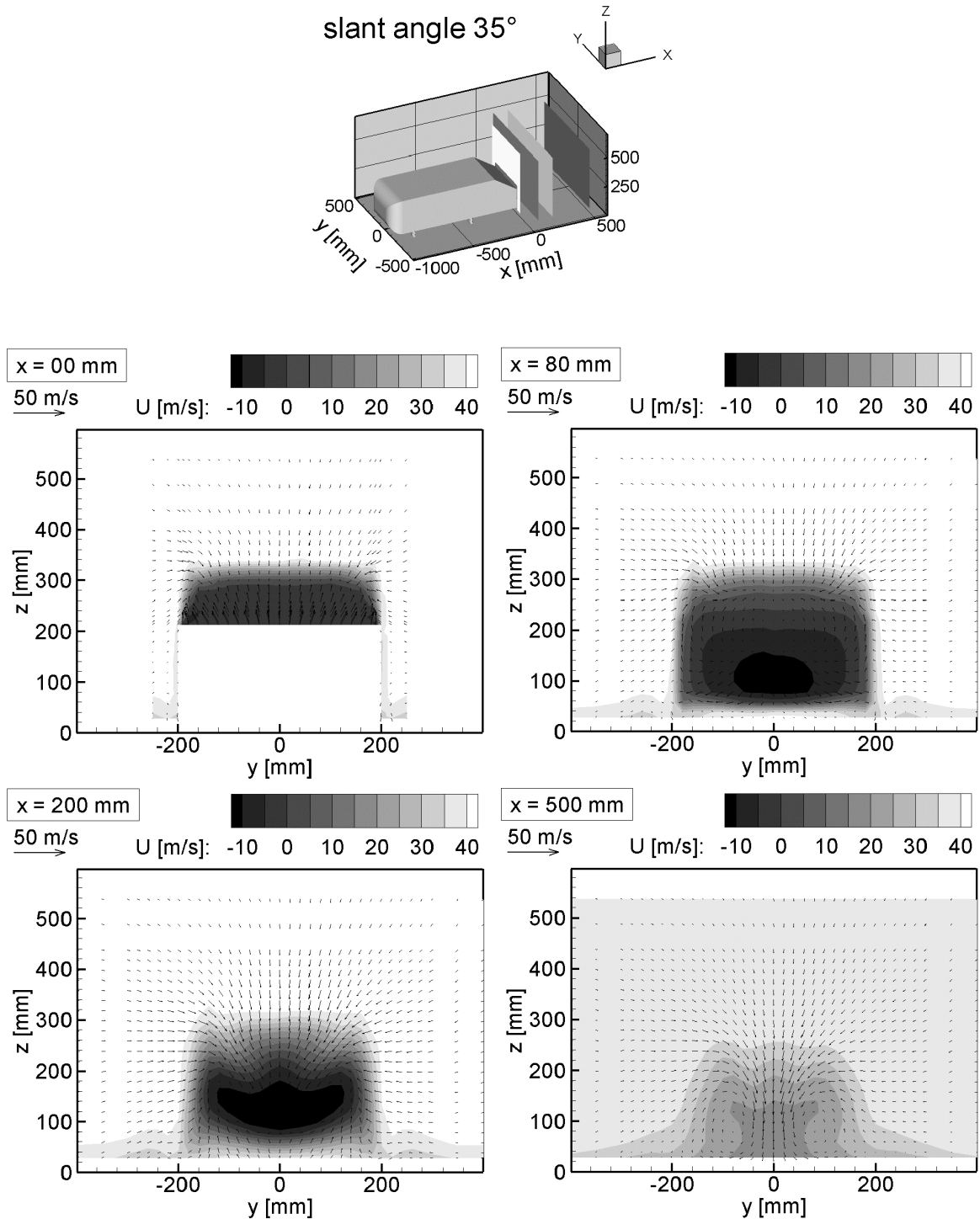
Figure 1.14: Development of the wake behind the 35° slant model (Lienhart & Becker, 2003).

1.2.2   The Ahmed Body as Proof-of-Concept

Although car manufacturers do, nowadays, study the complex shapes of a real car exploiting their strong aerodynamic understanding and know-how, the Ahmed body is still used to test new techniques and drag reduction methods as a sort of proof-of-concept. Following the afore-mentioned studies, indeed, a vast literature regarding experimental investigations can be found which aims mainly at a more precise flow topology characterisation as well as at a substantial drag reduction by different methods. Cavitation, for instance, has been used as alternative non-intrusive visualisation technique to capture the longitudinal vortical structures while providing at the same time pressure measurements (Beaudoin et al., 2004). An in-depth investigation of the critical slant angle configuration, i.e. $\varphi = 30°$, was carried out and, among the other things, a slightly revised and more detailed flow topology was proposed (Vino et al., 2005). An investiga-tion in proximity of a moving ground by LDA showed the presence of lower longitudinal vortices produced by the absence of the slits (Strachan et al., 2007). The overhead supporting strut, however, had the effect of weakening the C-pillar vortices which in turn decreased the downwash on the slant surface failing in promoting reattachment of the flow for the $30°$ configuration. The use of flaps in different locations and configurations was successfully employed with the goal of reducing drag (Beaudoin & Aider, 2008). Other than a 25% reduction in drag, also a 105% reduction in lift was achieved and the flow field was investigated by means of planar Particle Image Velocimetry (PIV). Passive flow control by means of vortex generators (VG) was tested on a modified Ahmed body with a curved rear (Aider et al., 2010). A maximum 15% reduction in drag coefficient, as well as a 104% decrease in lift, were accomplished and planar PIV was used again as non-intrusive investigation technique. A similar approach was followed by Pujals et al. (2010), exploiting this time cylindrical VG. Also active flow control, in the form of steady microjet arrays (Aubrun et al., 2011) and pulsed jets (Joseph et al., 2012), was used to reduce the slant separation, achieving up to a 14% drag reduction. Another approach to decrease and, actually, eliminate the separation on the slant surface has been adopted by Thacker et al. (2012). This consisted in rounding off the corner connecting the roof to the slant itself which resulted in a 10% reduction in drag. A similar drag coefficient reduction has been obtained also by Tounsi et al. (2016), this time with the use of piezoelectric actuators. Also the effect of the aspect ratio of the Ahmed body has been investigated (Venning et al., 2015), discovering a critical aspect ratio able to produce on the flow field the same effect of the critical slant angle and therefore to affect drag accordingly. An experimental flow visualisation around the whole model, by Spohn & Gillieron (2002), highlighted for the first time experimentally flow separation and reattachment on the front-end of the model, although the dramatically low Reynolds number, up to two orders of magnitude lower then the one used by Lienhart & Becker (2003), poses extreme doubts about the reliability of the results, especially with respect to highly Reynolds number dependent phe-nomena such as flow separation and reattachment. Grandemange et al. (2013) experimentally studied the global modes and bi-stability of the wake past a squareback Ahmed body and later also investigated the effects on the drag at an industrial scale (Grandemange et al., 2015). Of particular interest for the present work is the fact that bi-stability has been studied also with the help of yaw angles. Similarly, Meile et al. (2016) studied the bi-stability of the wake of a slanted Ahmed body, introducing even bigger yaw. Another very interesting investigation was

carried out by Zhang et al. (2015), who studied the unsteady flow structures around the Ahmed body. Particular attention has been paid to the Strouhal number of the different flow structures and the effect of the Reynolds number has been addressed as well, following the work of Vino et al. (2005). Finally, similarly to what done by Grandemange et al. (2015), an industrial-sized squareback Ahmed body has been studied by Evrard et al. (2017), this time to compare the effects of vortex generators on the simplified body and on a real car (Peugeot 208).

1.2.3   The Ahmed Body in Steady Cross-Wind

With good approximation, when considering the motion of ground vehicles, a certain amount of ambient wind is always present. As a consequence, the velocity of the vehicle with respect to the ground is different from its velocity with respect to the air. If the wind is not aligned with the travelling direction, a yaw angle arises whose extent depends both on the direction of the wind and on its magnitude with respect to the ground speed of the vehicle (see figure 1.15). Once more, differently from aeronautical practice, the drag force relevant to propulsion requirements and fuel economy is the force resultant aligned with the travelling path, rather than the one aligned with the relative wind (Sovran et al., 1978). As a result of a cross-wind angle β different from zero, the flowfield around the vehicle becomes asymmetric which in turn generates a side force together with a yawing and rolling moment. At the same time, also the lift, the drag and the pitching moment are affected and usually increase (Hucho & Sovran, 1993). Some typical variation of drag coefficient C_D, yaw moment coefficient C_N and side force coefficient C_Y with varying the yaw angle β are qualitatively illustrated in figure 1.16 (a), (b) and (c), respectively. According to Hucho & Sovran (1993), driving conditions with β large enough to reach the maximum drag are rare, except in gusts, and averages values of β are expected to be less than 10° for typical driving. From a practitioner point of view, if unsteady cross-wind, namely gusts, poses a problem with respect to the handling of the vehicle, steady cross-wind is mainly responsible for an increase in drag and therefore its study is relevant from a fuel economy perspective.

Not much is available in the literature with respect to the Ahmed body in steady cross-wind, and, in particular, nothing with a high-drag configuration rear (25 degrees slant angle). An experimental investigation of the flow structures generated in steady cross-wind by a bluff body in ground proximity has been conducted by Gohlke et al. (2007). The investigated model is
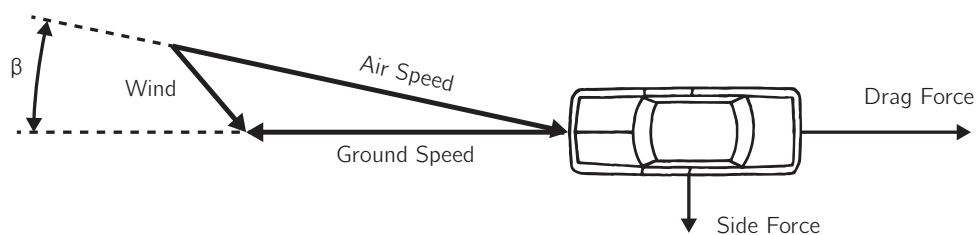
Figure 1.15: Velocity diagram and cross-wind angle β for a road vehicle.
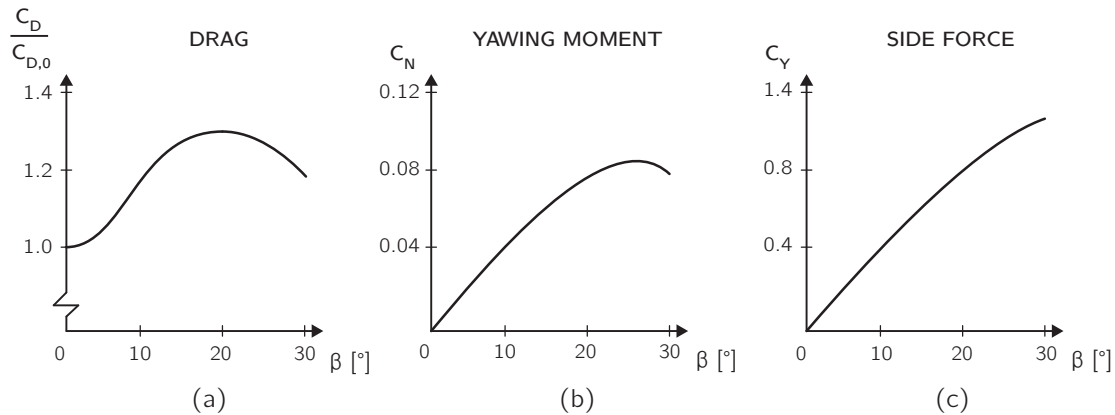
Figure 1.16: Normalized drag coeff. (a), yaw moment coefficient (b) and side force coeff. (c) with varying yaw angle β. Figure adapted from Hucho & Sovran (1993).

similar to an Ahmed body with squareback, although the front and the side corners have been considerably rounded off. Both forces and surface pressures have been measured at different yaw angles and the flow field has been investigated by means of planar PIV and LDA. In particular, planar PIV has been used to study the flow in the symmetry plane while the near wake has been investigated on a horizontal plane downstream the model. Moreover, the vortex shedding on the leeward side of the model has been captured within an x-plane close to the squareback. The same model has been further studied with numerical methods by Guilmineau et al. (2013) and the results achieved by means of a Detached Eddy Simulation (DES) approach have been compared against the ones provided by Gohlke et al. (2007).

As mentioned before, yawed configurations have been used in experimental investigations of the stability behaviour of the wake, such as the ones from Grandemange et al. (2015) and Meile et al. (2016). If in the first study pressure probes were used to characterize the wake behind a squareback model, again, in the second one Stereo-PIV was employed to scan the wake with different y-planes for both the 25° and 35° slant angles. However, since the bi-stable behaviour of the wake in cross-wind is found only for the greater slant angle, the 25° configuration has been considered not of interest and therefore briefly addressed without adding any relevant notion to the body of knowledge. For the curiosity of the reader, two considerations of the authors concerning such configuration are here reported: "*The longitudinal vortex at the windward side is much larger than observed for smaller yawing angles. A large region is influenced by this vortex upstream above the slant and can be identified in several inner measurement planes. The vortex must, therefore, be initiated upstream at the prismatic part of the Ahmed body*" (Meile et al., 2016) and "*At the windward side of the Ahmed body, this vortex rotates in the same direction as the C-pillar vortex, and it may be assumed that the vortices merge. At the lee side, the roof-edge vortex rotates in opposite direction and, hence, the C-pillar vortex is reduced or even vanishes at larger yawing angles. Pressure profiles clearly support this assumption*" (Meile et al., 2016). As it results from figure 1.17, illustrating the experimental setup, neither the domain upstream the slant nor close to the leeward C-pillar region are in any way investigated, reducing therefore the findings of the authors merely to educated-guesses. Moreover, with

respect to the generated flowfield, the extrapolation of large and longitudinal flow structures from two-dimensional measurements on longitudinal y-planes belonging to a limited volume (see figure 1.17) seems therefore not appropriate nor quantitative enough to be relevant, leaving considerable space for improvement.
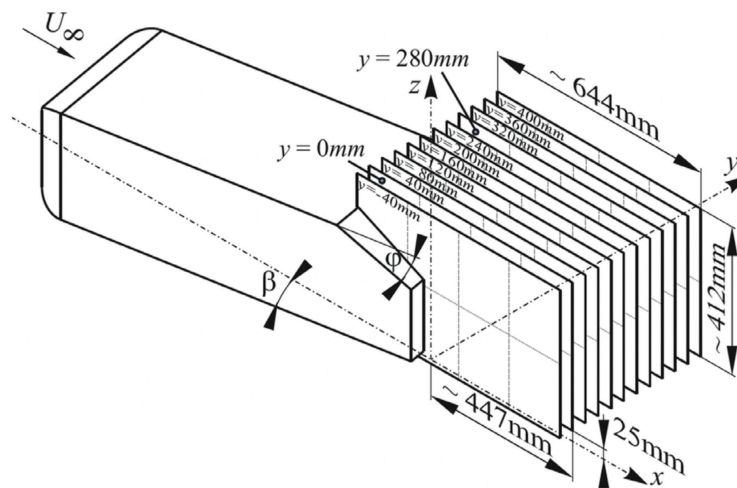
Figure 1.17: Ahmed body in cross-wind, overview of the Stereo-PIV measurement planes from Meile et al. (2016).

1.2.4   The Ahmed Body as CFD Benchmark

With CFD gaining more and more momentum, driven by an exponential increase in available resources, many computational investigations have been carried out which aim at matching as precisely as possible the experimental data provided in the literature. The first comprehensive CFD study was performed by Gillieron (1999) when the state-of-the-art were Reynolds-Averaged Navier-Stokes (RANS) simulations together with k-ϵ turbulence model. Many different slant angles have been investigated and, although the computed drag coefficient has been consistently overestimated, the simulations managed to catch the general trend of C_D with varying the slant angle. Large-Eddy Simulations (LES) were performed on the Ahmed body already in 2004 by Krajnovic & Davidson (2004, 2005) while Fares (2006) demonstrated the feasibility of LES approach within the lattice Boltzmann framework. Moreover, high-order LES and wall-resolved LES were employed as well by Minguez et al. (2008) and Keogh et al. (2016), respectively. Less computationally intensive RANS simulations were presented by Guilmineau (2008) and a combination of both techniques, LES and RANS, also known as Detached-Eddy Simulations (DES), was employed by Guilmineau et al. (2011, 2013). Finally, state-of-the-art RANS and DES method were assessed against each other both on an Ahmed and on a realistic automotive model by Ashton et al. (2016).

To conclude the present section, the most representative papers are resumed in table 1.1 together with the employed investigation techniques and configurations.

Table 1.1: Outline of the most relevant experimental and computational investigations.

Experimental Studies	Slant angles, φ [°]	Yaw angles, β [°]	Measurement/Visualization Technique	Reynolds number, Re_H
Ahmed et al. (1984)	0, 5, 10, 12.5, 15, 20, 25, 30, 35, 40	-	10-hole directional probe, strain gauges balance	1.20×10^6
Lienhart & Becker (2003)	25, 35	-	LDA, oil flow	7.68×10^5
Vino et al. (2005)	30	-	13-hole ECA probe, surface pressure, oil flow, smoke	$5.50 \times 10^5 - 7.70 \times 10^5$, $0.73 \times 10^6 - 2.83 \times 10^6$
Gohlke et al. (2007)*	0	$-30 \leq \beta \leq +30$	PIV, LDA, surface pressure, strain gauge balance, oil flow	6.49×10^5
Strachan et al. (2007)	0, 5, 10, 15, 20, 25, 30, 35, 40	-	LDA	4.69×10^5
Spohn & Gillieron (2002)	25	-	Flow vis (electrolytic precipitation technique)	8.31×10^3
Grandemange et al. (2013)	0	-	Stereo-PIV, 6-hole probe, hot-wire probe, surface pressure, bidirectional strain balance	9.20×10^4
Tunay et al. (2014)	25, 30, 35	-	PIV	1.48×10^4
Grandemange et al. (2015)	0	$-3 \leq \beta \leq +3$	18-hole spherical probe, surface pressure, 6-components balance	2.50×10^6
Venning et al. (2015)	25	-	PIV	2.58×10^4
Zhang et al. (2015)	25	-	PIV, hot-wire, laser-induced fluorescence (LIF)	$0.45 \times 10^5 - 2.4 \times 10^5$
Meile et al. (2016)	25, 35	$-15 \leq \beta \leq +15$	Stereo-PIV, surface pressure, 6-components balance	2.78×10^6
CFD Studies	Slant angles, φ [°]	Yaw angles, β [°]	Numerical approach	Reynolds number, Re_H
Gillieron (1999)	0, 10, 12, 20, 25, 30, 40, 50	-	RANS	1.20×10^6
Krajnovic & Davidson (2004, 2005)	25	-	LES	2.00×10^5
Fares (2006)	25, 35	-	LES (Boltzmann)	7.68×10^5
Guilmineau (2008)	25, 35	-	RANS	7.68×10^5
Minguez et al. (2008)	25	-	LES	7.68×10^5
Guilmineau et al. (2011)	25	-	DES	7.68×10^5
Guilmineau et al. (2013)*	0	$0 \leq \beta \leq +30$	DES	9.00×10^5
Ashton et al. (2016)	25, 35	-	RANS, DES	7.68×10^5
Current study	25	$-4 \leq \beta \leq +8$	Robotic Coaxial Volumetric Velocimetry (CVV)	1.15×10^5

* Slightly modified Ahmed body with rounded off front and side corners.

1.3   Objective and Relevance of the Thesis

The present work has a double intent: if from one hand it aims at generating new experimental data with respect to the Ahmed body in steady cross-wind, since no data with three-dimentional measurement techniques are available in the literature, from the other hand it proposes to assess the capabilities of the employed novel technique. As matter of fact, indeed, and to the best of the author's knowledge, this would be the first experimental investigation carried out on the Ahmed body with the employment of robotic PIV techniques. This would, therefore, allow, for the first time, a convenient three-dimensional and quantitative mapping of the volume around the model. The employed novel experimental technique, indeed, has the advantages of considerably simplifying hardware setup and drastically reducing processing time if compared to state-of-the-art tomographic PIV. The author, therefore, believes this has all the ingredients to raise interest at an industrial level.

Two main research questions are identified with the goal of guiding the author during the present experimental investigation. The first research question concerns the investigation of the aerodynamic flow field and reads

> "*What is the influence of a steady cross-wind angle on the wake of an Ahmed body with respect to the headwind case? In particular, what are the effects on the dominant vortical structures produced by a 25 degree slanted rear geometry in terms of position and intensity? What physical mechanisms produce the aforementioned changes?*".

while the second one focuses on the assessment of the employed measurement technique and reads

> "*What are the advantages of robotic coaxial volumetric velocimetry for assessing the qualitative and quantitative flow field of a similar configuration? What is the aerodynamic intrusiveness of the system in terms of velocity and pressure perturbations? What are the performances in terms of dynamic spatial and dynamic velocity range? What are the main differences of the present technique compared to the state-of-the-art measurement techniques in wind tunnel?*".

1.4   Structure of the Thesis

After the present introduction, an overview of the state-of-the-art of different PIV techniques is outlined in chapter 2. Starting from planar, stereo and tomographic PIV, also Particle Tracking Velocimetry (PTV) is presented, together with the respective working principles. Furthermore, also the seeding technique, of pivotal importance for achieving large-scale measurements, namely Helium Filled Soap Bubbles (HFSB), is introduced. After the aforementioned brief background on PIV, the proposed novel measurement technique is dealt with in detail. Robotic Coaxial Volumetric Velocimetry (CVV) is presented together with its working principle.

Following the description of the employed measuring technique, the experimental setup is illustrated in chapter 3, where also the parameters selected for the acquisitions are addressed.

A very brief discussion on the adopted data reduction techniques are outlined as well in chapter 4

Concluded this preliminary part, the results concerning the performances of the measurement system and the flow field of the Ahmed body are presented and discussed in chapter 5 and 6, respectively.

In chapter 5, indeed, the system intrusiveness is quantified in terms of velocity and pressure perturbations. Not only the effects of the system on the surrounding free stream have been assessed but also its interference with the Ahmed model has been evaluated in order to operate the aero probe in a safe and non-intrusive position. Finally, dynamic spatial and velocity range of the system are evaluated.

Following, the second part of the results, which concerns the aerodynamic flow field of the Ahmed body, is presented in chapter 6. Firstly, the headwind case is validated against the experimental data provided by Lienhart & Becker (2003) and then the cross-wind cases are analyzed. Different x-planes are used to inspect and measure both the position and the dimension of the dominant vortical structures and such flow features are highlighted also in a three-dimensional manner. Moreover, for such cases, an original flow topology is proposed.

Finally, in chapter 7, the conclusions concerning both the flow field generated by the Ahmed body in steady cross-wind and the used novel experimental technique are drawn and recommendations are given to further improve future applications.

2

Robotic Coaxial Volumetric Velocimetry

In this chapter, a very brief description of the state-of-the-art of PIV techniques is presented before introducing the novel measurement technique employed in the present work. Coaxial Volumetric Velocimetry, indeed, is discussed together with its working principle and its peculiarities.

Contents

2.1 PIV Background

2.1.1 Planar PIV

In its first iteration, Particle Image Velocimetry has been a two-dimensional technique capable of measuring the two velocity components (2C) in a plane. The measurement plane is illuminated by means of a thin light sheet, usually generated through a pulsed laser. Light is scattered by the tracer particles advected by the flow and passing the illuminated region. The scattered light is therefore recorded by an imaging device orthogonal to the plane, typically a CCD or CMOS sensor camera. The images recorded by the sensor are divided in interrogation windows and the displacement of the particles is obtained by evaluating their position at two subsequent time instances by means of a cross-correlation analysis. By knowing the displacement of the particles and the separation time between the two images, the instantaneous velocity is obtained as the ratio of the aforementioned quantities. See figure 2.1 for a graphical representation of the just described planar PIV working principle.
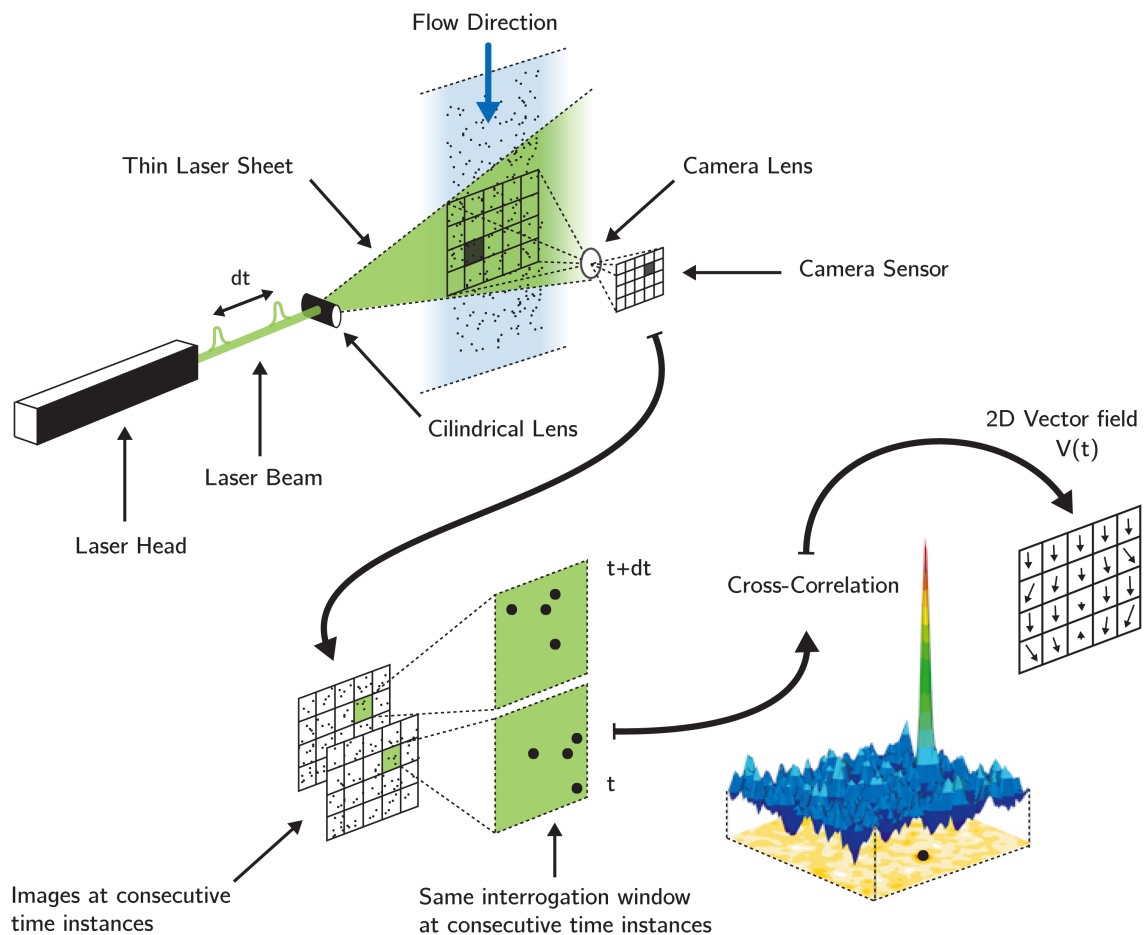
Figure 2.1: Working principle of Planar PIV.

2.1.2   Tomographic PIV

With the use of three or more cameras, a tomographic, or volumetric, approach can be exploited. This allowed for the first time the measurement of the three velocity components (3C) inside the investigated volume (3D) (Elsinga et al., 2006). The working principle is very similar to the one employed for planar PIV but it consists of a further step, namely a tomographic reconstruction. The three-dimensional position of all the particles, indeed, is reconstructed starting from the two-dimensional images captured by the single cameras so that the motion analysis can take place inside the investigated volume. As in planar PIV, the reconstructed volume is divided in now three-dimensional interrogation regions and cross-correlated with the subsequent time instance, to then obtain a three-dimensional velocity vector field (see figure 2.2).

The tomographic reconstruction step, however, is far from being straightforward and computationally inexpensive. For years, the most used method to solve the tomographic reconstruc-
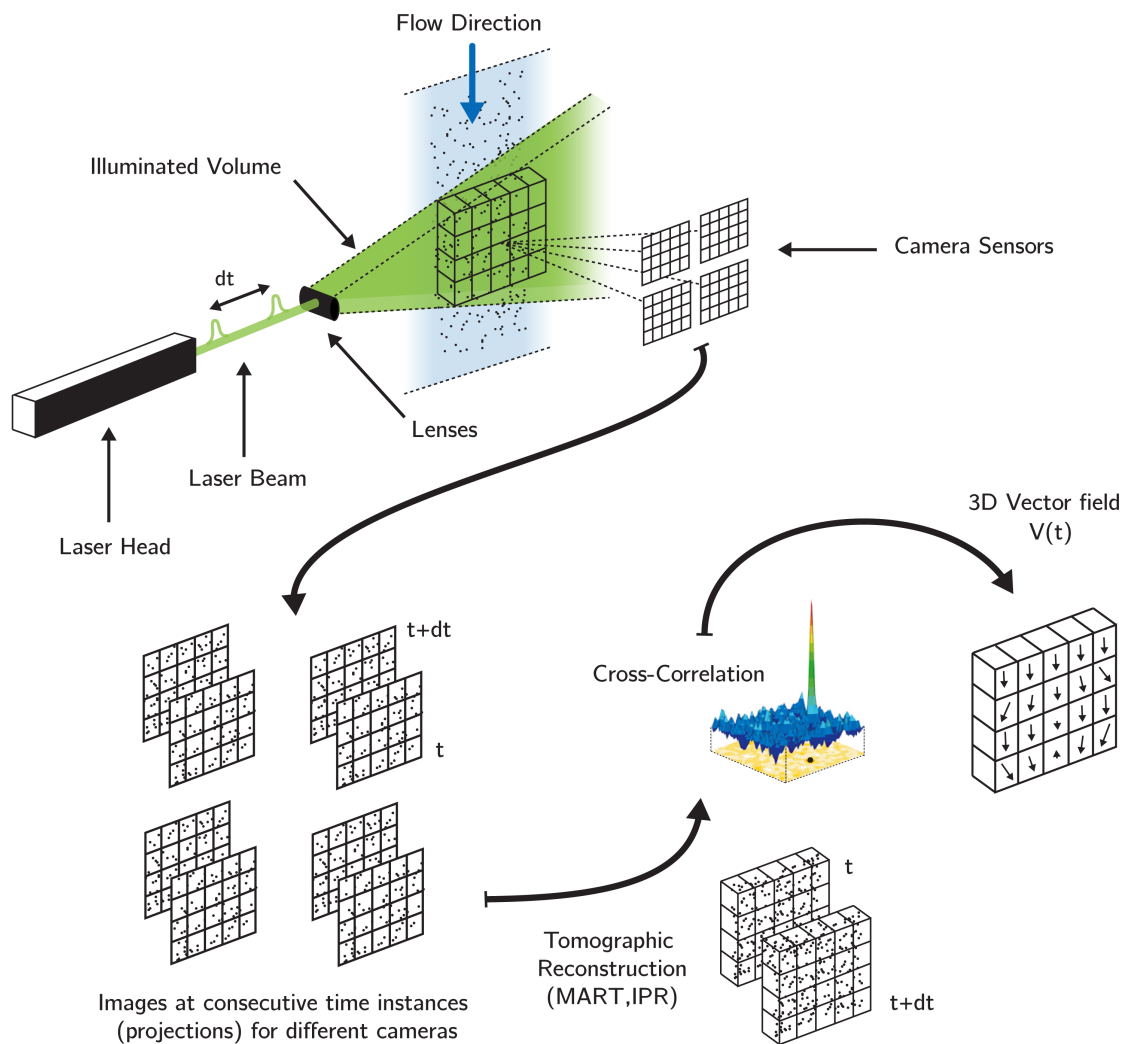
Figure 2.2: Working principle of Tomographic PIV.

tion problem has been the Multiplicative Algebraic Reconstruction Technique[1] (Herman & Lent, 1976). The MART approach consists of an iterative attempt to find the 3D light intensity distribution by starting from the intensity distributions of the 2D images. Although being the problem underdetermined, the MART algorithm is known for achieving a good accuracy and it is still used as reference technique to assess new reconstruction methods. Different reconstruction methods followed, with the main goal of reducing the computational resources required by the MART approach. In this respect, it is worth mentioning the Iterative Particle Reconstruction[2] technique introduced by Wieneke (2013). The IPR algorithm obtains the 3D particles distribution through particles triangulation and then it projects back the resulting particles onto the 2D images, in order to compute residual images. The positions can be iteratively improved through the information supplied by nonzero residual images and when the actual position is matched accurately, the information density of the residual image decreases and more particles can be triangulated. Not only the IPR approach proves to be very accurate but it also manages to work reliably at high information densities, up to 0.05 particles imaged per pixel (ppp) (Wieneke, 2013), concentration typical of volumetric PIV approaches (Scarano, 2013).

However, despite being considered the state-of-the-art of volumetric PIV, tomo-PIV still has some significant drawbacks which limit its applications. Not only the setup is complicated and often inappropriate for assuring good visual access around articulated geometries, but also the maximum measurable volume and the required processing time do not make the technique appealing outside of a purely academic environment.

2.1.3   Large Scale HFSB PIV

As just pointed out, despite being regarded as the breakthrough which allowed volumetric measurements, tomo-PIV is still limited in terms of dimensions of the investigated volume due to stringent illumination requirements. An effective solution, which finally allowed large-scale volumetric PIV measurements, has been proposed by Scarano et al. (2015) with the introduction of Helium Filled Soap Bubbles (HFSB) as tracer particles. As the illumination intensity is a critical parameter for volumetric PIV (Scarano, 2013), the leading idea has been to increase the light scattered by the tracer particles by means of an increase in the size of the particles. Although effective in terms of scattering, the increase in size of the tracers poses a problem concerning their capabilities to follow the flow accurately. Indeed, to be the motion of the tracer particles representative of the dynamics of the seeded flow, the difference between the motion of the particles and the fluid has to be negligible. For small spherical particles at very low Reynolds numbers, where the viscous forces are dominant over the inertial ones, the capability of following the flow is frequently evaluated in terms of slip velocity U_{slip} of the particles (Raffel et al., 2018):

$$U_{slip} = -\frac{d_p^2}{18} \frac{(\rho_p - \rho_f)}{\mu} \frac{dU}{dt} \tag{2.1}$$

where d_p is the diameter of the particles, ρ_p and ρ_f are the densities of particles and fluid, respectively, μ is the dynamic viscosity of the flow and eq. 2.1 is derived from the Stokes drag

---

[1]Hereafter referred to as MART
[2]Hereafter referred to as IPR

under the hypothesis of creeping flow ($Re \ll 1$). Given that the acceleration $\frac{dU}{dt}$ together with the density ρ_f and the dynamic viscosity μ are properties of the studied flow, to minimize the slip velocity only the two remaining parameters d_p and ρ_p can be adjusted. Since the size of the tracer particles d_p has been increased for scattering purposes, it is important to decrease the density of the tracers in order to match as close as possible the density of the fluid, achieving, in so doing, neutrally buoyant particles. As introduced by Scarano et al. (2015), HFSB consist of a mixture of water, glycerine and soap, called bubble fluid solution (BFS), filled with helium. With an average size of 300 μm, such tracer particles achieve a considerable light scattering potential[3]. Furthermore, by tuning the helium concentration, the particles can be made almost neutrally buoyant, which greatly reduces their slip velocity. With an estimated characteristic response time[4] of the order of 10 μs, HFSB have been therefore considered suitable for quantitative velocimetry in wind tunnel flows (Scarano et al., 2015).

2.1.4   Large Scale HFSB PTV

With the introduction of HFSB, one of the weak points of the tomographic PIV approach referred to in section 2.1.3, could, therefore, be addressed, finally delivering large-scale volumetric measurement. Another drawback, namely the demanding computational effort, has been tackled with the introduction by Schanz et al. (2013) of the novel Lagrangian Particle Tracking algorithm *Shake the Box*[5], presented in more details in section 2.2.5. The Particle Tracking Velocimetry[6] approach, differently from PIV, does not divide the acquired frames into interrogation windows to perform a cross-correlation analysis but it reconstructs instead the trajectories of the particles. If this produces clear advantages in terms of computational time for two-dimensional problems, it proves not as much efficient in three-dimensional environments, where a tomographic reconstruction must take place anyway. Furthermore, in order to properly trace the particles, the seeding concentration must be lower than the one typical of tomo-PIV measurements, which in turn reduces the spatial resolution. The advent of the STB algorithm addressed the aforementioned disadvantages, managing to exploit an intelligent predictor which allowed fast and precise track reconstructions at seeding concentration and spatial resolution comparable to tomo-PIV approaches. The reason for such a computational efficiency resides in the way STB operates. Such algorithm, indeed, performs a certain number of operations for each particle contained in the analysed frame. Contrarily, the usual PIV, or even PTV, algorithms do repeat the needed operations for each voxel the investigated volume is discretized with. The difference between the number of illuminated particles and the number of voxels discretizing the illuminated volume can often differ by up to three orders of magnitudes, justifying the considerable efficiency of the STB algorithm and therefore the convenience of a PTV approach in terms of computational requirements.

---

[3]Compared to conventional PIV micron-sized droplets, the scattering potential is increased by several orders of magnitude (Caridi et al., 2016; Schneiders, 2017).

[4]This quantity represents the time response of the tracer particles to a change in flow velocity. Such quantity is derived from the slip velocity and it is mainly due to the difference in density between the tracers and the fluid.

[5]Hereafter referred to as STB

[6]Hereafter referred to as PTV

2.2   CVV Principles

With respect to what outlined in section 2.1.3 concerning the limitations of three-dimensional PIV techniques, there is still an aspect which has not been addressed, yet. As quickly discussed, the size of the measurable volume has been increased with the introduction of HFSB as tracer particles. Moreover, the use of a particle tracking approach coupled with an efficient Lagrangian particle tracking algorithm decreased considerably the requirements in terms of processing effort. The last shortcoming, namely a complex setup and a limited visual access, is addressed with the introduction of the proposed Coaxial Volumetric Velocimetry approach.

A sketch illustrating the working principle of the CVV setup is presented in figure 2.3. Coaxial imaging and illumination are clear, despite the two-dimensional scheme. The tomographic cameras with low aperture lenses are packed inside a compact probe which makes the system suitable for robotic manipulation. Furthermore, the laser light is delivered from the laser to the centre of the probe through a flexible fibre optic cable. Clear differences with respect to a typical tomo-PIV setup are both the low tomographic aperture angle β and the large depth of field (DOF). Both the aforementioned features are responsible for a significant variation of light scattering intensity and magnification in depth. Such imaging properties, albeit quite unique,
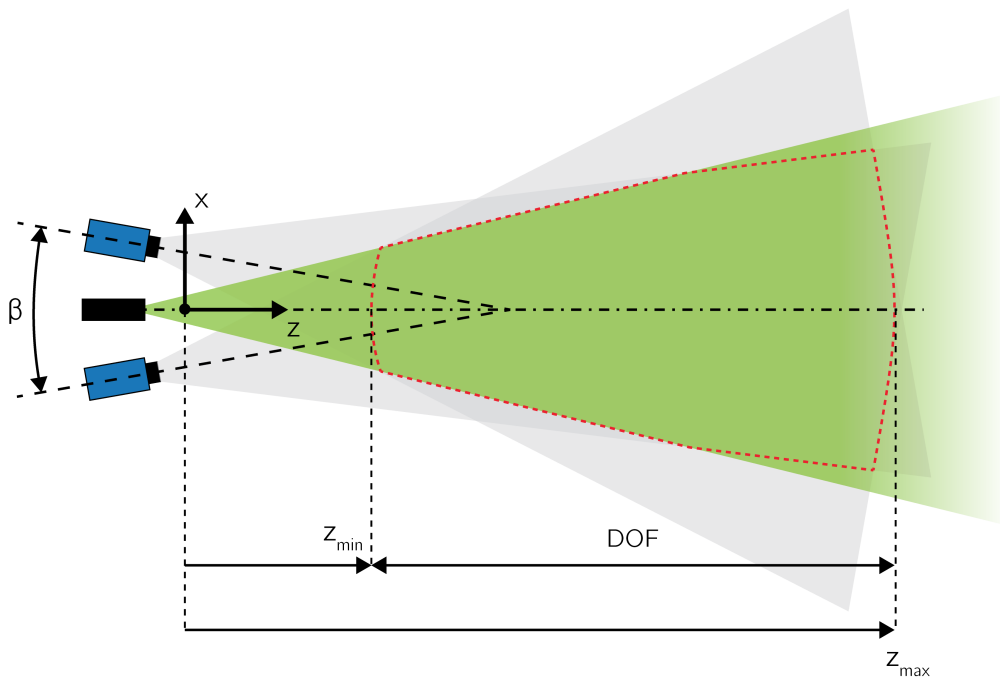
Figure 2.3: Working principle of CVV probe. Low aperture tomographic cameras (blue) are coaxial with light source (black) and illuminated volume (green). Measurements can take place inside volume resulting from the overlap of the field of view of the cameras (grey) and the illuminated region (dashed red contour). Figure adapted from Schneiders (2017).

are typical characteristics of the CVV technique.

The compactness and the convenience of the CVV probe, comprising both imaging and illumination devices, is evident when compared to a more complex typical tomographic setup. If to switch between two different typical tomographic setups can require hours, by means of robotic actuation, it just takes seconds to reposition the CVV probe. Furthermore, being the position of the four cameras fixed, relatively to each other, no further calibration is needed.

The notion of visual access, instead, could be not as straightforward as the simplification of the setup. To illustrate such concept, figure 2.4 depicts the differences between a CVV and a classical tomographic approach. For the sake of simplicity, just a cylinder is imaged and the representation is again two-dimensional. As it is easy to realize, the laser casts a shadowed cone behind the solid body. Even if visible from the cameras, such region cannot yield information about the flow since the particles are not illuminated and therefore do not scatter light. Similarly, each camera suffers from a blind region produced behind the body along the line of sight of the camera itself. As it can be seen from figure 2.4 (a), the small tomographic angle together with a reduced angle between the imaging and illumination directions manage to reduce the blind spot around the body of interest. This maximizes the size of the measurement volume (red), producing flow information also on the side of the cylinder. On the other hand, in figure 2.4 (b) a typical tomographic setup is reproduced. The combination of a greater tomographic angle and of a larger angle between imaging and illumination directions is responsible for a less comprehensive measurement volume together with the casting of a larger shadowed region. Although extremely simplified, figure 2.4 is still representative of the improved optical access provided by the proposed CVV configuration. Especially true for measurement entailing more complex bodies, the coaxial imaging and illumination technique allows a volumetric mapping of the volume around the studied object with fewer views compared to more classical tomographic approaches.

(a) CVV setup   (b) Typical tomo-PIV setup.
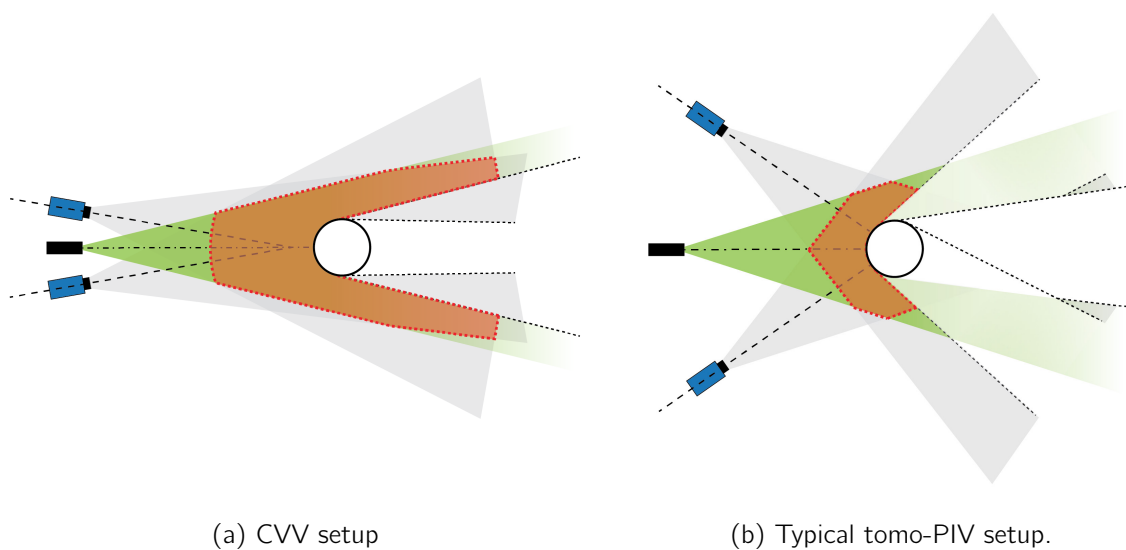
Figure 2.4: CVV approach vs classical tomographic setup: difference in visual access. Measurement volume is highlighted in red.

2.2.1   Low Tomographic Aperture and Measurement Uncertainty

Despite a low tomographic angle improves the optical access of the CVV probe, if compared to a more classical tomo-PIV setup, such low tomographic aperture introduces some disadvantages too. As deduced from a simple geometric analysis, and reported by Scarano (2013), the reconstructed particle resulting in a diamond-like shape elongates in depth with reducing the tomographic angle. This source of in-depth uncertainty is reproduced in figure 2.5 for a particle imaged at the centre of the sensor for two different tomographic aperture angles. When the particle is imaged far enough from the camera, the reconstructed diamond-like shape becomes approximately symmetric and banal trigonometric relations yields:

$$\frac{d_p}{d_z} \approx \tan\left(\frac{\beta}{2}\right) \quad \rightarrow \quad d_z \propto \frac{1}{\tan(\beta)} \quad \rightarrow \quad d_z \approx \frac{2}{\beta} \cdot d_p \quad \forall \beta \mid \beta \ll 1 \text{ rad} \qquad (2.2)$$

It is so demonstrated how the uncertainty in the in-depth position of the reconstructed particle is inversely proportional to the tomographic aperture angle. Moreover, the in-depth accuracy further decrease with increasing the distance of the particles from the cameras as this does contribute to generate an even smaller aperture between the lines of sight. Such effects have been modelled and successively experimentally measured by Schneiders (2017). The reconstructed d_z increases quadratically with the z-coordinate until reaching a maximum roughly in the middle of the measurement volume and stays thereafter constant. Furthermore, the reconstructed d_z decreases with moving away from the z-axis (Schneiders, 2017). However, through the Lagrangian particle tracking algorithm STB, the temporal information of the particle tracks can be utilized to reduce the uncertainty in the particle position. Assuming a random distribution in the reconstruction error of the particle position and fitting a polynomial through the estimated locations at consecutive time instants, the true trajectory of the particle can be obtained. The difference between the estimated position and the ideal trajectory can be used to quantify the uncertainty in the particle position. For the sake of giving an order of magnitude to such uncertainty, both Schneiders (2017) and Jux (2017) found approximately $\epsilon_x = \epsilon_y \leq 0.1$ mm and $\epsilon_z \leq 1$ mm.

(a) Small tomographic angle β_1.   (b) Large tomographic angle β_2.
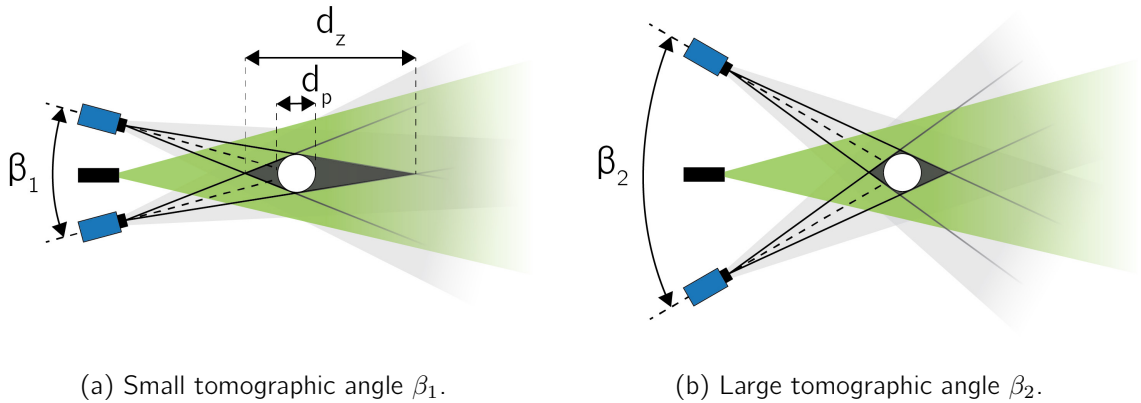
Figure 2.5: In-depth uncertainty due to tomographic angle β. Reference particle (white) and reconstructed particle (black). Figure adapted from Scarano (2013).

2.2.2 Large Depth of Field

Another singular feature due to the coaxial imaging and illumination setup is the large depth of field. Indeed, if for conventional tomographic PIV the measurable volume in depth is generally constrained by the thickness of the laser sheet, in a CVV approach it is mainly limited by the light source power. Because of a considerably higher illumination depth, the DOF is therefore accordingly increased, until becoming the dominant dimension characterizing the measurement volume.

As pointed out by Schneiders (2017), to avoid out-of-focus particles, the limits of the measurement volume, z_{min} and z_{max} (see figure 2.3), should be included by the near and far limits of the DOF, respectively D_N and D_F. Such values can be approximated by

$$D_N = \frac{H_d \cdot z_f}{H_d + z_f} \leq z_{min} \tag{2.3}$$

and

$$D_F = \frac{H_d \cdot z_f}{H_d - z_f} \geq z_{max} \tag{2.4}$$

for $z_f < H$, being z_f the focal plane depth and H the hyperfocal distance. For the CVV system H results

$$H_d = \frac{f^2}{f_\# \cdot d_\tau} \tag{2.5}$$

being f the focal length, function of the image and object distance, d_i and d_0 respectively

$$f = \frac{1}{d_i} + \frac{1}{d_0} \tag{2.6}$$

$f_\#$ the *f-stop* (or *f-number*) defined as the ratio between the focal length f and the aperture diameter D of the lens

$$f_\# = \frac{f}{D} \tag{2.7}$$

and d_τ the particle image size. The latter can be estimated, according to Raffel et al. (2018), as

$$d_\tau = \sqrt{(M \cdot d_p)^2 + \left(2.44 \cdot \lambda \cdot f_\# \cdot (M+1)\right)^2} \tag{2.8}$$

The first term in such equation defines the geometrical image particle diameter while the second one is the contribution due to diffraction effects. Being the magnification factor M, namely the ratio of image to object distance, not constant and comprised between 10^{-1} and 10^{-2} for the CVV system in use (Schneiders, 2017), the particle image size can be assumed to be dominated by diffraction effects. In so doing, equation 2.8 simplifies to

$$d_\tau = 2.44 \cdot \lambda \cdot f_\# \cdot (M+1) \tag{2.9}$$

Solving therefore equations 2.3, 2.4 and 2.5 for the minimum $f_\#$ produces:

$$z_f = \frac{2 \cdot z_{min} \cdot z_{max}}{z_{min} + z_{max}} \tag{2.10}$$

and

$$f_{\#,min} = \frac{1}{2} \cdot \frac{f^2}{d_\tau} \cdot \left(\frac{1}{z_{min}} - \frac{1}{z_{max}} \right) \tag{2.11}$$

For the experiment presented in this work, given the necessity of measuring from $z_{min} \approx 20$ cm to $z_{max} \approx 80$ cm the cameras have been focused to $z_f = 32$ cm, according to relation 2.10. As it can be inferred from such values, for the CVV system the focal plane should not be centred with respect to the measurement volume but indeed it should result closer to the near limit of the DOF, namely D_N. Finally, from equation 2.11, a minimum aperture of approximately $f_\# = 8$ resulted appropriate to image in focus the whole measurement volume.

2.2.3   Illumination and Scattering

As already introduced when presenting the CVV system, the laser light is delivered to the centre of the probe through a flexible fibre optic cable. The light then expands conically after a spherical lens. Differently from conventional tomographic PIV, the laser beam is not cut by means of knife edge filters to control the size of the measurement volume but it is free to expand at an angle θ_{vol}. The aforementioned angle should be large enough for the laser light to illuminate the whole field of view (FOV) of the imaging system. Under such hypothesis, the width and the height of the measurement volume, L_x and L_y respectively, are determined by the size of the sensor ($W_s \times H_s$) and the focal length f, such that

$$L_x(z) = \frac{W_s}{M(z)}, \qquad L_y(z) = \frac{H_s}{M(z)} \tag{2.12}$$

where the magnification factor, not constant for a CVV approach, is inversely proportional to the distance z:

$$M(z) = \frac{d_i}{z} \quad \rightarrow \quad M(z) \approx \frac{f}{z} \quad \forall M \mid M \ll 1. \tag{2.13}$$

The laser can therefore be focused in such a way as to cover the whole FOV of the cameras and the angle θ_{vol} of the illumination cone results

$$\theta_{vol} = 2 \cdot \arctan \left(\frac{L_x(z)}{2 \cdot z} \right) = 2 \cdot \arctan \left(\frac{W_s}{2 \cdot f} \right). \tag{2.14}$$

As pointed out by Schneiders (2017), other than on the correct lens focus setting, the capability of properly imaging the seeding particles and reconstructing their tracks also depends on the illumination source power and on the camera sensitivity. In fact, by considering the conical propagation of the laser and the spherical propagation of the light scattered back by a particle located at a distance z, according to Schneiders (2017), the light collected by the camera system, namely I_p, decreases with the fourth power of the distance of the particle:

$$I_p \propto \frac{1}{z^4} \tag{2.15}$$

Such scaling has been experimentally verified by Schneiders (2017). Finally, as introduced before, also the sensitivity of the imaging devices plays an important role in determining the minimum and maximum measurable depth, namely z_{min} and z_{max}. Indeed, removed the DOF constraints through a proper focus setting, if z_{max} is typically limited by the laser pulse energy I_0, z_{min} is influenced by the position where particle images begin to saturate the sensor. Such distance, namely z_{sat}, can be estimated by:

$$\frac{z_{max}}{z_{sat}} \propto \left(\frac{2^b}{I_{min}} \right)^{\frac{1}{4}} \tag{2.16}$$

being I_{min} the minimum particle image intensity detectable, b the bit depth of the camera sensor and the exponent $\frac{1}{4}$ derived from the forth order relation 2.15. For the present experiment, given a 10-bit camera sensor and a minimum level of detectability of approximately 20 counts, z_{min} and z_{max} do result $z_{min} = 20$ cm and $z_{max} = 75$ cm. Particles closer than approximately 20 cm, therefore, do produce images of saturated intensity.

2.2.4   Measurement Volume Size

Given the aforementioned limitations in terms of optical focus, laser pulse energy, particle image saturation and overlap between illumination and field of view of the cameras, the measurement volumes can be approximated with a truncated rectangular pyramid. The aspect ratio of the rectangular bases is dictated by the shape of the sensor, whether cropped or not, and for the present study it reaches the maximum dimensions of 30×25 cm. As for the height of the truncated pyramid, it extends roughly between $z_{min} = 20$ cm and $z_{max} = 75$ cm. In so doing, the measurement volume results of approximately 30 litres. Although being of the same order of more conventional large-scale HFSB tomographic PIV measurements (Caridi et al., 2016), the compactness of the system and its convenient positioning by means of robotic actuation makes it easy to map considerably bigger volumes (Jux et al., 2017).

2.2.5   Lagrangian Particle Tracking - STB

Two important benefits of a Lagrangian Particle Tracking approach have been already mentioned, namely the high computational speed in reconstructing the particle positions (2.1.4) and the increase of in-depth position accuracy, especially valuable for a CVV system (2.2.1). If in the past, PTV applicability has been limited to low seeding particle densities, with the introduction by Schanz et al. (2013) of the STB algorithm, seeding concentrations of the order of 0.05 ppp, typical of tomographic PIV, became possible, achieving a comparable spatial resolution. For the sake of completeness, a very short, and by no means exhaustive, introduction on the working principles STB is based on is given below. Furthermore, a schematic description of the salient stages is illustrated in figure 2.6. For a more detailed description, the reader is referred to the work of Schanz et al. (2016).

For the initialization of STB, when information of previous time instances is not available, conventional particle tracking algorithms, such as MART or IPR, are used to triangulate particles which can then generate particle tracks. Usually, three or four particles per track are considered

sufficient to predict accurately the position of the particle at the following time instance. Starting therefore from the particle positions at the time step t_n, their locations at t_{n+1} are predicted and, under the assumption of a small enough time step, such positions are expected to be very close to the actual ones. Each particle in the predicted set is then compared to the actual frame acquired at t_{n+1}: starting from the predicted location, image matching techniques are used and every particle is basically moved around (*shaking* process) until the actual position is found. Should more particles fall within the shaking range, conditions regarding light intensity or particle acceleration can be exploited to determine the most plausible pairing. Once paired successfully, the information about the particle is appended to the t_{n+1} frame and the particle is removed from the frame (residual image) in order to facilitate the triangulation of the remaining particles. After the shaking procedure, the remaining unpaired particles, likely to be new particle entering the measurement volume, are triangulated with the standard identification algorithms used for the initialization step. Finally, when the intensity falls below a certain threshold (usually 5% of the average particle intensity), the particle is assumed to be lost, it is deleted from the residual image and the track ends.

For the sake of completeness, a third advantage deriving from the use of STB must be mentioned. If compared to other reconstruction techniques, the STB algorithm, indeed, yields a decreased number of ghost particles, since their appearance is less likely to correlate over multiple consecutive time instances, creating a ghost track.
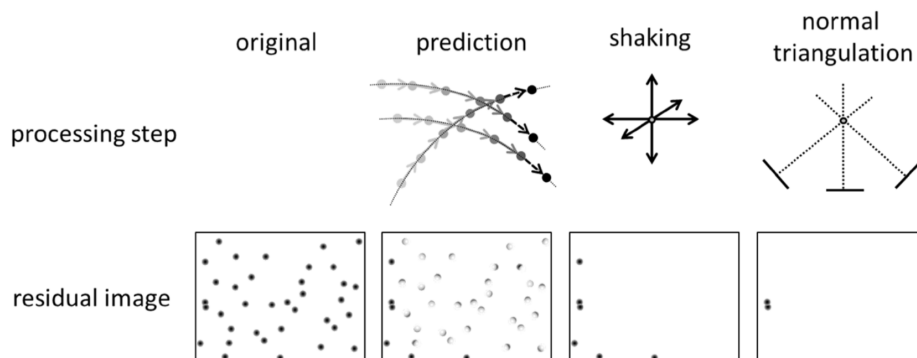
Figure 2.6: Schematic description of the STB procedure in its converged state. Effects of the different computational steps on the residual image of a single camera. Figure adapted from Schanz et al. (2016).

3

Experimental Setup and Procedures

In this chapter, the setup of the experiment, together with its design strategy are discussed. After presenting the involved hardware, for the sake of completeness, a few information about the system calibration are briefly mentioned. Moreover, the acquisition strategy and procedure are presented, in order to give the reader a better understanding of the whole experimental process.

Contents

3.1   Experimental Setup

As already introduced before, a 50% replica of the Ahmed body with a 25° slant angle has been investigated in different configurations, among which the headwind condition and two different yaw angles, namely $\beta_1 = +4°$ and $\beta_2 = +8°$.

The free-stream speed has been set to $U_\infty = 12$ m/s which corresponds to a height-based Reynolds number of 1.15×10^5. Such choice has been mainly dictated by the limited acquisition frequency of the CVV system which, without using particular techniques, cannot cope with excessive particle displacements from one frame to another. As already introduced in section 4.2, to alleviate such limitation, the camera sensors have been cropped to 700×420 px^2, which in turn increased the acquisition frequency to $f_{ac} = 700$ Hz. In so doing, the average free-stream particle displacement from one frame to another is limited to approximately $\delta_p = 65$ px which, according to the author's experience, fells inside the working range where STB performs robustly.

The second restriction in terms of Reynolds number is given by the size of the test object. The 50% scale, indeed, has been merely dictated by the availability of the item. However, according to the literature (see table 1.1), the generated wake topology is mainly governed by geometry-driven separation and only the Strouhal number of the main flow structures shows some very moderated Reynolds number effects (Vino et al., 2005; Zhang et al., 2015). Moreover, given that the proposed Reynolds number is of the same order of magnitude of the one in use by Lienhart & Becker (2003), main reference for the present study, the two aforementioned constraints have been deemed acceptable.

Both three-dimensional and two-dimensional representations of the experimental setup are proposed in figure 3.1(a) and (b), respectively.

3.1.1   Wind Tunnel

The experimental campaign has been performed in the Open Jet Facility (OJF) at the High-Speed Laboratories of TU Delft. The closed-loop, open test section wind tunnel provides a 3:1 contraction ratio[1] with an octagonal exit section of 2.85×2.85 m^2. The room including the test section is 13 m wide an 8 m height and it terminates with a cooling radiator mesh. The fan driven by a 500 kW electrical motor can speed up the airflow until reaching a maximum speed of 35 m/s. The nominal turbulence intensity of the free-stream is reported to be 0.5% (Lignarolo et al., 2014) even though this does not include the presence of the seeder in the settling chamber upstream of the acquisition domain, which is expected to raise the free-stream turbulence intensity.

3.1.2   Ahmed body

The test model is a 50% replica of the Ahmed reference model with a slant angle of 25 degrees. The model measures $522 \times 194.5 \times 144$ mm in length, width and height respectively. The slanted surface is 111 mm long while the front of the body is rounded with a radius of curvature of 50 mm. Zig-zag stripes are applied all around the frontal part of the body in order to trigger

---

[1]The horizontal contraction ratio of the OJF is 1.88 while the vertical one is 1.62, producing a total contraction of about 3.03.
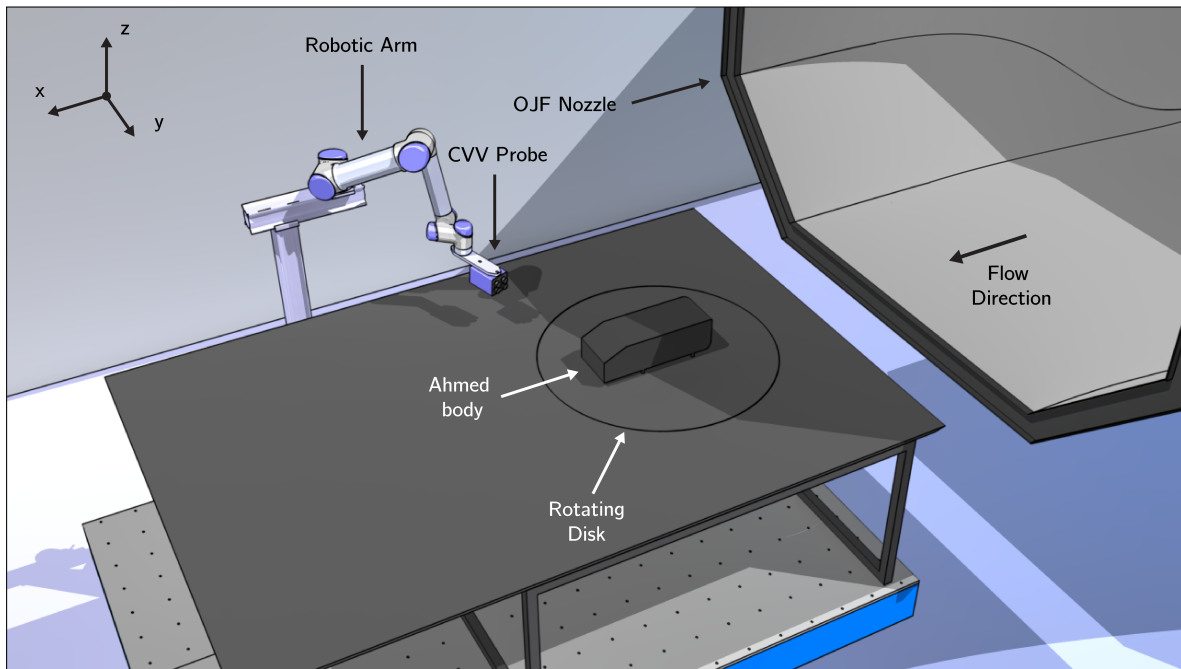
(a) 3D view.
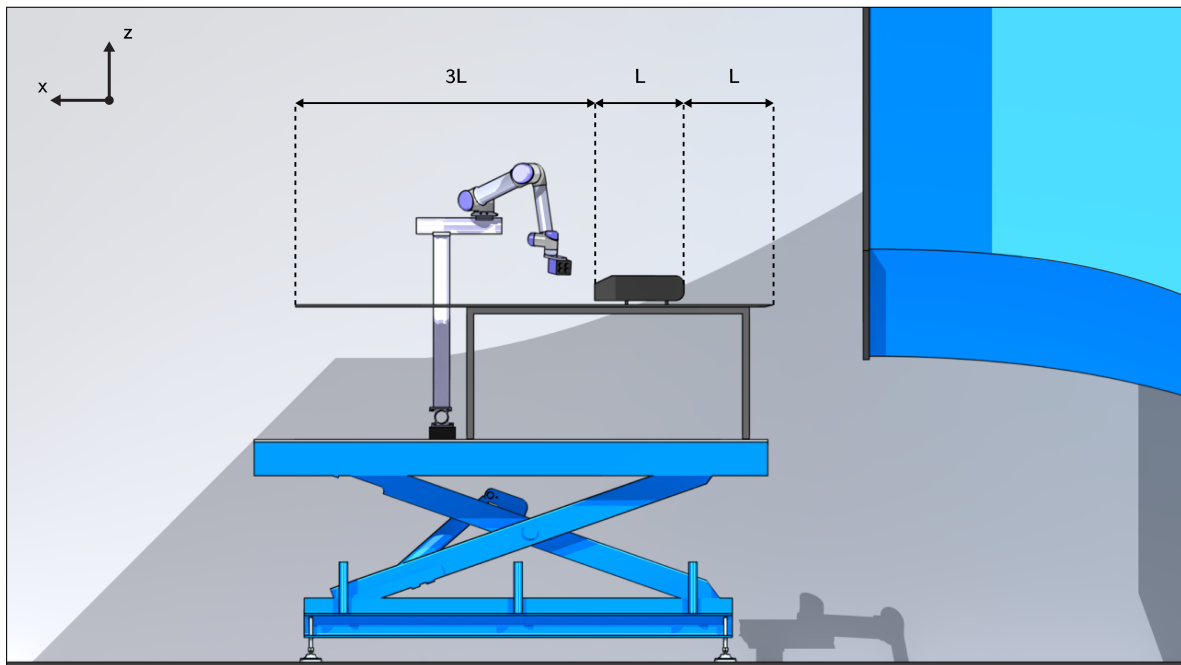
(b) Side view.

Figure 3.1: Experimental setup: OJF test section, Ahmed body, support table and rotating disk, robotic arm and CVV probe. Flow direction from right to left. 3D (a) and side view (b).

transition and obtain a turbulent boundary layer at the back of the body. In doing so, despite a lower Reynolds number if compared to the original experiment, a qualitatively similar boundary layer is expected. The model is supported by 4 circular stilts of 15 mm diameter which generate a clearance from the ground of 25mm. The stilts are connected to a disk that can be rotated in order to reproduce the different yaw angles. Such disk belongs to a raised floor which extends one characteristic length upstream of the body and three lengths downstream of it, featuring a sharp leading edge for boundary layer control purposes.

3.1.3 Seeding Rake and Seeding Generator

The seeder has been designed by the Department of Aerodynamics of TU Delft and it consists of a rake of ten parallel wings of 1 m length with 20 nozzles each. Every wing, as well as every nozzle on each wing, are 5 cm apart from each other. The seeding rake, therefore, consists of a total of 200 nozzles seeding a surface of approximately 0.95×0.50 m^2. Inside the nozzles, Helium, Air and Soap are mixed to form the HFSB particles. Every nozzle has a theoretical maximum production rate of 30.000 bubbles per second, although a more representative estimation of a nominal working condition is on the order of 3.000 bubbles per second. Helium, Air and Soap are supplied to the seeding rake by a *LaVision* Fluid Supply Unit (FSU). The pressures of the three components are controlled by three different valves and for the present experiment Helium, Air and Soap pressures have been set to 2.0, 1.5 and 2.0 bar The seeding rake has been placed inside the settling chamber in horizontal position, centred with respect to the centre line of the settling chamber. The lowest wing has a clearance with respect to the ground of 20 cm. As the reader can easily realize, the main reason for collocating the seeder inside the settling chamber concerns the reduction of the produced turbulence by exploiting the wind tunnel contraction. Given the dimensions of the seeding rake, the cross-section of the seeded region inside the settling chamber, before the contraction, measures approximately 95×50 cm^2 while after the contraction it reduces to about 50×30 cm^2, according to the aforementioned horizontal and vertical contraction ratios. However, because of the influence of the Ahmed body, the stream tube representing the seeded region is modified. The width, corrected for the presence of the test object, can be easily inferred from the traces of soap on the floor and the height can be worked out through continuity considerations. Nevertheless, the real dimensions have been measured with the CVV system, immediately downstream the Ahmed body where the cross-section of the seeded region resulted roughly 58×31 cm^2.

As per the nominal seeding concentration C_{HFSB}, before the experiment the seeding rake has been tested in order to assess its working state. Out of the 200 nozzles, 25 have been found not properly working. Considering an average bubbles generation rate of the order of 3.000 bubble/s per each working nozzle, an estimation of the expected average seeding concentration can be easily calculated. By using, indeed, the area of the seeded region immediately downstream the seeder,

$$A_s = 95 \times 50 = 4500 \text{ [cm}^2\text{]},\tag{3.1}$$

and remembering that, given the free-stream velocity $U_\infty = 12$ m/s and the contraction ratio of the wind tunnel, the flow speed inside the settling chamber is only $U_s = 4$ m/s, the seeder

volumetric flow rate $\dot{V}_s$ results

$$\dot{V}_s = A_s \times U_s = 4500 \times 400 = 1.8 \times 10^6 \text{ [cm}^3\text{/s]}. \tag{3.2}$$

The seeding concentration can, therefore, be obtained as the product between the number of working nozzles and the nozzle bubbles generation rate divided by the volumetric flow rate:

$$C_{HFSB} = \frac{175 \times 3000}{1.8 \times 10^6} = 0.29 \text{ [bubbles/cm}^3\text{]}. \tag{3.3}$$

However, the reader shall not forget the HFSB seeding quality and concentration can be controlled by means of the Helium, Air and Soap pressures supplied by the FSU. As already mentioned, an optimal setting for such pressures of 2, 1.5 and 2 bar, respectively, guarantees the production of neutrally buoyant tracers (Scarano et al., 2015; Morias et al., 2016) and generates an average imaged concentration of roughly 0.035 ppp, never exceeding the STB upper limit of 0.05 ppp (see figure 3.2).

Nominal Concentration (0.035 ppp)

Pressures [bar]:
He   2.0
Air   1.5
Soap 2.0

Too High Concentration (0.075 ppp)

Pressures [bar]:
He   2.0
Air   2.5
Soap 2.0
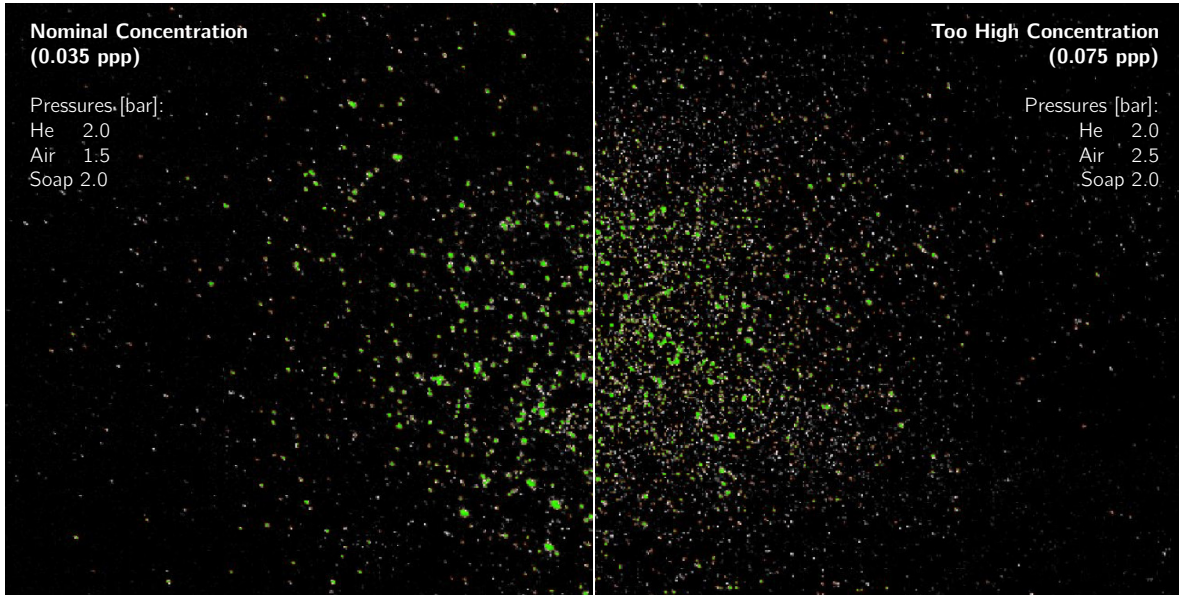
Figure 3.2: Seeding concentration comparison. Nominal seeding concentration at 0.035 ppp (left) and too high seeding concentration at 0.075 ppp (right). FSU pressures are also indicated.

3.1.4   Imaging System

The *LaVision MiniShaker S* probe (see figure 3.3) consists of four CMOS[2] sensor cameras packed together inside a compact prismatic body ($w \times h \times d : 13 \times 9 \times 8$ cm^3). The optical fibre runs through the whole probe, delivering the coaxial illumination. The cameras are characterized by a focal length $f = 4$ mm, the lens aperture can be adjusted from $f_{\#} = 4$ to $f_{\#} = 11$ while the tomographic aperture β of the cameras is $\beta = 4.3°$. The sensor size is 800×600 px^2 ($W \times H$) and it allows a maximum acquisition frequency at full sensor $f_{ac} = 511$ Hz. The size

---

[2]Acronym for Complementary Metal-Oxide-Semiconductor
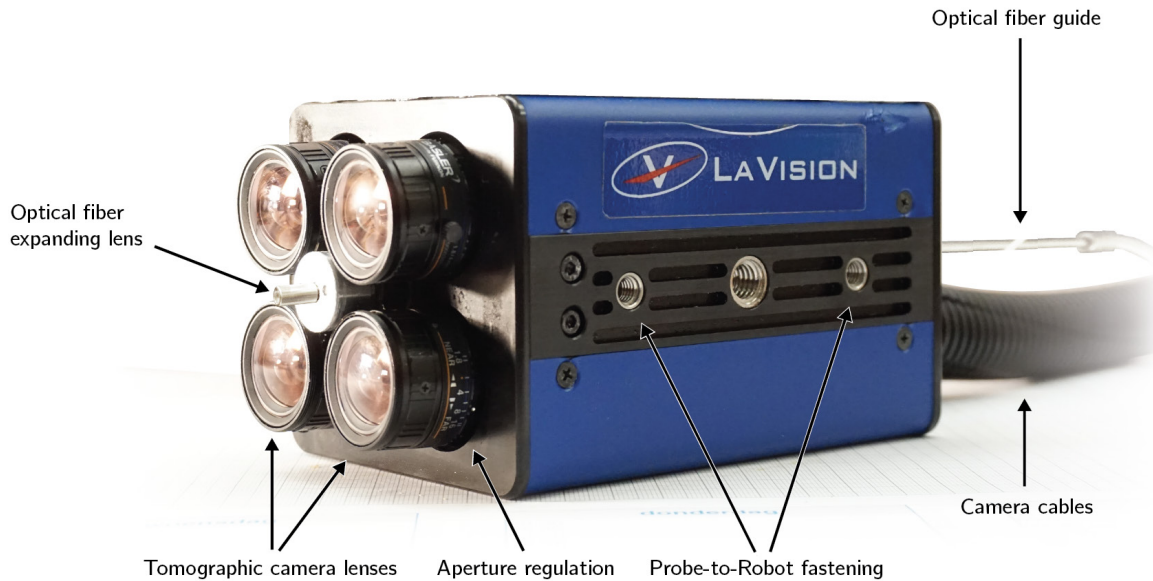
Figure 3.3: Coaxial Volumetric Velocimetry probe.

of the pixels, also known as pixel pitch, is $\Delta_{px} = 4.8$ μm. Finally the bit depth is $b = 10$ bits. The cameras are controlled by `DaVis 8.4.0` through an acquisition computer. The acquisition computer has an integrated Programmable Time Unit (PTU) which controls both the camera and the illumination systems. For the present experiment and a free-stream velocity of $U_{\infty} = 12$ m/s, the sensors of the camera system have been reduced to 700×420 px^2 in order to increase the acquisition frequency up to $f_{ac} = 700$ Hz and provide STB with optimal data. The lens aperture has been set to $f_{\#} = 8$ which allows to image in focus the whole width of the seeded region with maintaining the camera at a distance of 20 cm from the near limit of the seeded volume. This setup limits the intrusiveness of the probe and prevents the lenses from getting dirty because of the proximity with the seeding particles. The approach followed to properly set the focus and achieve the required DOF has been presented in section 2.2.2. Finally, the exposure time has been set to 59 μs.

3.1.5   Illumination

The light source consists of a high-speed laser *Quantronix Darwin Duo Nd:YLF*. The wavelength of the generated light is $\lambda = 527$ nm while the maximum power is of the order of 25 mJ, achieved with both cavities operating simultaneously. Both the laser head and its power supply are installed on one side of the measurement table. Furthermore, the laser light is delivered to the centre of the CVV probe through a 4m-long optical fibre coupled with the laser beam through a spherical converging lens in the proximity of the laser head. At the other end of the fibre, another spherical lens expands the light generating the conical illumination volume introduced in the previous chapter. As for the imaging system, also the laser pulses are triggered by the PTU

integrated into the acquisition computer and controlled with `DaVis 8.4.0`.

3.1.6 Acquisition PC

The acquisition computer features a double processor *Intel(R) Xeon(R) CPU E5-2650 v3 @ 2.30 GHz* with 64 GB of RAM and *Windows 7 Professional* (64-bit) as operative system. The system has a total of 20 physical cores (10 per each CPU) and 40 logical ones (2 per every physical core). To increase the data storing speed, the main hard drive consists of a solid state disk *SSD 850 PRO* with 512 of space. Further space is provided by a conventional 4 TB hard disk. The PC integrates a $LaVision$ PTU to control the cameras and laser light.

3.1.7 Robotic Arm

The orientation and the position in space of the CVV probe are controlled by means of a *Universal Robots - UR5* robotic arm, illustrated in figure 3.4. The robotic arm has a total of six joints and provides six degrees of freedom, namely three rotations and three translations. The maximum reach of the free extremity of the robot, named *tool* (a), is represented by the surface of a sphere of radius 85 cm centred in the other, fixed, end of the robot, named *base* (b). The motion around the *base* is controlled by two joints, delivering a pitching and a yawing movement and resulting in a ball and socket type of joint, resembling a human shoulder. Attached to the *shoulder* of the robot (c), two individual arms are connected by a single degree of freedom, which mimics
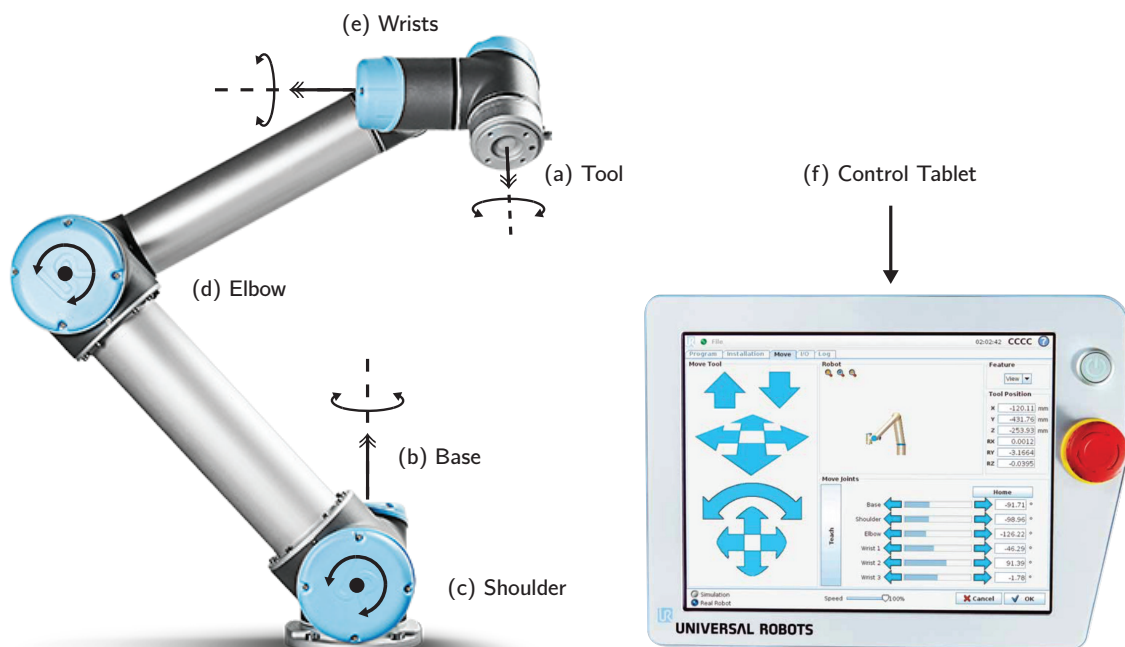
Figure 3.4: *Universal Robots - UR5* and its control tablet.

a human elbow (d). At the far end of such *arms*, three joints control the pitching, yawing and rolling motion of the *tool* where the CVV probe is attached, resembling a human wrist (e). The position of the tool can be controlled within a ± 0.01 mm and ± 0.01 deg precision, translation and rotation-wise, respectively. Moreover, each one of the joints of the robot allows for a $\pm 360°$ rotation range of movement with guaranteeing the repeatability of the *tool* position within ± 0.1 mm, according to the manufacturer. The robot position can be parametrically controlled by a tablet or through a pc, by means of self-tailored `python` scripts or third-party software, such as `RoboDK`. Furthermore, a so-called *collaborative* mode allows the user to manually position the robot arm. Indeed, if a parametric positioning of the CVV probe is the best way to always guarantee a minimum overlap between subsequent measurements, the manual positioning allowed by the *collaborative* mode permits to achieve quickly an approximative starting position together with a disposition of the *arms* which minimizes the aerodynamic intrusiveness of the whole system.

The robotic arm *Universal Robots - UR5* is installed on the side of the measurement table thanks to an x95 beams system (see figure 3.5). The base of the robot is positioned 50 cm above the measurement plane, 65 cm downstream the Ahmed body and 110 cm apart with respect to the symmetry plane (a). In such position, the CVV probe attached to the free end of the robot can easily sweep the volume past the rear portion of the test model and the relative wake. Moreover, in this position, the extrema of the camera system DOF do overlap with the whole width of the seeded region with maintaining the CVV probe 20 cm away from the seeding particles and a minimum of 44 cm away from the test object. In so doing, the acquisition volume is maximized with a limited intrusiveness of the measurement system. Furthermore, the robot always retains a minimum aperture between its arms in order to expose a reduced cross section to the flow and further minimizing the blockage. Finally, to investigate the whole length of the Ahmed body in the maximum crosswind configuration, the base of the robot, together with the whole x95 structure, has been shifted forward 60 cm (b). As a side note, during the whole testing campaign, the robot has been manoeuvred with the help of its tablet.

3.2   System Calibration

3.2.1   Geometric and Self-Calibration

To correctly triangulate the position of the imaged particle in a three-dimensional space, starting from a set of two-dimensional projections, an accurate optical calibration of the system in use is required. A first geometrical calibration (Soloff et al., 1997) has been performed with imaging at three different distances a *LaVision - Type 30* calibration plate[3]. Following the geo-calibration, a so-called volume self-calibration (Wieneke, 2008) has been applied. By looking at the disparity map resulting from the geometric calibration, at a distance of 40 cm from the cameras the maximum error is of the order of 1.2 px. Such error has been decreased by a factor 3 after the self-calibration, which disparity map shows a maximum error of 0.4 px at the same distance. On this refined calibration, an Optical Transfer Function[4] (Schanz et al., 2013) has been calculated which allows 3D particle triangulation starting from 2D projections. After this installation procedure, the system does not require any further calibration and it can be moved around through the robot, acquiring in minutes what would require otherwise hours and an entirely new setup with a conventional tomographic approach.

3.2.2   Robot Calibration

Apart from the optical one, also a different kind of calibration is needed given the use of a robotic arm. Indeed, since the acquired data are expressed with respect to the camera reference system XYZ_{camera}, to map such positions into a global reference frame XYZ_{global}, the relative position between the origin of the camera reference and of the rotation centre of the robot *tool* XYZ_{tool} is indispensable. Being such distance difficult to measure, a procedure to determine the relative shift between the two reference frames $\vec{x}_{cor}$ is therefore implemented (Jux, 2017). The used approach consists of imaging from different views the same black target with a certain number of white points (seven, for the present case). The positions of the white spots are reconstructed with STB and exported into `Matlab`. An iterative procedure then attempts at estimating the position of the sought rotation centre by systematically overlapping the different views and minimizing the residual error between the positions of the points. The resulting centre of rotation measured in mm with respect to the camera reference system[5], for the present setup results $\vec{x}_{cor} = [-9.6, -59.8, 554.3]$. The maximum in-plane positional uncertainty, given by the standard deviation in x and y, is of the order of 0.5 mm, while, the same value measured in depth, increases up to 2.5 mm. As expected, the uncertainty in z is the most significant, being driven by the small tomographic aperture of the camera system.

---

[3]The CVV probe has been aligned with the centre of the calibration plate and it has moved away from it, orthogonally, in order to acquire three different views of the plate at 150 mm, 350 mm and 550 mm of distance.

[4]Hereafter referred to as OTF.

[5]Note that the z-axis corresponds to the main CVV axis and it is positive when pointing towards the cameras.

3.3   Experimental Procedure

3.3.1   Measurement Position

The main acquisition strategy consisted in sweeping the volume downstream the Ahmed body to capture its wake. A first sweep consisting of three volumes has been achieved with translating each time the CVV probe of 10 cm in streamwise direction. The cameras have been therefore rotated downward and a second sweep, similar to the previous one, has been accomplished. The described vertical and horizontal movements are illustrated in figure 3.5 (a) and (b), respectively. As it can be seen from such drawings, a certain degree of pitch and yaw of the CVV probe has been maintained in order to improve the visual access around the rear of the Ahmed body and to reduce the reflections. Furthermore, when rotating the support disk, introducing a sideslip angle to reproduce the crosswind conditions, the rear part of the test object translates in y-direction. For such cases, the CVV probe is therefore translated accordingly in order to maintain the same distance from the Ahmed body. In order to investigate the whole length of the body for the maximum crosswind setpoint, the base of the robot has been translated forward of 60 cm (see position (b) of figure 3.5(b)). In so doing, the standard sweep has been extended upstream with a total of 8 extra measurements, namely 4 for volumes for each vertical position.

3.3.2   Sampling Strategy

To estimate in advance the minimum number of acquisitions required to reach a statistical convergence, the temporal information provided by the literature about the expected main flow structures can be exploited. According to Zhang et al. (2015), in good agreement with the majority of the literature and for the range of Reynolds numbers of interest, the Strouhal number of the slant recirculation bubble is found to be $St_{slant} = 0.20$. Similarly, the Sthroual number of the C-pillar vortices results $St_{vortex} = 0.27$, although the power spectral density function of the hot-wire signal shows also the second harmonic at $St_{vortex,2} = 0.53$. Finally, the wake behind the base and its pulsation have been measured at $St_{base} = 0.44$. From this data, the characteristic frequencies of every flow structure can be extrapolated, and therefore also a characteristic timescale. For this exercise, it is important to note how Zhang et al. (2015) do use the square root of the frontal area as a characteristic length scale, for the present case $l_{\sqrt{A}} = 167$ mm. The resulting frequency for the main flow structure of interest, namely the C-pillar vortices, is therefore

$$f_{vortex} = 19.4 \text{ Hz} \tag{3.4}$$

and the associated time scale

$$T_{vortex} = 0.05 \text{ s.} \tag{3.5}$$

As a side note, such integral time scale can also be obtained, *a posteriori*, through an autocorrelation analysis of the measured velocity signal. However, the number of uncorrelated samples can be estimated as the ratio between the acquisition period T_{ac} and the integral time scale of the flow structure of interest.
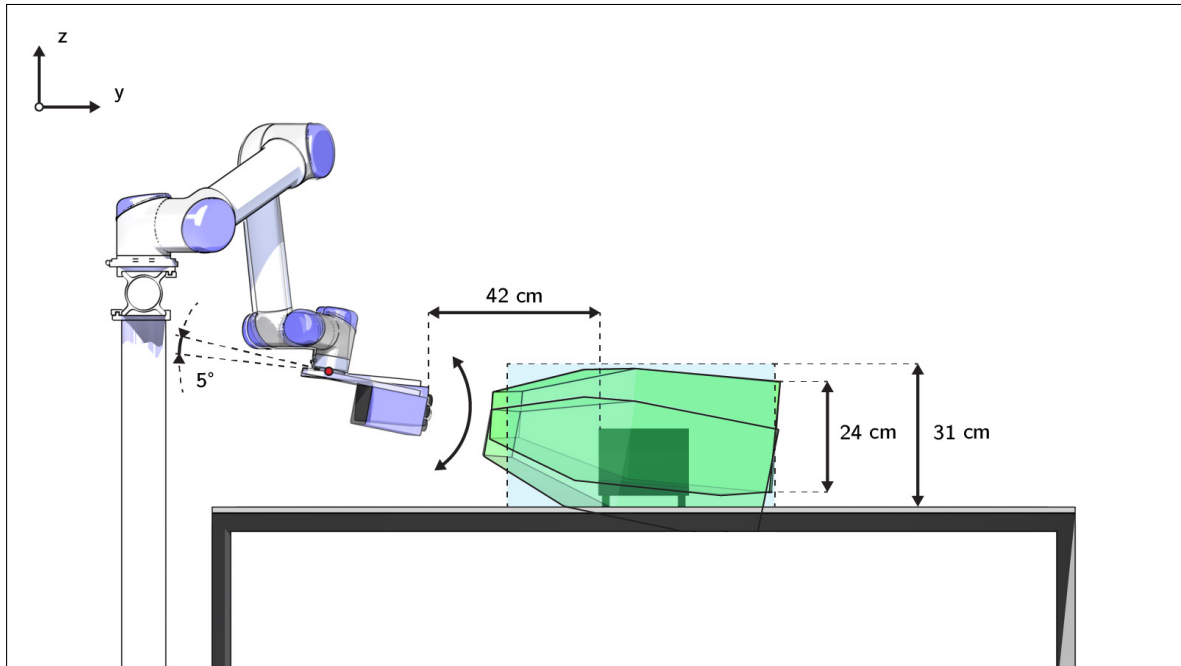
(a) View from the back.
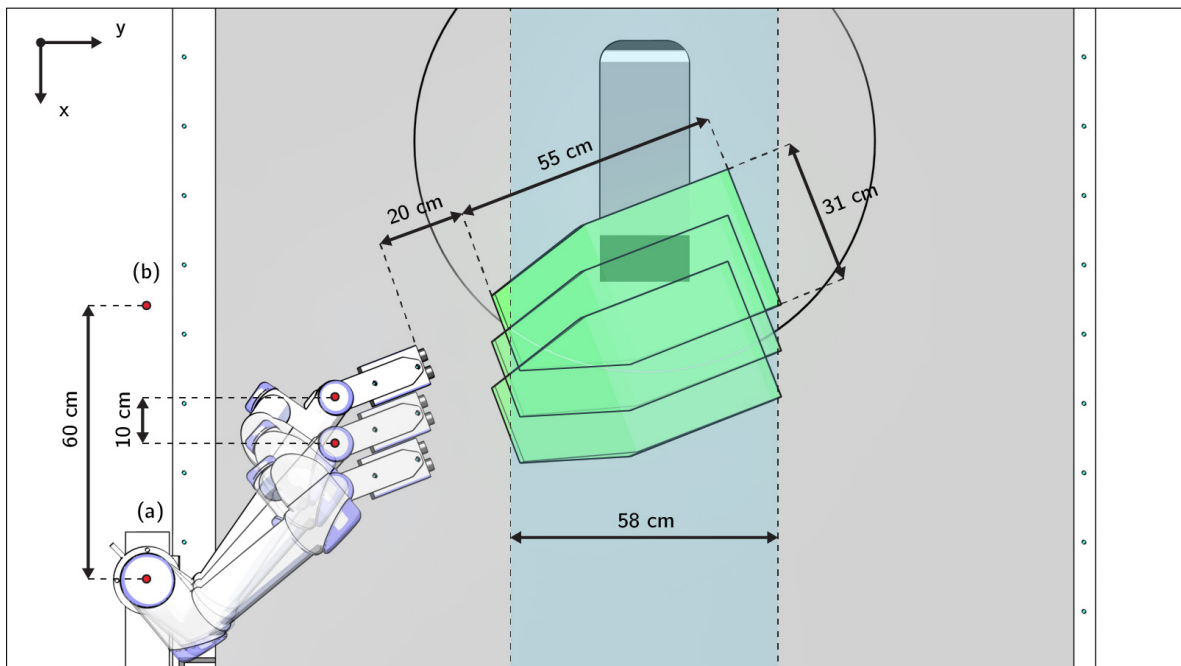
(b) View from the top.

Figure 3.5: Experimental setup, top and back views. Standard sweep, total of six volumes: three horizontal translations in x with two different vertical position in z. Rearward (a) and forward (b) positions of the robot base and seeded region (light blue) are also indicated.

Given the acquisition of 8,000 images at a frequency of $f_{ac} = 700$ Hz, the acquisition period results $T_{ac} = 11.43$ s. The uncorrelated observations measured over the acquisition period, given the acquisition frequency, therefore result

$$N_{vortex} = 228. \tag{3.6}$$

Recalling now the expression for the uncertainty, equation 4.3, the uncertainty for the measurement inside the vortex scales according to

$$\varepsilon_u \propto \frac{1}{\sqrt{N}}. \tag{3.7}$$

By using the average standard deviation inside the vortex measured by Lienhart & Becker (2003), i.e. $\sigma_{vortex} \approx 20\%$, it therefore results for the estimated uncertainty:

$$\varepsilon_{vortex} \approx \frac{\sigma_{vortex}}{\sqrt{N_{vortex}}} \approx 1.3\%. \tag{3.8}$$

However, it must be noted that the value computed above, does refer to an isolated measurement. According to figure 3.5(a), in the central part of the seeded region, where the wake resides, because of the vertical overlap of the measurement cones, a double number of uncorrelated samples is expected. Furthermore, according to figure 3.5(b), the horizontal overlap of the measurement volumes can increase the number of acquired samples up to three times the nominal value. In so doing, the minimum uncertainty can drop as much as

$$\varepsilon_{vortex,min} \approx 0.5\%. \tag{3.9}$$

Finally, as per section 3.1.3, given the expected seeding concentration of $C_{HFSB} = 0.29$ bubbles/cm^3, a preliminary bin size no smaller than $20 \times 20 \times 20$ mm^3 is chosen. In so doing, assuming a regular operation of the seeder, at least one seeding particle is expected per cubic cell at every recorded frame, generating, therefore, information at every time instance. For the sake of correctness, it must be stressed that such considerations are just an approximation. In fact, the seeding concentration may decrease in the low-speed wake of the test article as it is expected to increase because of the measurement overlap. An optimal bin size assessment is, therefore, necessary once the acquired data can be inspected (5.2).

3.3.3 Data Acquisition Procedure

After the initial installation, consisting of two optical calibrations (3.2.1) and a robotic one (3.2.2), the system is ready to be used without any further calibration required. The different steps of the data acquisition procedure are outlined below:

1. **CVV Probe Positioning**
   The velocimeter is moved, by means of the robot control tablet, in the desired position.

2. **Pre-Recording Check**
   The FOV is checked, together with the generated reflections due to the laser light. If the reflections exceed 256 counts, the probe is repositioned, usually introducing very small pitching and yawing angles.

3. **Position Recording**

   Once the operator is satisfied both with the FOV and the reflections, the view information, namely position and orientation of the robot *tool*, can be stored in a spreadsheet (see figure 3.6).

4. **Seeding Generation**

   The flow can be seeded with HFSB tracer particles by operating the FSU. Before data acquisition, the seeding concentration can be assessed by visual inspection.

5. **Data Acquisition**

   Once satisfied with the seeding concentration, data is acquired: 8,000 images are recorded at 700 Hz.

6. **Data Storing and Seeding Stop**

   The acquired data is quickly inspected. If deemed satisfactory, it is stored on the hard drive and the seeding generation is paused, differently, the data acquisition is repeated as per step (5).

The presented procedure has been optimized by pre-storing and checking all the necessary positions, with no wind. Once satisfied with the acquisition program, the wind tunnel and the seeding generation have been initiated and the aforementioned steps (1),(5) and (6) have been repeated multiple times. In so doing, a single user can operate the whole system, performing a run every three minutes approximately, while processing with STB the previous acquisition[6] to further check whether it needs to be repeated.

Acquisition Map

Run #	X	Y	Z	Rx	Ry	Rz	U [m/s]	XW [deg]	Slant [deg]	# Img	STB	Bin.	Description
		(base)			(base)			(Ahmed Ref)					
26	19.14	569.14	-250.05	172.50	0.00	-24.00	12	+4	25	8000	✔	☐	+4XW, High 1
27	19.14	569.14	-250.05	167.50	0.00	-24.00	12	+4	25	8000	✔	☐	+4XW, Low 1
28	89.85	498.43	-250.05	172.50	0.00	-24.00	12	+4	25	8000	✔	☐	+4XW, High 2
29	89.85	498.43	-250.05	167.50	0.00	-24.00	12	+4	25	8000	✔	☐	+4XW, Low 2
30	160.56	427.72	-250.05	172.50	0.00	-24.00	12	+4	25	8000	✔	☐	+4XW, High 3
31	160.56	427.72	-250.05	167.50	0.00	-24.00	12	+4	25	8000	✔	☐	+4XW, Low 3
32	33.28	583.28	-250.05	172.50	0.00	-24.00	12	+8	25	8000	✔	☐	+8XW, High 1, emptied return reservoir (almost full)
33	33.28	583.28	-250.05	167.50	0.00	-24.00	12	+8	25	8000	✔	☐	+8XW, Low 1
34	103.99	512.57	-250.05	172.50	0.00	-24.00	12	+8	25	8000	✔	☐	+8XW, High 2
35	103.99	512.57	-250.05	167.50	0.00	-24.00	12	+8	25	8000	☐	☐	+8XW, Low 2
36	174.70	441.86	-250.05	172.50	0.00	-24.00	12	+8	25	8000	✔	☐	+8XW, High 3
37	174.70	441.86	-250.05	167.50	0.00	-24.00	12	+8	25	8000	✔	☐	+8XW, Low 3, (finished @ 19.41), almost half return is full
38	75.71	484.29	-250.05	172.50	0.00	-24.00	12	0	25	8000	✔	☐	As Run 15, "SA, High 2", (refill soap reservoir), delta static pressure WT -1.5 Pa

Figure 3.6: Extrapolation of the spread sheet used as acquisition map.

---

[6]A very quick processing of 300 images only already gives the operator a decent idea of the acquisition quality and seeding concentration, with requiring no more than a couple of minutes.

4

Data Reduction Techniques

In this chapter, a strategy for the pre-processing of the images is discussed, together with the importance of such operation. Once prepared the data set for the particle tracking procedure, the settings of the used algorithm are presented. Generated the particle tracks with STB, data filtering and outlier detection are briefly discussed. The conversion of the processed data from a Lagrangian description to a Eulerian one, the so-called binning process, is introduced as well. Finally, for the sake of clarity, the whole data processing procedure is resumed.

Contents

Similarly to any other PIV or PTV investigation, the raw images resulting from the CVV acquisition system do portrait the investigated object, together with some background reflections and a multitude of tracers carried by the flow. Being the ultimate goal of the experimentalist the achievement of a velocity field, from which other properties, such as vorticity or pressure, can be derived, it should be immediately clear to the reader how far from trivial is to obtain such information starting from the available raw data. The steps required for achieving a structured velocity vector field starting from the recorded raw images are discussed below.

4.1   Image Pre-Processing

Even though, thanks to the use of the high scattering efficient HFSB, the light source power in use by the CVV system can be decreased, reducing accordingly background reflections, the resulting CVV raw images are not always and entirely reflection-free. When a pixel of the sensor is saturated by such reflections, any seeding particle passing by and imaged on the saturated pixel do not yield any useful information. Such kind of strong reflections, contributing to the image noise and promoting the reconstruction of stationary unphysical particles, must, therefore, be avoided when possible. However, less strong reflections and regular background noise can still be filtered by means of a proper image pre-processing. In this respect, Sciacchitano & Scarano (2014) proposed a novel approach for the elimination of PIV light reflection by means of a temporal high pass filter (HPF). The technique is based on the decomposition in the frequency domain of the pixel intensity. The high-frequency content of the signal, due to the transit of the tracer particles, is retained, whereas the low-frequencies, associated with the undesired reflections, are filtered out. For such purpose, the use of a third order Butterworth filter has been proposed (Sciacchitano & Scarano, 2014).

The instantaneous raw images as recorded by the CVV system (camera 1-to-3) are illustrated in figure 4.1, together with the result of the Butterworth filter (camera 4). As a side note, the reader can notice how barely perceivable the differences between the different views are because of the small tomographic angle of the CVV system. However, the reflections due to the solid edges of the body[1], as well as some background in the images, are easily noticeable in camera 1, 2 and 3. On the other hand, the Butterworth filter[2], applied on the raw image of camera 4, managed to effectively remove both the background image and the unwanted reflections. For the sake of completeness, it must be said that, albeit resulting saturated at the scale used in figure 4.1, the reflections do not appear to saturate the sensor if the scale is extended to 256 counts. Being the depth of the sensors in use of 10 bits, the pixel saturation is actually reached at $2^{10} = 1024$ counts and the seeding particles can, therefore, be successfully imaged and tracked. As a rule of thumb, with the aim of providing the STB algorithm with high-quality input images, whenever the reflections exceeded the 256 counts in the present acquisitions, the view (position and attitude) has been slightly adjusted in order to reduce the aforementioned reflections and consequently improve the recordings.

The pre-processed images are therefore ready to be processed with STB, in order to recon-

---

[1]The rear part of the Ahmed body is imaged from behind.
[2]Filter length of 7 recordings.
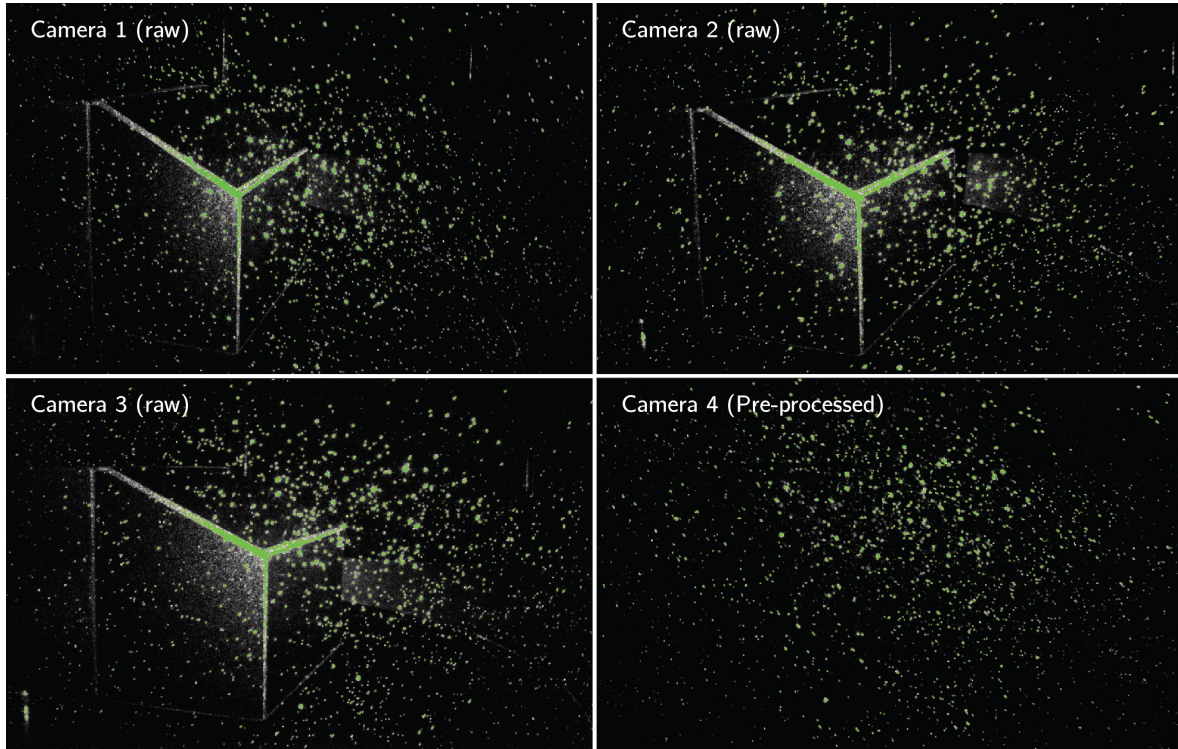
Figure 4.1: Raw instantaneous images from cameras 1 to 3 and Butterworth pre-processed image from camera 4 (bottom-right). Intensity scale 0 to 64 counts, black to green.

struct the tracks of the imaged seeding particles.

4.2 Particle Tracking - STB

The Butterworth-filtered images are then processed with the STB Lagrangian particle tracking algorithm (Schanz et al., 2016) implemented in `DaVis 8.4.0` by *LaVision*. The main idea when setting up STB main parameters is to provide tight enough limits to facilitate particle detection and tracking, speeding up the process, while leaving adequate room to the algorithm for capturing the different flow features investigated.

The first key parameter is the threshold intensity for 2D particle detection I_{min}. This parameter, depending on the noise level of the camera sensor, has been set to $I_{min} = 20$ counts. Every signal whose intensity falls under such threshold results indistinguishable from the background noise of the sensor.

The second important parameter is the allowed triangulation error ε_Δ. Schanz et al. (2016) suggests a working range of $0.5 \leq \varepsilon_\Delta \leq 1.5$ px, depending on the raw data quality. For the present setup, an average value of $\varepsilon_\Delta = 1$ px has been selected.

A third parameter, of paramount importance, is the maximum particle shift Δ_p. Given a cropped sensor acquisition frequency $f_{ac} = 700$ Hz, a particle moving with free stream velocity $U_\infty = 12$ m/s, moves approximately of 17 mm from one frame to another. Given for the present case a pixel size $l_{px} = 0.26$ mm, the expected displacement for a particle moving with

the free stream velocity is therefore 65 px/time-step. A maximum particle shift $\Delta_p = 75$ px has been therefore considered a good starting point, since allowing a 15% acceleration behind the free stream value with constraining the research radius for particles pairing to a sensible limit [3]. However, because of the deep measurement volume of the CVV system, the particle displacement in pixel varies significantly in depth. Given a cropped sensor size of 700×420 px^2, at the far end of the measurement volume $z_{max} = 75$ cm the FOV dimensions result approximately 31.5×23.5 cm^2 and the aforementioned free stream particle displacement is of the order of 34 px. On the other hand, at the nearest extreme of the measurement region, $z_{min} = 20$ cm, because of the smaller FOV of approximately 15×11 cm^2, the particle displacement increases to 72 px. An example of the tracks resulting from STB is proposed in figure 4.2.

For the sake of completeness, the remaining advanced settings are illustrated in figure 4.3. Should the reader be interested in a more advanced discussion on the algorithm parameters, interesting information can be found in the related literature (Schanz et al., 2016).
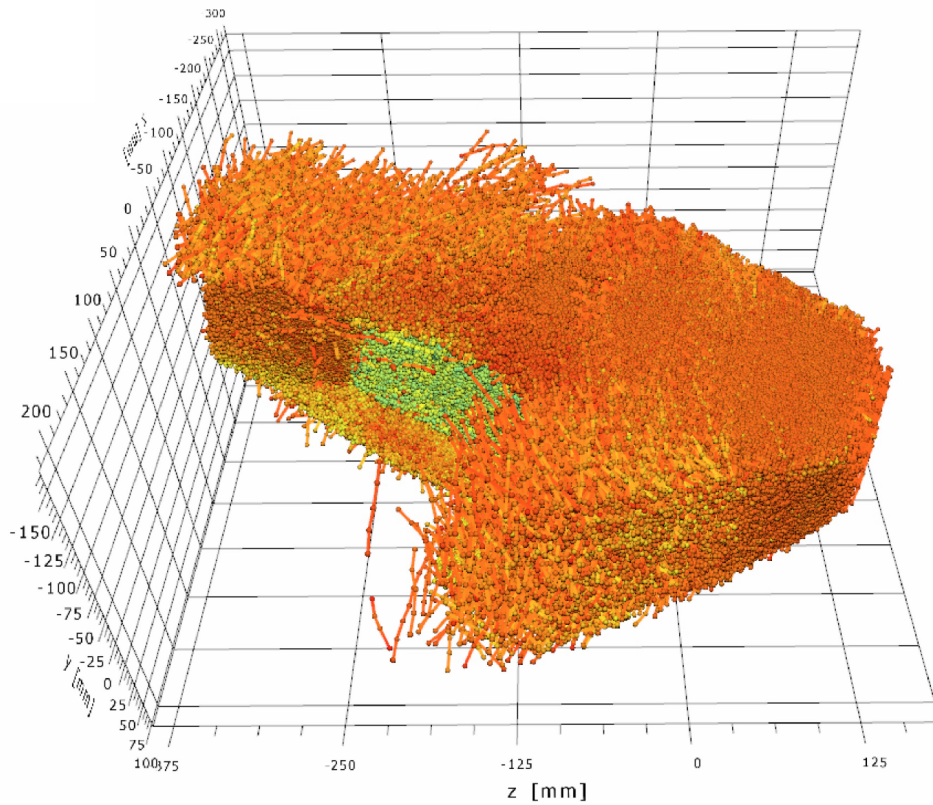
Figure 4.2: Particle tracks as generated by STB and coloured by velocity magnitude. The absence of tracks on the left-hand-side is caused by the presence of the rear part of the Ahmed body.

---

[3]An higher maximum particle shift, namely $\Delta_p = 85$ px, has been tested too, without noticing any relevant difference in the reconstructed tracks and a slightly longer processing time.
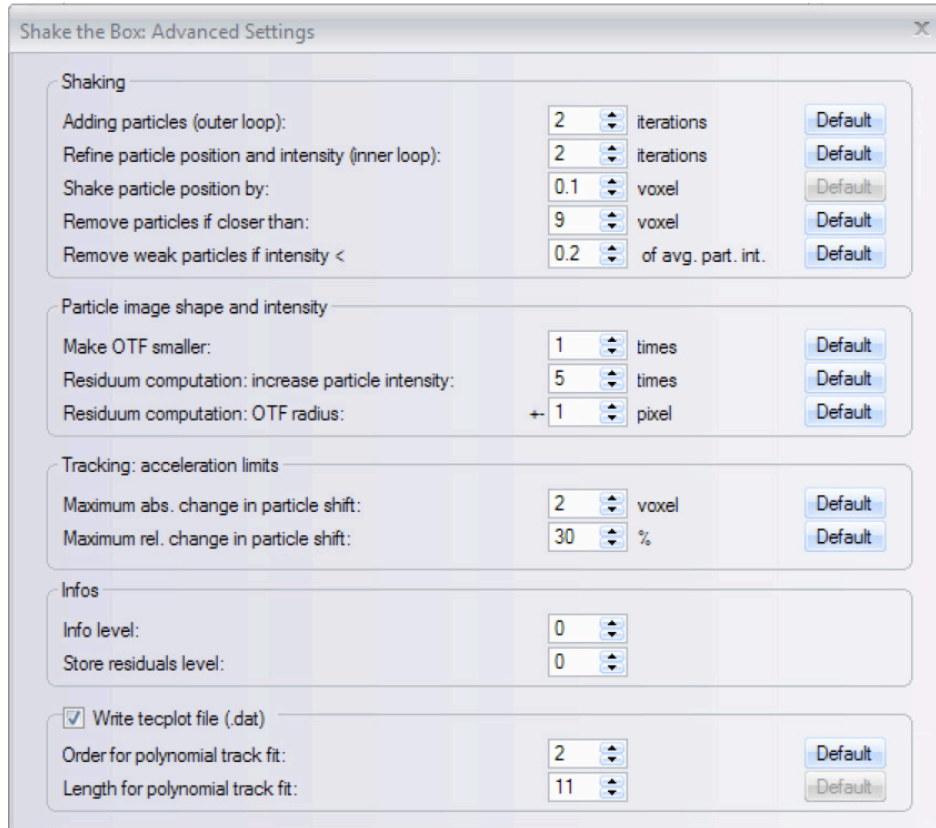
Figure 4.3: Shake the Box advanced settings window, `Davis 8.4.0`.

4.3 Data Filtering - Outlier Detection

Although a very robust and reliable processing technique, STB, as any other algorithm, is highly dependent on the quality of its input data and, as such, its results should not be regarded uncritically. As introduced before, noise sources, such as background reflections, can easily yield incorrect particles pairing and therefore generate spurious data. One of the most straightforward, yet effective, filtering approaches is the definition of a confidence interval, defined by a mean value and a range dependent on a standard deviation and a coverage factor. By using the instantaneous velocity u_i as filtering quantity, its mean $\bar{u}_i$ is defined by

$$\bar{u}_i = \frac{1}{N} \sum_{n=1}^{N} (u_i)_n \tag{4.1}$$

whereas its standard deviation σ_u results

$$\sigma_u = \sqrt{\frac{1}{N-1} \sum_{n=1}^{N} \left((u_i)_n - \bar{u}_i\right)^2} \ . \tag{4.2}$$

For the present application, a coverage factor $k = 3$ has been selected which provides a 99.7% confidence level. The confidence interval is therefore defined as $\bar{u}_i \pm 3\sigma$. All the data falling outside such interval are considered outliers and discharged during the grid conversion procedure.

4.4   Grid Conversion - Binning Process

As the data resulting from PTV is unstructured, being the tracer particles randomly distributed in space, it is convenient to convert the acquired information into a structured grid, passing, in so doing, from a Lagrangian to a Eulerian description of the velocity field. The resulting, structured, velocity field is obtained by ensemble averaging of the particles velocities inside interrogation volumes or bins. As a side remark, analogously to what commonly done with PIV data and interrogation windows, the bins do retain a certain degree of overlap which increases the vector pitch of the generated grid. However, it is of great importance to ensure the velocity estimate inside the bins is statistically converged. In this respect, principles and techniques for ensemble averaging have been recently extended to 3D PTV data by Agüera et al. (2016). Intuitively, the uncertainty in the velocity estimation ε_u is driven by the number of samples per cell:

$$\varepsilon_u = \frac{k\sigma_u}{\sqrt{N}} \ . \tag{4.3}$$

Moreover, reducing the size of the cell in the attempt of increasing the spatial resolution, reduces the number of samples contained in the cell, increasing accordingly the uncertainty. Indeed, given a seeding concentration C and a minimum number of measurements N_{min} within a bin, the number of needed uncorrelated samples N is inversely proportional to the bin characteristic dimension l_b:

$$l_b = \sqrt[3]{\frac{N_{min}}{N \cdot C}} \ . \tag{4.4}$$

However, it is important to remember that for time-resolved PTV measurements, the number of acquired images is unlikely to match the number of uncorrelated samples. Firstly, being the position of the tracers in the flow random, there is no guarantee to find a seeding particle inside every bin at every time instance. Furthermore, for unsteady flows with certain periodic characteristics, the acquired samples are likely to be correlated in time and space. Such considerations have been accounted for during the design of the present experiment and are presented section 3.1.

4.5   Data Processing Procedure

The data reduction procedure is quickly summarized below, for convenience:

1. **Raw Data Pre-Processing: Butterworth filter**
   The Raw images are pre-processed with a high-pass filter in order to remove background noise and reflections (4.1).

2. **Particle Tracking: STB**
   The pre-processed images are provided as input for STB which reconstructs the particles tracks (4.2).

3. **Outlier Detection**
   Spurious tracks are removed by applying filtering techniques (4.3).

4. **Grid Conversion: Binning**
   The data referred to the camera reference system XYZ_{camera} is converted into a global reference system XYZ_{global} aligned with the free-stream. The Lagrangian tracks representation is then mapped into a structured grid by means of ensemble averaging techniques and a time-averaged velocity field is obtained (4.4). The elementary grid element, cell or bin, consists of a cube of $20 \times 20 \times 20$ mm^3 with a 75% overlap, yielding a velocity vector field with a 5 mm vector pitch.

5. **Flowfield Analysis**
   Conventional flowfield analysis can, therefore, take place with common tools such as velocity and vorticity iso-surfaces, velocity and vector field representation, vortex detection, etc.

   To give the reader an order of magnitude of the time required for processing the data, with the acquisition computer, the 8,000 images of a single acquisition can be processed and binned in roughly 20 minutes. The average velocity field resulting from a whole sweep, consisting of six measurements, can be obtained in roughly 1.5 h.

Part II

Results and Discussion

5

Measurement System Performances

In this chapter the intrusiveness of the CVV system is assessed in terms of velocity and pressure perturbations and the interaction with the test article due to the system proximity is parametrically evaluated. The statistical convergence of the acquired data, as well as the effects of different binning element sizes, is presented as well. Finally, for the present experiment, the system resolution is quantified in terms of dynamic spatial range and dynamic velocity range.

Contents

5.1 System Intrusiveness

Differently from a more conventional PIV setup, for a CVV approach, the cameras are not far away from the measured region. In fact, usually, the CVV probe is even immersed in the flow and, as such, it modifies the flowfield in its proximity. When designing an experiment, the resulting interference must be, therefore, taken into account.

A first aerodynamic interference model is proposed by Jux (2017). Potential flow theory is exploited and the presence of the CVV probe is modelled by a 10 cm diameter sphere. The freestream solution and the dipole one, representing the sphere, are added together and the solution is expressed in a spherical coordinates frame. By normalizing the norm of the obtained perturbations by the magnitude of the freestream, the induced velocity error ε_v is obtained. The iso-surfaces of ε_v do consist of ellipsoids centred in the centre of the sphere and whose major axis is aligned with the freestream. Moreover, the velocity perturbation in the radial direction, V_R, decays with the inverse of the cube of the distance r, whereas in the tangential direction, V_τ, is proportional to the half of the just mentioned value:

$$\text{radial direction:} \quad V_R \propto \frac{1}{r^3} \tag{5.1}$$

$$\text{tangential direction:} \quad V_\tau \propto \frac{1}{2} \cdot \frac{1}{r^3} \tag{5.2}$$

Therefore, the maximum velocity deviation in the tangential direction, V_τ, is less severe than the equivalent in the radial direction, V_r. Finally, Jux (2017) suggests that, in order to keep the induced velocity error ε_v below 1%, the minimum measurement distance from the probe should not be lesser than 17.5 cm.

However, albeit useful for a first estimation of the interference generated by the probe, such approach has some serious limitations. Firstly, the assumption of potential flow, in the near proximity of a bluff body which is expected to show recirculation regions and a separated unsteady wake is rather optimistic. Moreover, the presented model does not take into account the presence of the robot tool, which, together with the adjoining wrist, basically doubles the cross-sectional area exposed to the flow.

Because of this, for the present investigation, a metal flange has been used to connect the CVV probe to the robot tool, increasing, therefore, the mutual distance and reducing the blockage created by the robot extremity. Furthermore, the perturbations generated by the measuring system have been assessed by inspecting a freestream measurement. Finally, the interaction due to the proximity of the test article has been quickly and parametrically investigated before performing the acquisition campaign.

5.1.1 Velocity Perturbation

A freestream acquisition has been performed with the camera orthogonal to the flow, namely pointing in the y-direction (see figure 5.1). A total of 5,000 images have been acquired and binned using a bin size of $30 \times 30 \times 30$ mm, resulting in a vector pitch of 7.5 mm. A larger bin size, if compared to the one proposed before (3.3.2), has been chosen because of a reduced
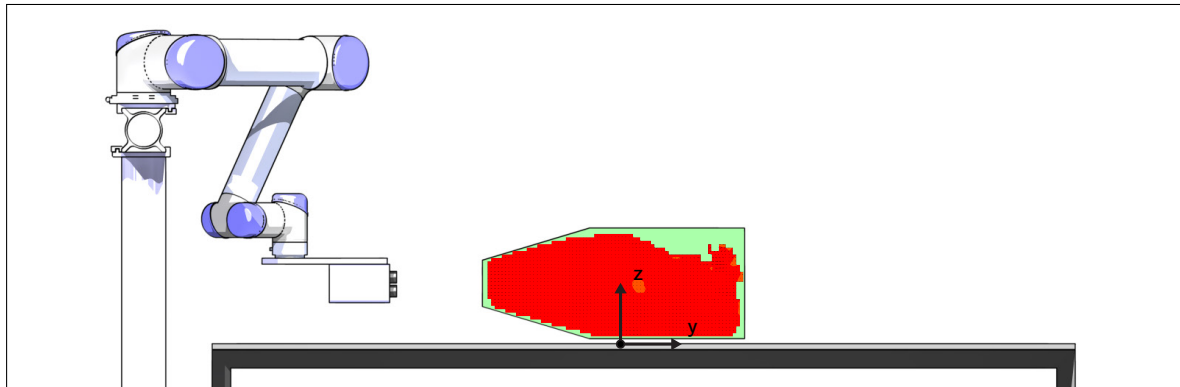
(a) View from the back.
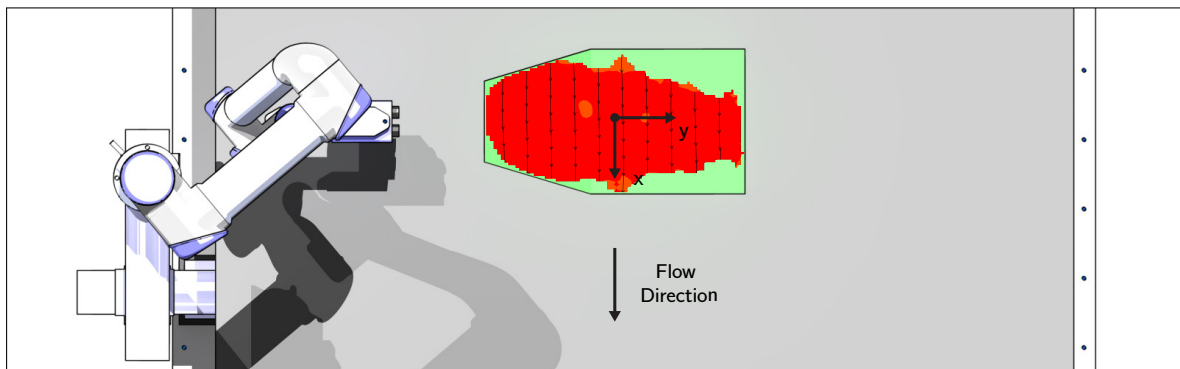
(b) View from the top.

Figure 5.1: Freestream acquisition setup, back (a) and top (b) views.

number of available samples [1].

Two cross-sections of the measured volume are presented in figure 5.2, namely a slice in x (a) and one in z (b), and are coloured by streamwise velocity magnitude U. The velocity vector field is also plotted on the x-plane (a) while some streamlines are appreciable from the z-plane top view (b). As it can be seen from such figures, the velocity field is rather homogeneous and in good agreement with what expected for a freestream $U_\infty \approx 12$ m/s. A more detailed analysis can be performed by narrowing the measurement scale, as per figure 5.3. In here, what seemed before a homogeneous velocity field actually shows a velocity gradient in y. The perturbations generated by the measurement system do reach the boundaries of the measurement volume, although moderately. To quantify the intrusiveness, two isolines have been highlighted, namely $U_a = 12.4$ m/s (a) and $U_b = 12.3$ m/s (b). Assuming an average measured freestream of $U_\infty = 12.15$ m/s, the induced velocity error ε_v results $\varepsilon_{v,a} = 2\%$ at location (a) while it fells below $\varepsilon_{v,b} = 1\%$ behind isoline (b).

---

[1]Other than 5,000 images, no overlap with other measurements is applicable.
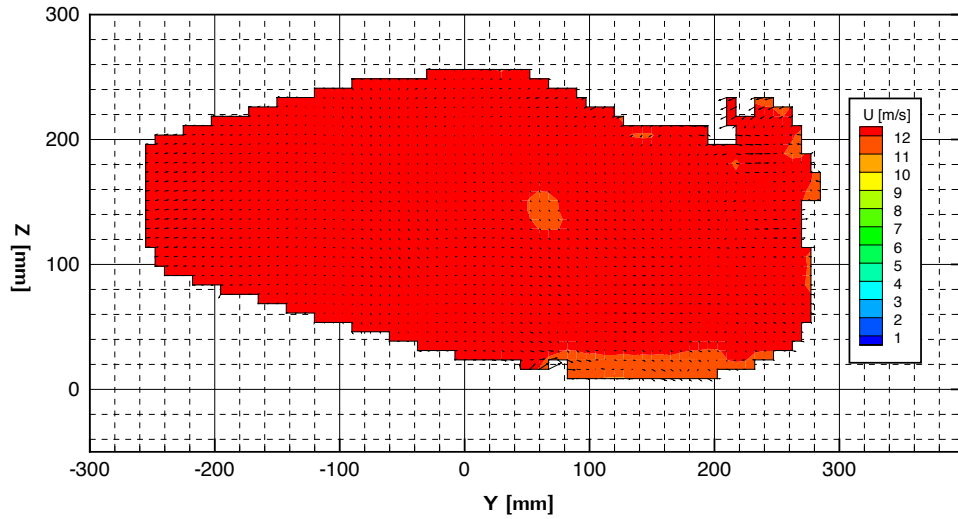
(a) Front view.
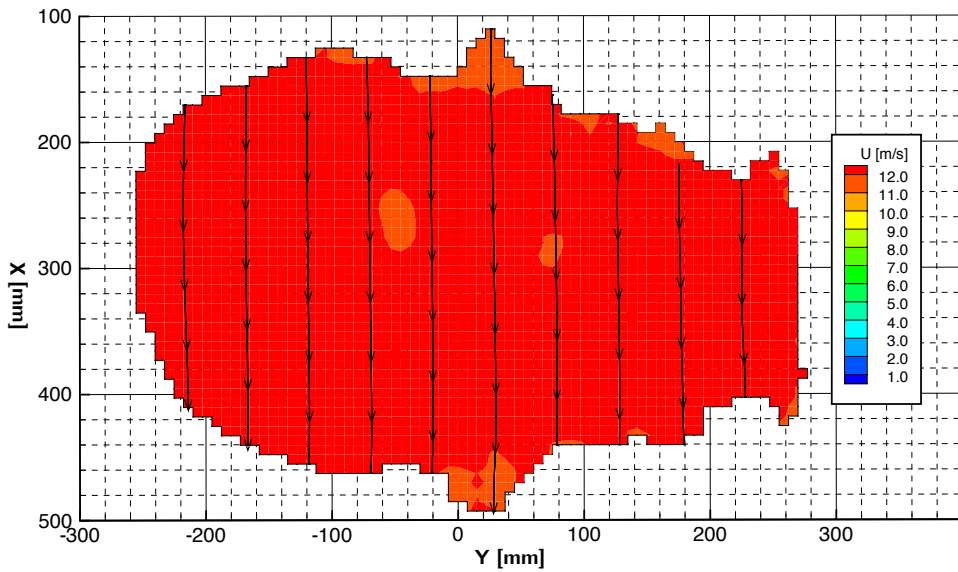
(b) Top view.

Figure 5.2: Freestream measurement, contours of streamwise velocity magnitude U_x, velocity vector field and streamlines. Central x-plane (a) and z-plane (b). Cameras located at $y = -450$ mm.

Recalling now that, because of the focus settings, the CVV systems begins to record at a distance of 20 cm from the cameras, according to figure 5.3 (b) the maximum measured velocity error falls below $\varepsilon_v = 1\%$ at approximately 32 cm from the probe. It is therefore recommended to position the measuring system at least 32 cm away from the region of interest. As expected, such distance results considerably larger than the one suggested by Jux (2017).
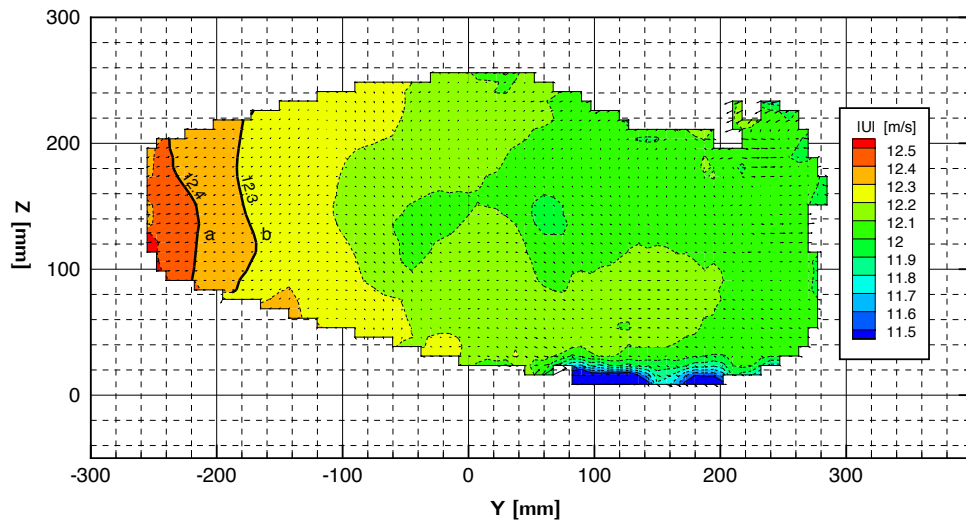
(a) Front view.
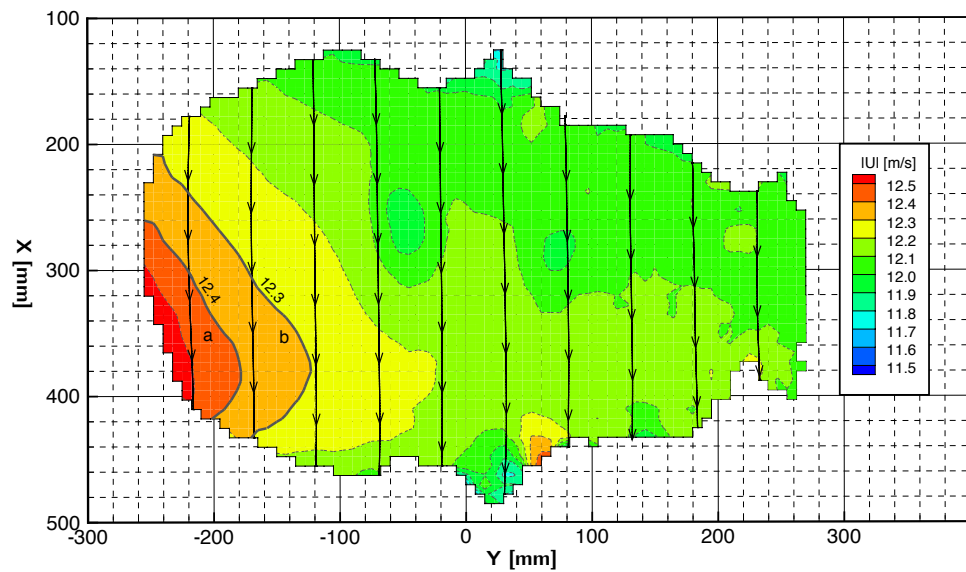
(b) Top view.

Figure 5.3: Freestream measurement, contours of velocity magnitude U, velocity vector field and streamlines. Central x-plane (a) and z-plane (b). Narrower contours scale.

Furthermore, to quantify the freestream turbulence level, the standard deviation of the velocity has been integrated over a $50 \times 50 \times 50$ mm domain yielding a mean value $\overline{\sigma}_{u,x} = 0.1$ m/s, equivalent to $\overline{\sigma}_{u,x} = 0.8$ %. Such magnitude, almost two times the nominal turbulence intensity level of the OJF wind tunnel, is less than a half of the one measured by Jux (2017) with the seeder in the test section, just in front of the test object. As expected, the collocation of the seeding rake inside the settling chamber appreciably reduced the generated turbulence.

5.1.2 Pressure Perturbation

Similarly to what done with the velocity, also the static pressure has been investigated and it is proposed in figure 5.4. Under the assumption of incompressible potential flow, the static pressure P has been computed starting from the velocity field, according to Bernoulli:

$$P = P_\infty + \frac{1}{2}\rho_\infty \left(U_\infty^2 - U^2 \right) \tag{5.3}$$
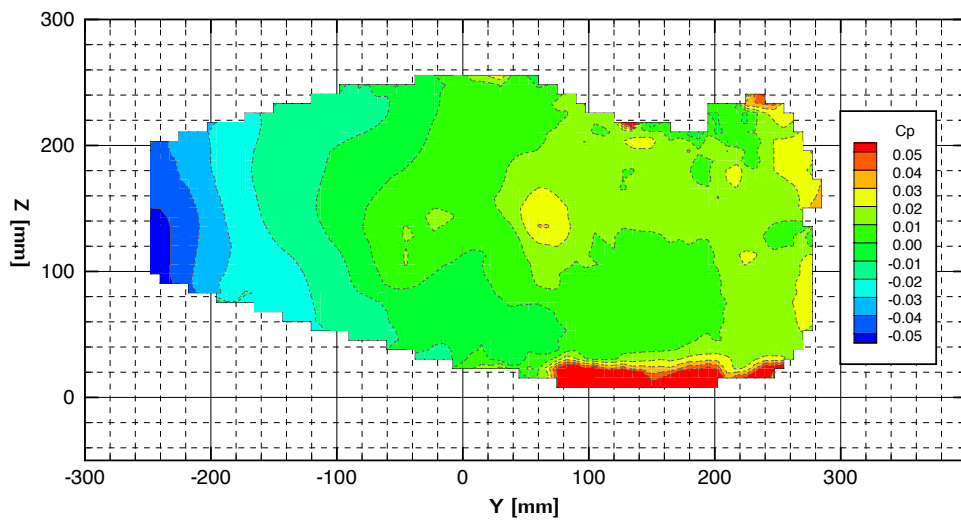
(a) Front view.
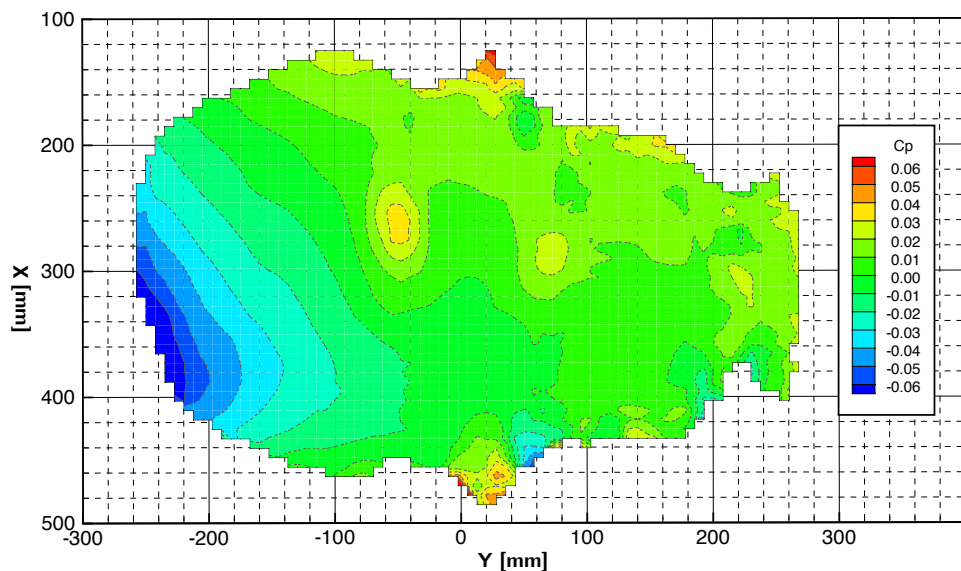
(b) Top view.

Figure 5.4: Freestream measurement, contours of static pressure coefficient Cp. Central x-plane (a) and z-plane (b).

being $P_\infty = 101,325$ Pa and $\rho_\infty = 1.225$ kg/m^3. Under such hypothesis, the static pressure coefficient is given by:

$$Cp = 1 - \left(\frac{U}{U_\infty}\right)^2.$$ (5.4)

According to figure 5.4, as expected, the Cp contours deviate from the freestream value when approaching to the CVV probe, in agreement with the measured velocity field. Where the streamwise velocity increases, the static pressure decreases and the Cp drops under zero. As a reference, according to equation 5.4, when the velocity error equals $\varepsilon_v = 1\%$, the pressure coefficient results $Cp = -0.02$. As a side note, with respect to the moderate noise present at the centre of the cone, it is most likely due to seeder not working steadily in its early stages and the resulting seeding concentration exceeding temporarily the STB maximum threshold[2].

5.1.3 Proximity Interaction

Once evaluated the magnitude of the perturbation induced on the freestream by the presence of the measuring system, the interaction with the test object is assessed as well. The CVV probe is placed slightly downstream the Ahmed body, in a plausible acquisition position to capture the two C-pillar vortices downstream the base surface. The cameras are then translated twice in y-direction away from the body as illustrated in figure 5.5. In the nearest position, the probe front surface is 30 cm apart, in y, from the lateral surface of the Ahmed body, while in the farthest position the distance between the cameras and the test article reaches 50 cm.
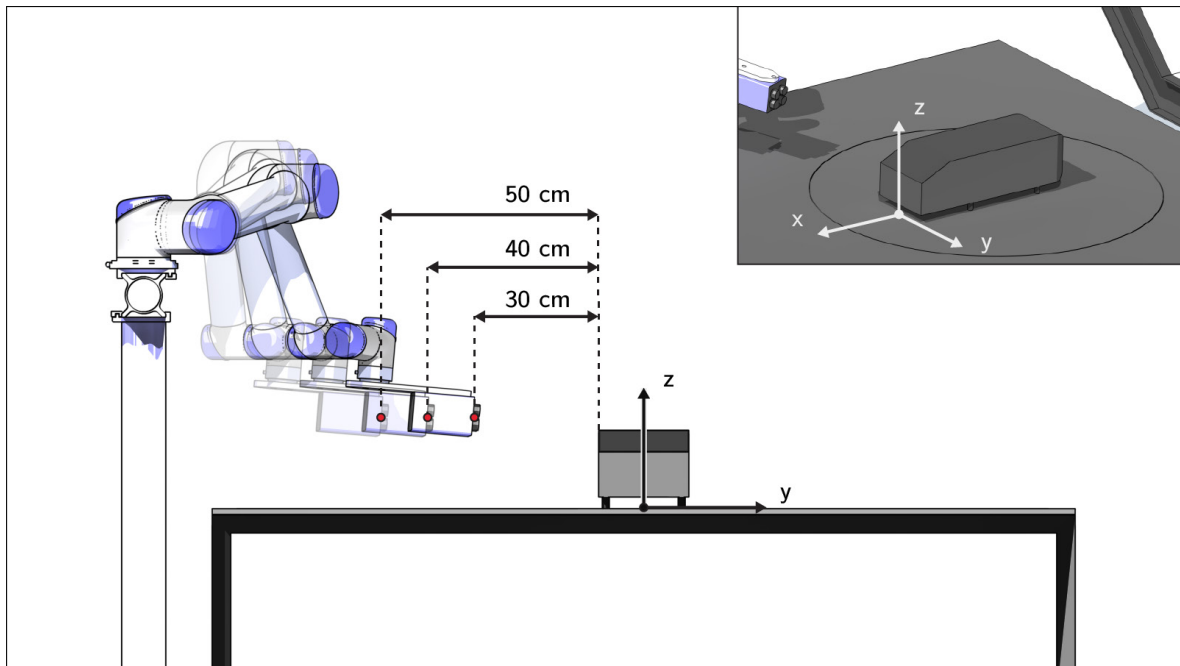
Figure 5.5: Proximity interaction assessment. CVV probe moved in y-direction.

---

[2]Remember STB does not work properly when the particles concentration exceeds 0.05 ppp

Figure 5.6 shows the resulting streamwise velocity field for the three aforementioned camera positions. The left C-pillar vortex has been highlighted by means of a circle (a), in order to ease the comparison between the three runs in terms of size and position. Although the dimension and the location of the vortex do not seem to be affected by the proximity of the camera, the velocity deficit inside the vortex core decreases when the CVV probe is in the closest position, as per figure 5.6 (a). To inspect what looks like a weaker vortex, also the streamwise vorticity has been assessed. In figure 5.7, indeed, the x-vorticity has been plotted for the three cases. From here, again, a visual inspection would suggest a slightly weaker vortex for the first case. However, in order to have a more quantitative idea of the differences, the streamwise vorticity has been integrated on the 50×50 mm square domain (b) highlighted in figure 5.7. The resulting mean vorticity values are $\overline{\omega}_{x,a} = -144.5$ s^{-1}, $\overline{\omega}_{x,b} = -155.9$ s^{-1} and $\overline{\omega}_{x,c} = -150.1$ s^{-1}, for the closer, middle and farther positions, respectively. Although slightly weaker, the integral vorticity over the investigated domain for the first case actually results comparable to the remaining two cases.

Finally, for the sake of correctness, it must be said that the measurement in the closest position has been acquired successively in time, with respect to the other two measurements, to extend the proximity interaction analysis behind any reasonable recording position. This can explain the differences in the top right shape of the cone due to a temporary and local reduction of seeding concentration[3] as well as the asymmetries in the wake between the different cases, possibly index of minor differences in alignment of the rotating disk.

However, with the aim of selecting the optimal probe position for the measurement campaign, only the two farther configurations have been taken into account, mainly because of the impossibility of capturing the whole wake of the test object with the probe in the closest position. In so doing, a distance in y-direction of 42 cm from the left side wall of the Ahmed body has been considered a good compromise, guaranteeing 10 cm of freestream on the right-hand-side of the model, 10 cm on the left-hand-side with a velocity error smaller than 1% (5.1.1) and no intrusiveness effects according to figures 5.6 and 5.7.

---

[3]Such behaviour is typical of the starting stages, after a few minutes of continuous operation the seeding concentration results more homogeneous in space and time.
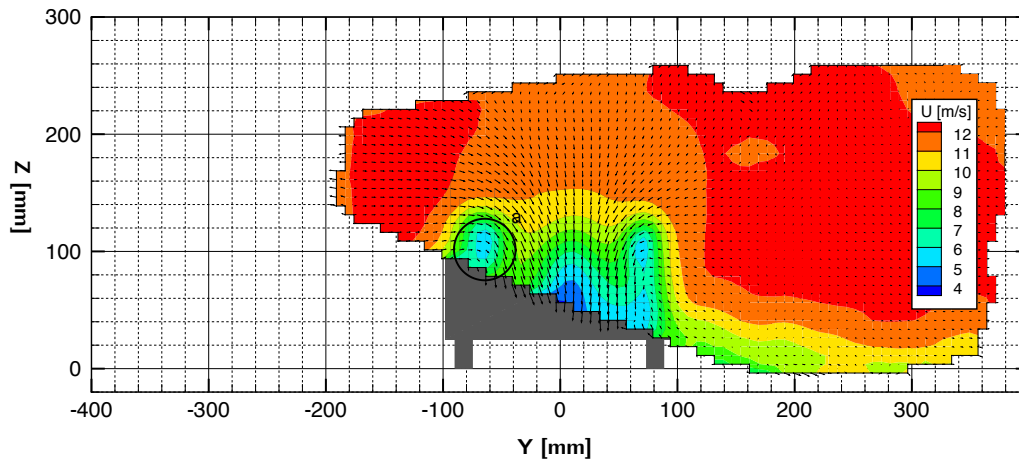
(a) Near position, 30 cm distance.
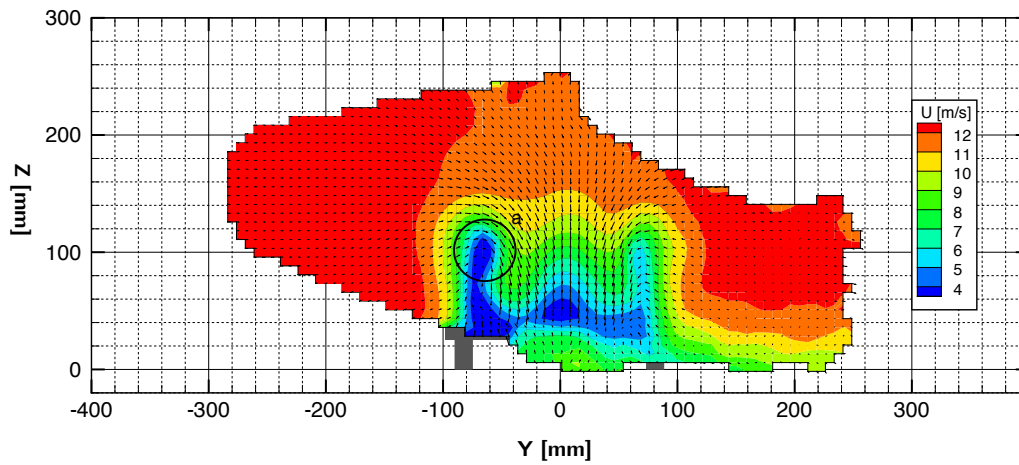
(b) Middle position, 40 cm distance.
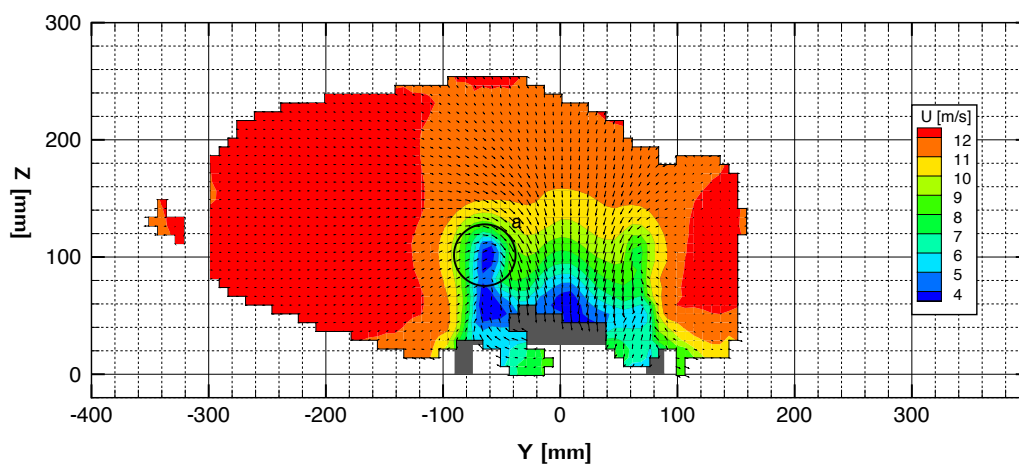
(c) Far position, 50 cm distance.

Figure 5.6: Proximity interaction assessment. streamwise velocity field on an x-plane downstream the Ahmed body (x=100 mm) for the three camera positions of figure 5.5.
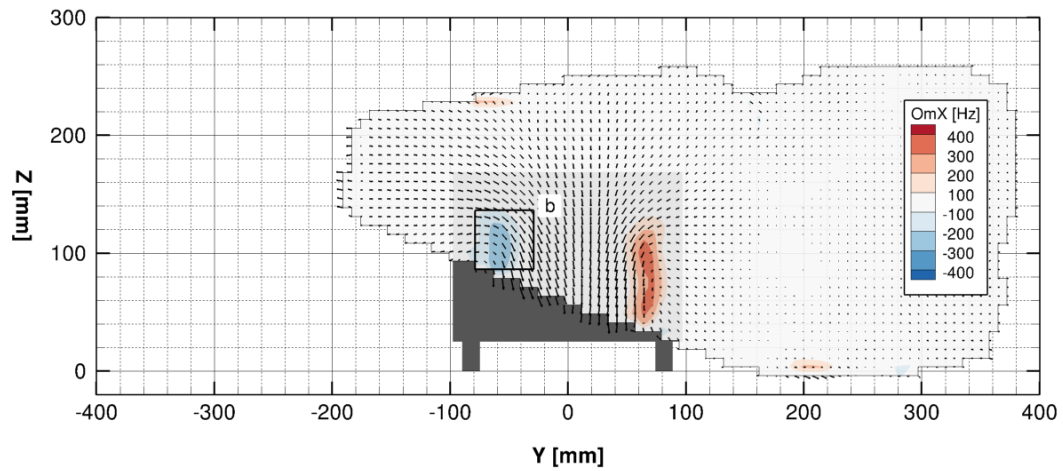
(a) Near position, 30 cm distance.
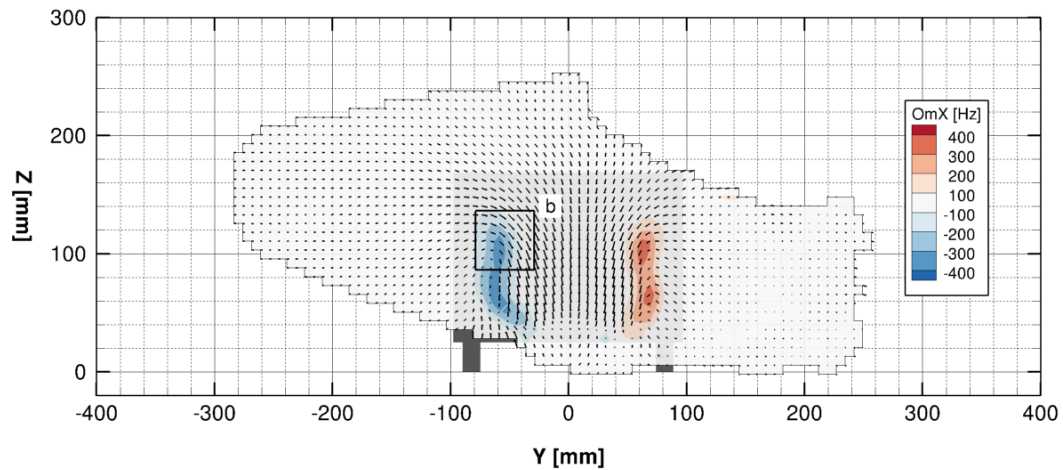
(b) Middle position, 40 cm distance.
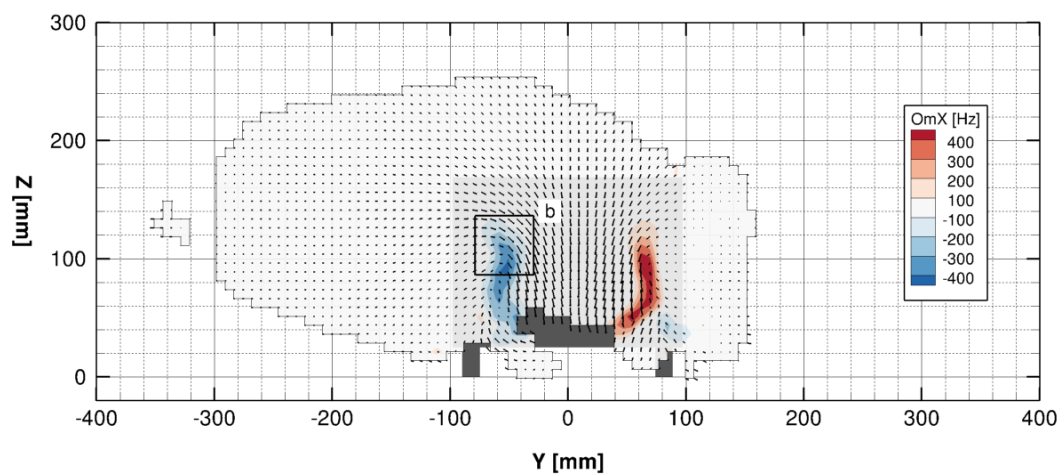
(c) Far position, 50 cm distance.

Figure 5.7: Proximity interaction assessment. streamwise vorticity field on an x-plane downstream the Ahmed body (x=100 mm) for the three camera positions of figure 5.5.

5.2   Bin Size and Statistical Convergence

The convergence of the data has been assessed by evaluating a population of 8,000 frames inside a single measurement cone. A virtual probe has been placed inside the negative C-Pillar vortex, 100 mm downstream the Ahmed body, as illustrated by figure 5.8 (a). The vorticity ω (b), the streamwise velocity U_x (c) and its standard deviation σ_{U_x} (d) have been plotted with increasing the number of randomly selected image frames and with varying the bin size. As expected, with increasing the bin size, and, therefore, the number of particles contained in it, the rate of convergence of the aforementioned variables increases and the oscillations around the mean values are reduced in magnitude and dampen out more rapidly. To facilitate the understanding of such plots and to give the reader a more practical grasp of the effect of changing the size of the binning cell, two-dimensional and three-dimensional representations of the C-Pillar vortices are presented in figure 5.9 and 5.10, respectively.

(a) Probe position, plane x=100 mm.

(b) Vorticity ω.

(c) streamwise velocity U_x.

(d) streamwise velocity standard deviation σ_{U_x}.
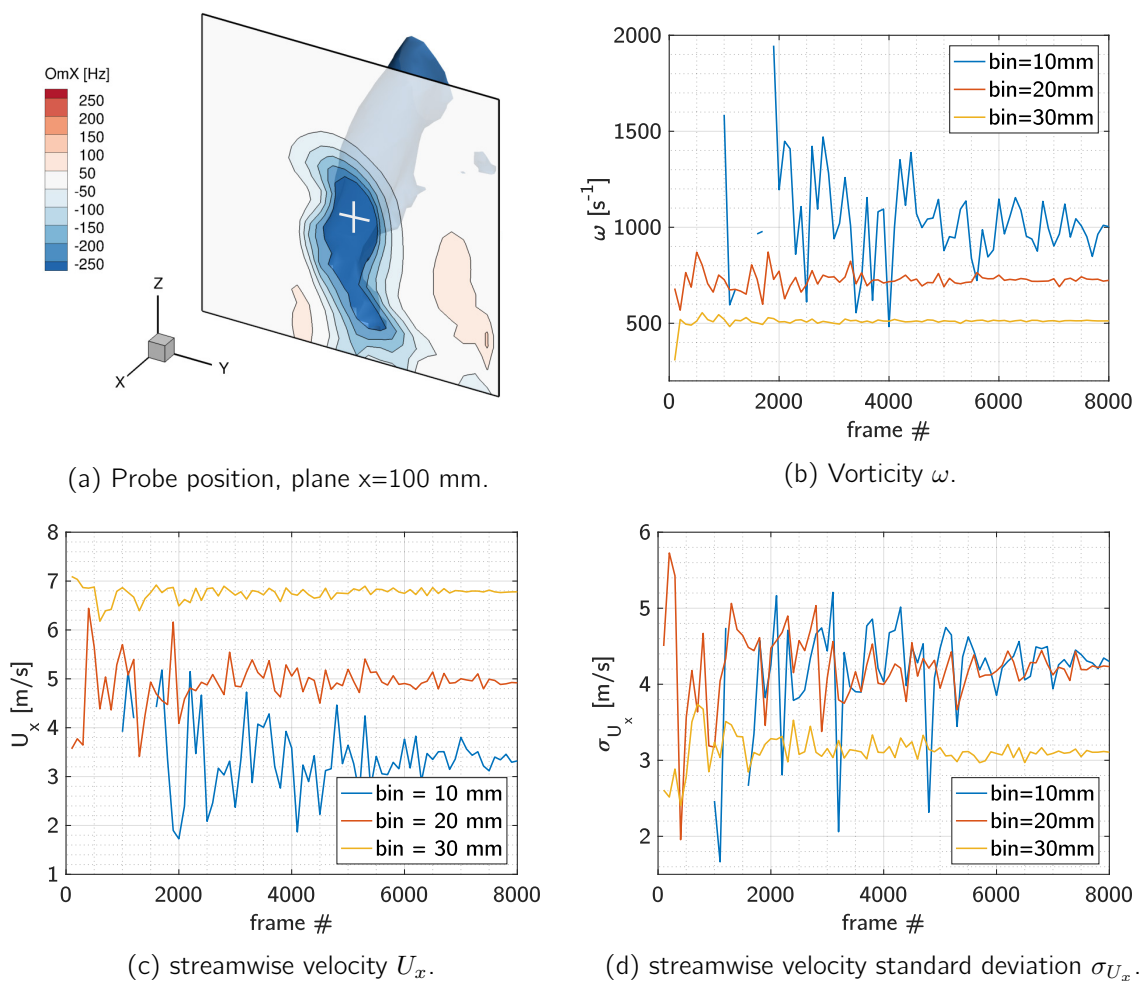
Figure 5.8: Data convergence inside the C-Pillar vortex core (a) with varying bin size and number of acquisition frames.
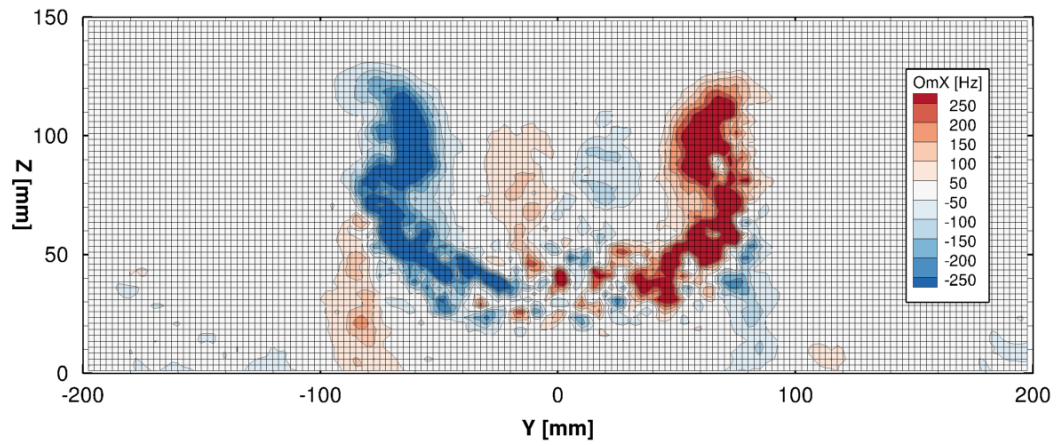
(a) Bin size $10 \times 10 \times 10$ mm.
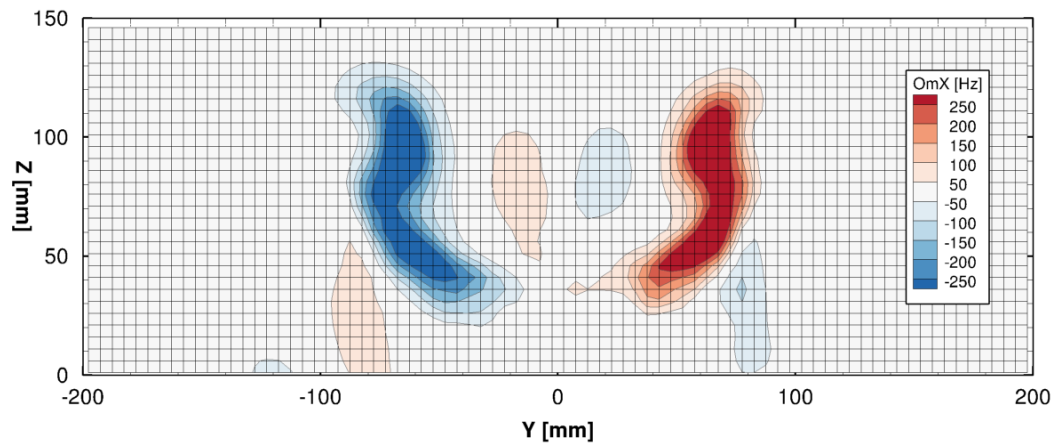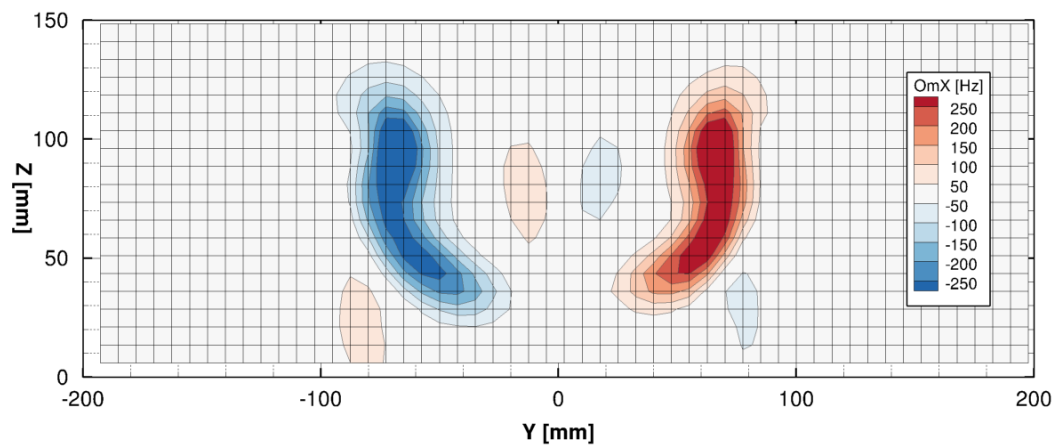
(b) Bin size $20 \times 20 \times 20$ mm.

(c) Bin size $30 \times 30 \times 30$ mm.

Figure 5.9: Bin size assessment. streamwise vorticity field on an x-plane downstream the Ahmed body (x=100 mm) for three different bin sizes.
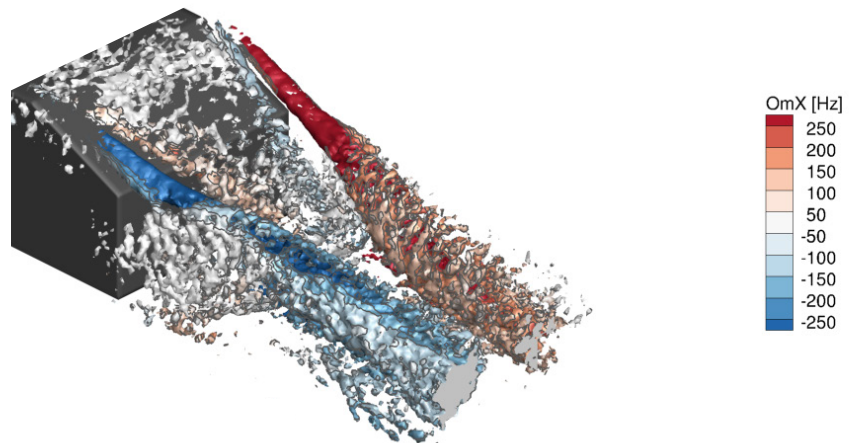
(a) Bin size $10 \times 10 \times 10$ mm.
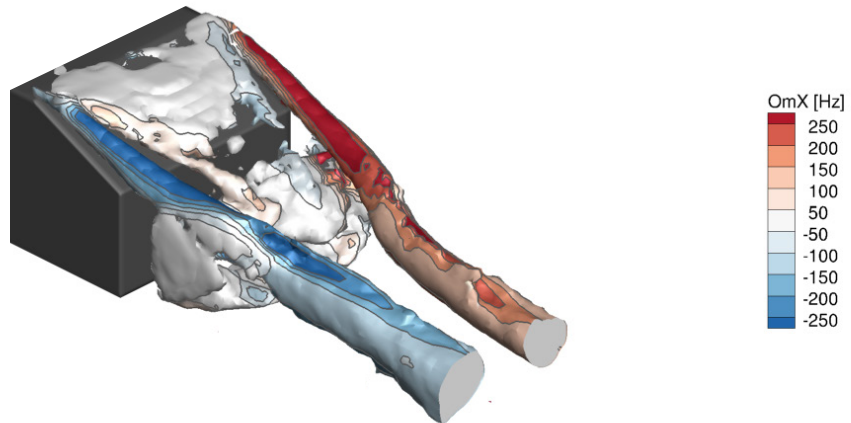
(b) Bin size $20 \times 20 \times 20$ mm.
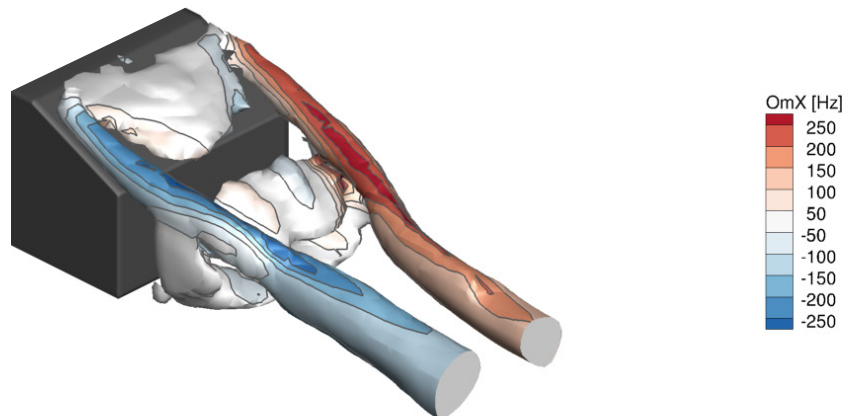
(c) Bin size $30 \times 30 \times 30$ mm.

Figure 5.10: Three-dimensional view of the wake of the Ahmed body for three different bin sizes. Iso-surfaces of Q-criterion at Q=3000 coloured by streamwise vorticity magnitude ω_x [s^{-1}].

In particular, by looking at figures 5.9 (a) and 5.10 (a), it is immediately clear how noisy the data becomes for the smallest bin size, namely 10 mm. This easily explains the highly fluctuating standard deviation of figure 5.8 (d). On the other hand, when increasing the dimension of the bin size, the spatial resolution decreases, as it can be seen from figures 5.9 and 5.10, and some details are lost. Indeed, this results in a spatial modulation of the data, which is clear when looking both at figure 5.8 (b) and (c). The peak of vorticity measured by the probe inside the vortex core decreases with increasing the bin size, since the vorticity results more diffused, and the velocity deficit decreases as well, because of the neighbouring higher velocity entering the boundaries of a bigger bin element.

Because of the aforementioned reasons, a tradeoff aiming at sufficiently statistically con-verged data and moderate spatial modulation is required. By looking at the convergence plots of figure 5.8, a bin size of 20 mm appears a good compromise, resulting sufficiently converged, especially if compared to the smallest bin size, and reducing the data spatial modulation with respect to the bigger one. However, when not interested in quantifying position and intensity of the main vortical structures, a bigger bin size of 30 mm can be useful to highlight smaller and weaker structures which otherwise would disappear because of the noise. Indeed, quantities depending on space-derivatives, such as the vorticity or the Q-criterion, do suffer considerably in the case of noisy data, as the reader can appreciate from figure 5.10 (a).

Finally, although the present convergence analysis is to a certain extent biased by the usage of samples of the same limited population, the random selection of the aforementioned reduces the correlation and the fluctuating resulting behaviour seems representative of a typical statistical convergence. Moreover, because of the overlap of the measurement regions, the number of available frames is expected to increase considerably, which would further improve the statistical convergence.

5.3   System Resolution

The two main parameters commonly used to assess the performance of a PIV system, namely the Dynamic Spatial Range (DSR) and the Dynamic Velocity Range (DVR) have been evaluated for the CVV system and are reported below.

5.3.1   Dynamic Spatial Range

The DSR is defined as the ratio between the largest and the smallest measurable length scales Adrian (1997). For the present application, the largest length scale is represented by the length of the volume measured for the high-cross-wind case while the smallest length scale is represented by the smallest used bin size. The $\overline{\text{DSR}}$ for time-averaged CVV measurements therefore results:

$$\overline{\text{DSR}} = \frac{1100}{20} = 57.$$ (5.5)

The same value can be computed for a single measurement cone, where the largest dimension is represented by the volume depth, of the order of 60 cm. The Dynamic Spatial Range therefore results $\overline{\text{DSR}} \sim 30$.

5.3.2 Dynamic Velocity Range

The DVR, similarly, is derived as the ratio between the maximum measurable velocity and the minimum resolvable one Adrian (1997). For time-averaged measurements, Schneiders (2017) derived an analogous formula, where the smallest resolvable velocity variation depends upon the velocity measurement uncertainty

$$\overline{u}_{min} \approx \sigma_{\overline{u}} \tag{5.6}$$

while the maximum resolvable velocity is dependent upon the maximum particle displacement that can be afforded by the particle tracking algorithm

$$\overline{u}_{max} = \frac{\Delta x_{max}}{\Delta t} \tag{5.7}$$

The $\overline{\text{DVR}}$ for time-averaged CVV measurements can therefore be expressed as

$$\overline{\text{DVR}} = \frac{\Delta x_{max}}{\sigma_{\overline{u}} \Delta t} = \frac{u_{max}}{\sigma_{\overline{u}}} \tag{5.8}$$

For the present experiments, the maximum measured velocity is close to the freestream value and the $\overline{\text{DVR}}$ therefore results

$$\overline{\text{DVR}} = \frac{12}{0.1} = 120. \tag{5.9}$$

In this calculation, the component of the standard deviation in the in-depth direction ($\overline{\sigma}_{u,y}$) has not been taken into account, since affected by the uncertainty due to the CVV low tomographic aperture. With taking into account also this contribution, the minimum value of the standard deviation increases from 0.1 m/s to 0.3 m/s, or, equivalently, from 0.8% to 2.5%. In so doing, the the Dynamic Velocity Range reduces to $\overline{\text{DVR}} \approx 40$

As pointed out by Schneiders (2017), the computed values of dynamic ranges do lie below those typically achieved with both planar and a conventional tomographic PIV measurements. The most common way to increase both $\overline{\text{DSR}}$ and $\overline{\text{DVR}}$ is by collecting larger sequences of images, at detriment of the computation time. Additionally, the $\overline{\text{DVR}}$ can be increased by means of a higher acquisition frequency (i.e. by decreasing the Δt) according to formula 5.8. However, although the acquisition of more samples allows for the use of smaller bins and decreases the random error of the measurement, the upper limit to the $\overline{\text{DVR}}$ is dictated by the intrinsic CVV system error which remains finite and depends upon the instrument precision.

6

Ahmed Body in Cross-wind

In this chapter, the acquired data is presented and commented. The headwind case is firstly validated against the reference literature and the two cross-wind set points are therefore introduced and commented as well. A qualitative and quantitative comparison of the three cases is carried out by inspecting visually the relative flowfields and by comparing position and intensity of the C-pillar vortices with varying the yaw angle β. Finally, based on the present data, a conceptual scheme describing the flow topology for the 25-degrees slant Ahmed body in cross-wind is proposed.

Contents

6.1   Headwind Case

6.1.1   Data Validation

Before analysing the cross-wind cases, the headwind condition has been compared against the data provided by Lienhart & Becker (2003) in order to assess the accuracy of the acquired measurements. At the same time, the boundary layer on the upper surface of the model, before the slant, has been evaluated in order to ensure the zigzag trip successfully managed to trigger transition. As expected, a fully developed boundary layer resulted, whose thickness and shape factor are $\delta_{.95} = 14.7$ mm and $H = 1.25$, respectively[1].

The position and the intensity of the two C-pillar vortices have been evaluated on the three x-planes downstream the model provided by Lienhart & Becker (2003), namely x/H=0.24, x/H=0.59 and x/H=1.48. All the dimensions have been scaled with respect to the height of the model, H, in order to ease the comparison of the present work against the literature. Furthermore, also the vorticity has been nondimensionalized according to

$$\Gamma = \frac{\omega \cdot d}{U} \tag{6.1}$$

being d a characteristic length, in this case the vortex diameter[2], while U, the freestream velocity. The results are graphically illustrated in figures 6.1 to 6.3 and are resumed, in terms of vortices position and intensity, in table 6.1. A very quick analysis of such data shows a good agreement with the reference literature both in terms of vortices position and intensity (peak of streamwise vorticity ω_x and nondimensional streamwise vorticity Γ_x).

(a) Lienhart & Becker (2003).   (b) Present work.
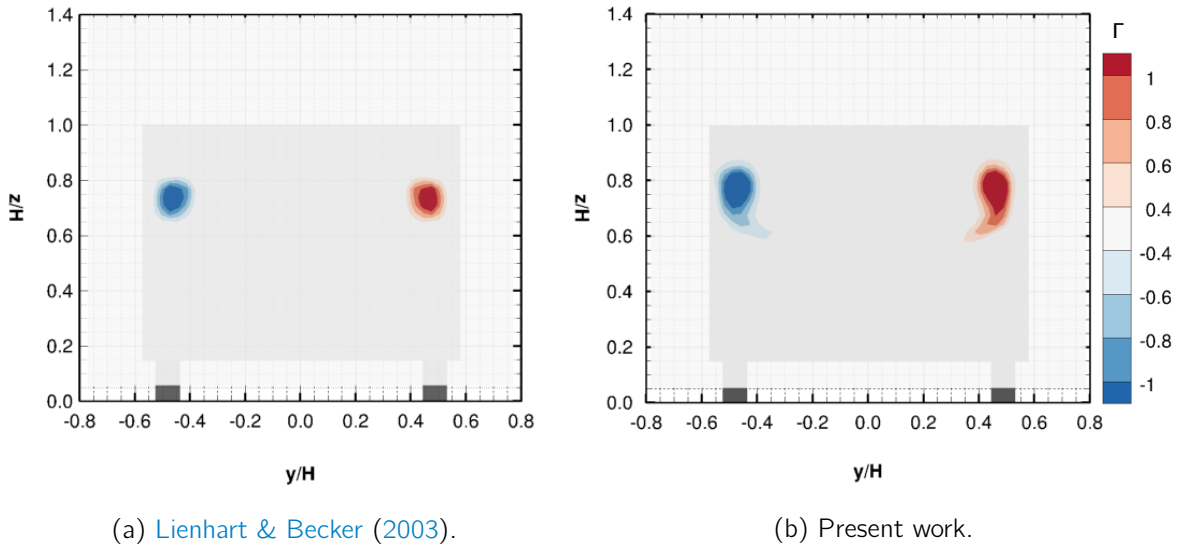
Figure 6.1: Normalized axial vorticity Γ_x downstream the model on plane x/H=0.24, Lienhart & Becker (2003) (a) vs present work (b).

---

[1]See appendix A for further details.

[2]The vortex diameters have been evaluated at x/H=0.24 both for Lienhart and for the present work, resulting in $d_{Lien} = 0.12 \cdot H_{Lien} = 40$ mm and $d_{Pres} = 0.18 \cdot H_{Pres} = 30$ mm, respectively.

Immediately downstream the model, at x/H=0.24, the difference in position falls under 5% with respect to the reference length H, while the streamwise peak vorticity differs for less than 1% (see figure 6.1). Moving further downstream, at x/H=0.59 and x/H=1.48, the positional error never exceeds the 8%, being greater in the vertical direction, and the difference in peak intensity never reaches the 25%. Given the differences in terms of Reynolds number and freestream conditions between the present work and the reference study, such dissimilarities are deemed acceptable and even expected. By looking at figure 6.2 (b), other than moderately elongated,

(a) Lienhart & Becker (2003).   (b) Present work.
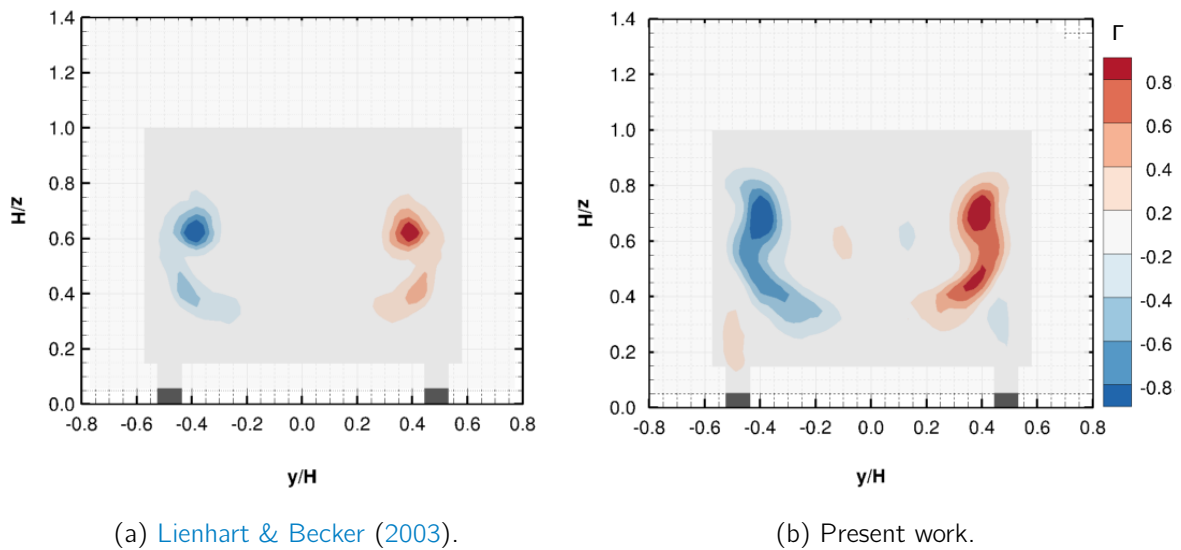
Figure 6.2: Normalized axial vorticity Γ_x downstream the model on plane x/H=0.59, Lienhart & Becker (2003) (a) vs present work (b).

(a) Lienhart & Becker (2003).   (b) Present work.
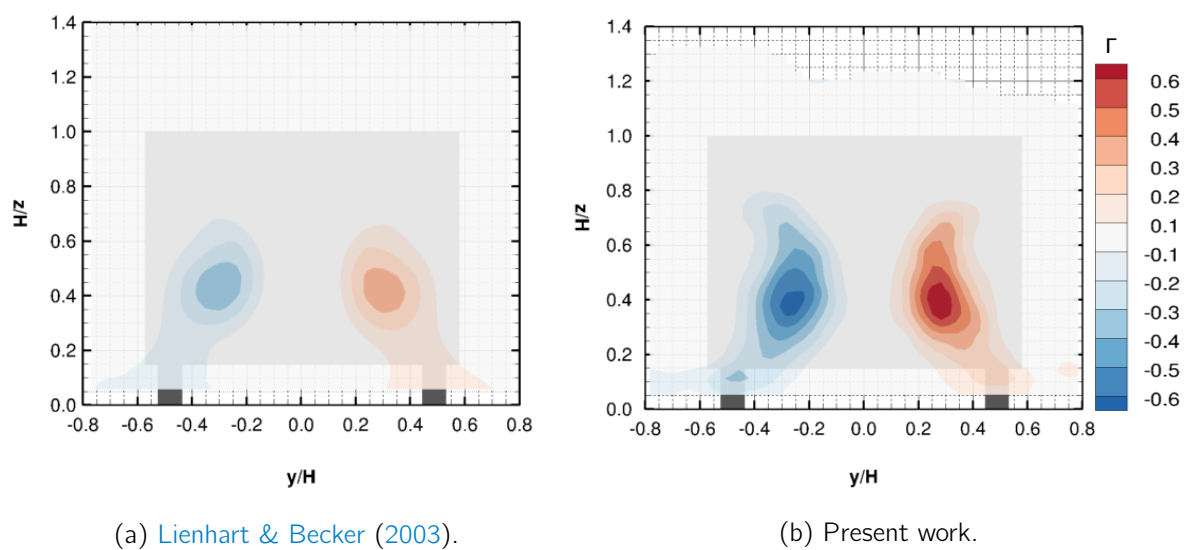
Figure 6.3: Normalized axial vorticity Γ_x downstream the model on plane x/H=1.48, Lienhart & Becker (2003) (a) vs present work (b).

Table 6.1: Vortices position and intensity on x-planes downstream of the model, present work vs Lienhart & Becker (2003).

		Lienhart & Becker		Present work		Comparison	
Position		y/H	z/H	y/H	z/H	Δ_y [%]*	Δ_z [%]*
Plane $x/H = 0.24$	L	-0.464	0.737	-0.473	0.774	-0.9	+3.7
	R	0.463	0.736	0.462	0.780	-0.1	+4.4
Plane $x/H = 0.59$	L	-0.391	0.626	-0.398	0.692	-0.7	+6.6
	R	0.389	0.625	0.391	0.702	+0.2	+7.7
Plane $x/H = 1.48$	L	-0.304	0.435	-0.266	0.377	+3.8	-5.8
	R	0.306	0.423	0.282	0.375	-2.4	-4.8
Intensity		ω_x [1/s]	Γ [-]	ω_x [1/s]	Γ_x [-]	Δ_{Γ_x} [%]	
Plane $x/H = 0.24$	L	-1755	-2.04	-785	-1.99	-2.5	
	R	1696	1.97	765	1.94	-1.5	
Plane $x/H = 0.59$	L	-1419	-1.65	-513	-1.30	-21.2	
	R	1285	1.50	447	1.13	-24.7	
Plane $x/H = 1.48$	L	-512	-0.60	-259	-0.66	+10.0	
	R	491	0.57	271	0.69	+21.1	

the cores vortices do result slightly higher if compared to the reference case (a). This can be due to the lower Reynolds number resulting in a somehow reduced downwash of the curving downward flow above and past the slanted surface. Furthermore, from figure 6.3, the vorticity content of the vortices for the present work (b) looks higher than for the reference case (a). Again, this can be due to the higher Reynolds number and the resulting higher turbulence which increases the diffusion and the dissipation of the cores vorticity for the reference case (a).

To proceed with the present analysis, also the information on the symmetry plane have been exploited to assess the flow topology. As figure 6.4 illustrates, the obtained flowfield (b) shows

Table 6.2: Critical points position on the symmetry plane, present work vs Lienhart & Becker (2003).

		Lienhart & Becker		Present work		Comparison	
		x/H	z/H	x/H	z/H	Δ_x [%]*	Δ_z [%]*
Upper Focus Point	F_1	0.166	0.400	0.253	0.479	+8.7	+7.9
Lower Focus Point	F_2	0.297	0.195	0.466	0.215	+16.9	+2.0
Saddle Point	S	0.532	0.255	0.596	0.237	+6.4	-1.8

* The Δ is computed with respect to the reference length H.

all the expected characteristics, in agreement with the reference case (a). The recirculation behind the base of the model consists of two counter-rotating vortices, staggered in x and y-direction, and the streamlines coming from the top and the bottom of the model do converge towards a saddle point to then maintain a downward velocity component. Most importantly, as highlighted by the slant area detail of figure 6.5, the slant recirculation bubble reattaches towards the end of the slant surface. This proofs that, despite the lower Reynolds number, the
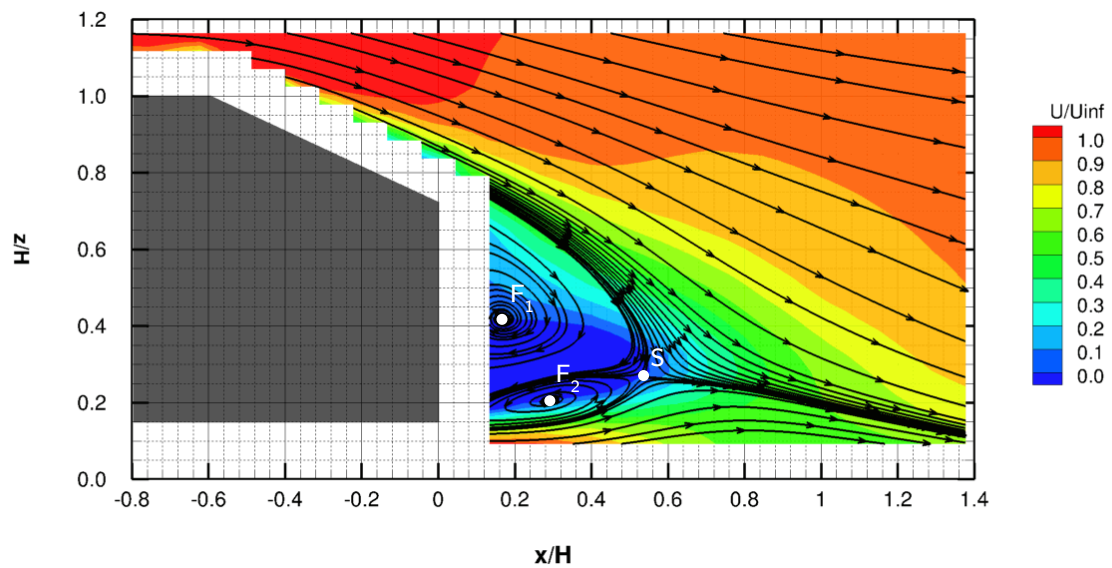
(a) Lienhart & Becker (2003).
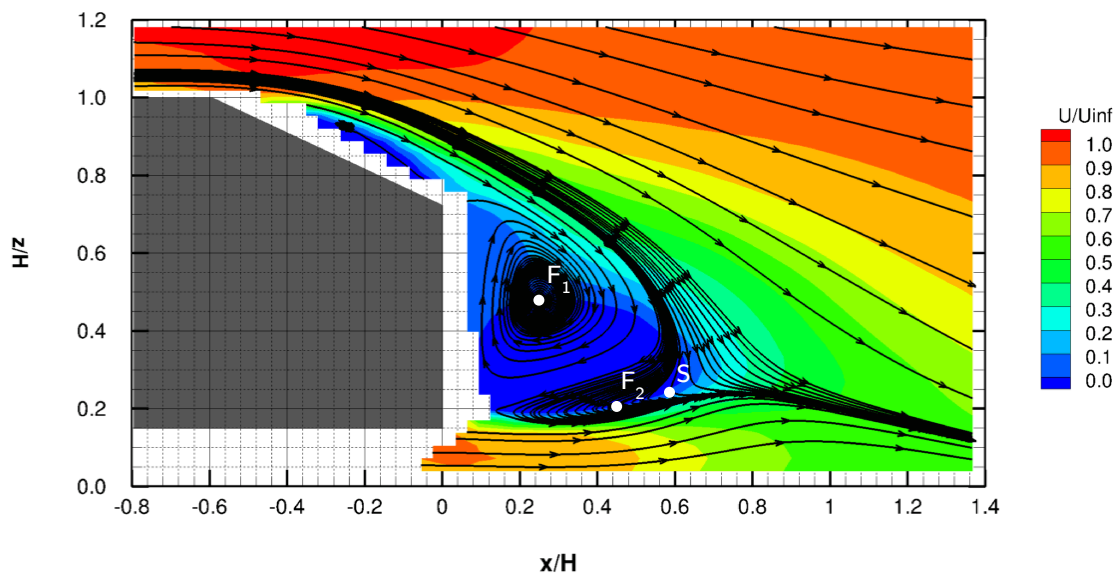
(b) Present work.

Figure 6.4: Nondimensional streamwise velocity U/U_∞ and streamlines on the symmetry plane y/H=0, Lienhart & Becker (2003) (a) vs present work (b).
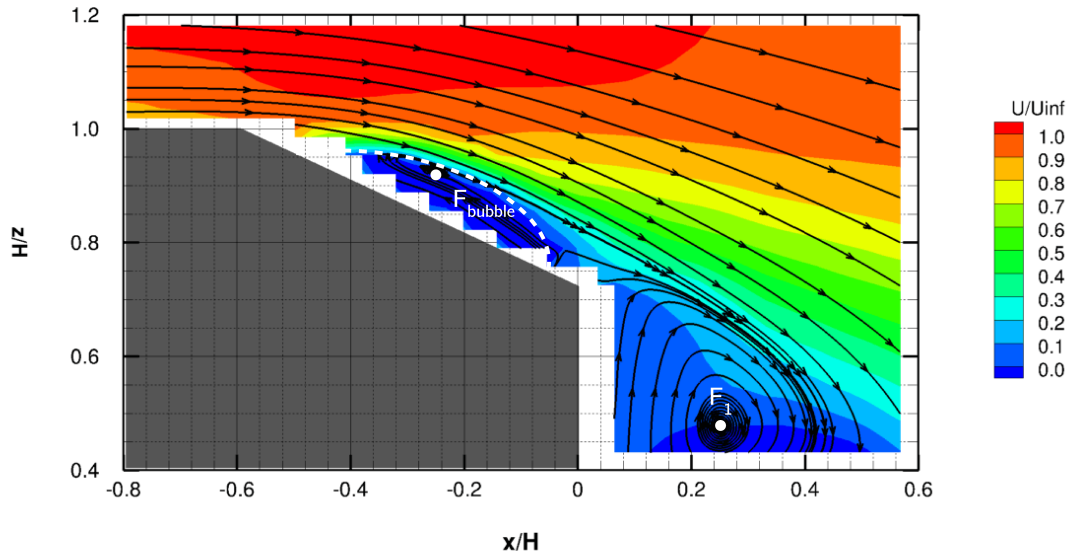
Figure 6.5: Axial vorticity ω_x downstream the model on plane x/H=1.48.

obtained flow topologies is in good agreement with what expected for a 25 degrees slant model. Some minor differences, such as the position of the critical points, namely the focii F_1 and F_2 and the saddle point S, are quantified in table 6.2. Finally, the moderate differences in the shape of the streamlines and in the wake velocity deficit do look compatible with the lower Reynolds number which characterizes the present work.

6.1.2   Three-dimensional Flowfield

Among the tools to visualize three-dimensional vortical structures, iso-surfaces of Q-criterion[3] coloured by streamwise vorticity magnitude has been employed in figure 6.6. The two main counter-rotating vortical structures, namely the C-pillar vortices, are immediately discernable. As expected, they originate from the slant side-edge as result of the pressure differential between the model side walls and the low-pressure slant surface. The flow coming from the roof of the model separates because of the slope discontinuity but it eventually reattaches, supported by the downwash generated by the two C-pillar vortices. This results in the so-called slant separation bubble, feature which characterizes the 25-degrees slant configuration. The flow coming from the side walls of the model rolls up into two vertical vortices, generated by the pressure and velocity differential between the freestream and the wake of the model. In the same way, the flow coming from the slant and from the bottom surface of the model does roll up into two horizontal vortices, already highlighted in figure 6.4. This double pair of counter-rotating vortices, the former with a prevalent content of ω_z vorticity while the latter dominated by ω_y, generates a toroidal vortex system constituting the wake recirculation. Although figure 6.6 shows some vorticity close to the side edges of the slant separation bubble, which is opposed to the one of the close C-pillar vortices, the selected Q level does not emphasize any coherent

---

[3]Refer to appendix B for definition and limitations.

structure. To address such issue, iso-surfaces of streamwise vorticity $\omega_x = \pm 70$ s^{-1} have been plotted in figure 6.7, which clearly shows two weaker and counter-rotating structures between the two main C-pillar vortices. Such secondary vortices, induced by the main vortices, are then advected downstream and downwashed by the C-pillar vortices. As for the C-pillar vortices, they move downwards under the effect of both their own downwash and the low pressure inside the wake recirculation. At the same time, the low pressure of the cores, draws them towards each other, prevailing on their image effect with the close ground which would otherwise move them apart from the symmetry plane.
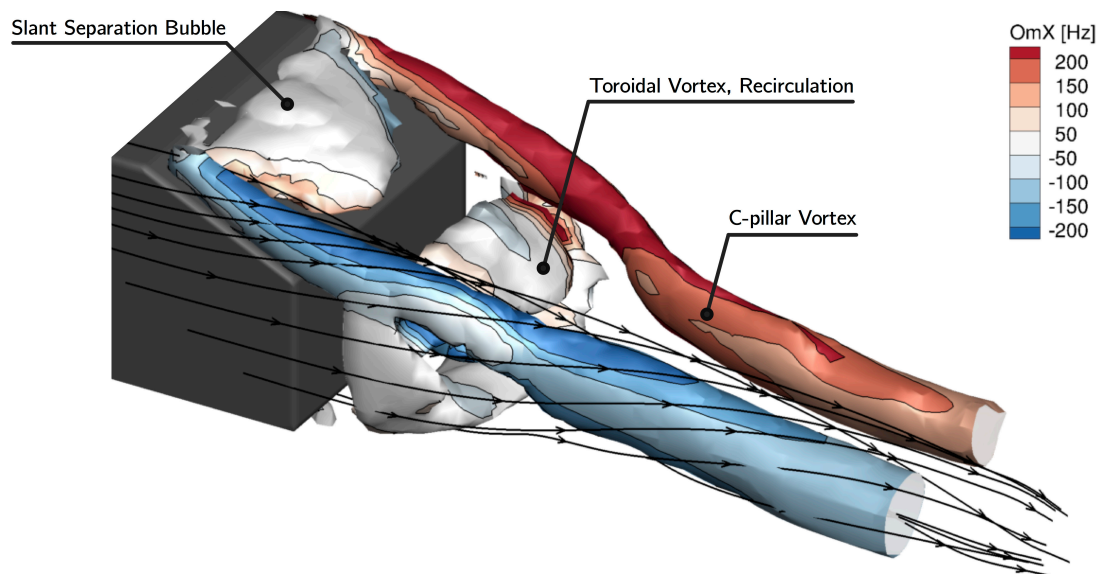
Figure 6.6: Iso-surfaces of Q=4000 s^{-2} coloured by streamwise vorticity ω_x. $\beta = 0°$.
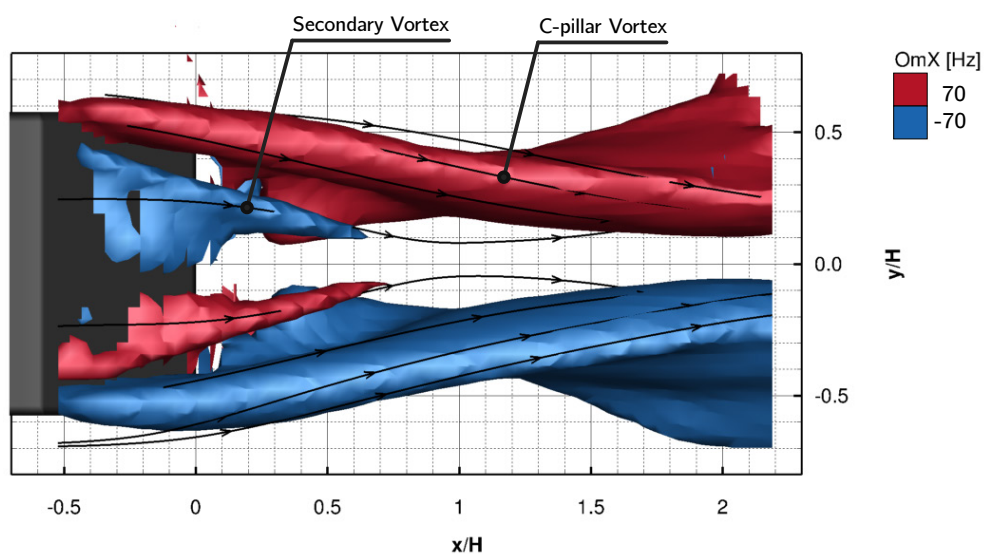
Figure 6.7: Iso-surfaces of streamwise vorticity $\omega_x = \pm 70$ s^{-1}. $\beta = 0°$.

6.2   +4° Yaw Case

Before introducing the results in presence of a yaw angle β, the setup for the cross-wind cases is illustrated in figure 6.8. As inferable from the drawing, in order to produce a cross-wind velocity component, the rotating disk the Ahmed body is connected to has been tilted in counterclockwise direction. This results in a positive yaw angle β and in a cross-wind velocity component from the right.
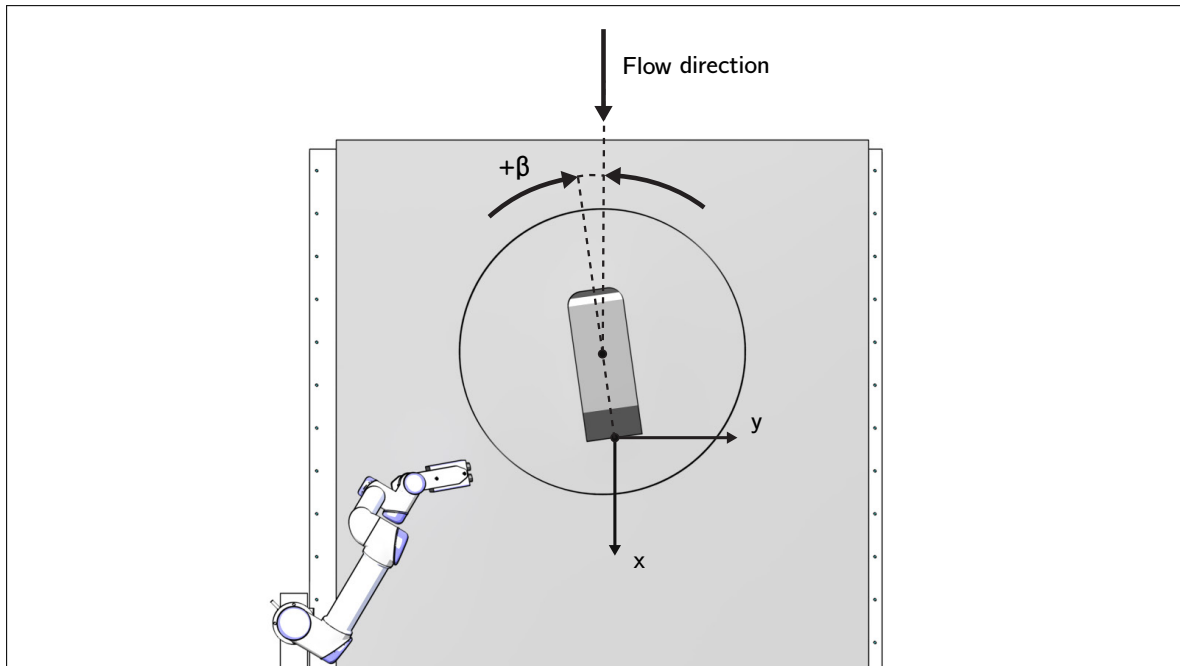
Figure 6.8: Reference system for cross-wind cases. A positive sideslip angle β generates a cross-wind component from the right of the model.

6.2.1   Three-dimensional Flowfield

The introduction of a yaw angle clearly generates some asymmetries in the flowfield around and downstream the model. In particular, the static pressure on the two side walls is not homogeneous anymore. The right, windward wall, can be thought as a pressure side, while the left one, is expected to manifest a drop in static pressure. This pressure differential, close to the slant side-edge, affects the way the C-pillar vortices roll-up. The windward C-pillar vortex, indeed, is strengthened by an increased static pressure on the windward side wall, which produces a stronger pressure differential between the side wall itself and the slant surface. On the other hand, the drop in pressure on the leeward side wall decreases the pressure differential with the slant and therefore weakens the leeward C-pillar vortex. What just described can be verified by looking at figure 6.9 (a). In here, indeed, despite the small yaw angle, not only the right C-pillar shows a greater diameter with respect to the leeward one, but its increased strength, and therefore downwash, partially suppresses the slant separation bubble which now loses its symmetry. The increase in downwash generated by the now stronger right C-pillar vortex can be

appreciated in figure 6.9 (b) as well, where the two vortices appear clearly staggered in vertical direction and the weaker one (leeward side) results downwashed by the stronger one (windward side). Apart from this vertical displacement, also an asymmetry in the y-direction is present, being the leeward blue vortex drawn slightly inboard. No relevant differences are appreciable with respect to the toroidal vortex system inside the recirculation bubble downstream the base surface. By looking at weaker structures, iso-surfaces of streamwise vorticity do highlight some other interesting differences with respect to the headwind case. Figure 6.10, indeed, shows
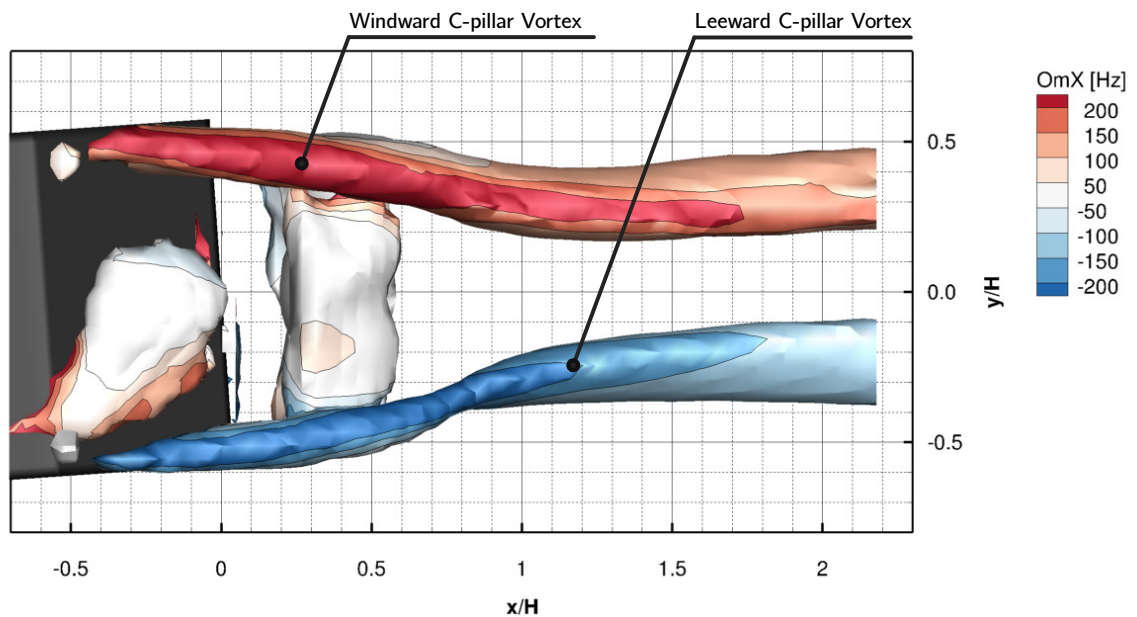
(a) Top view.
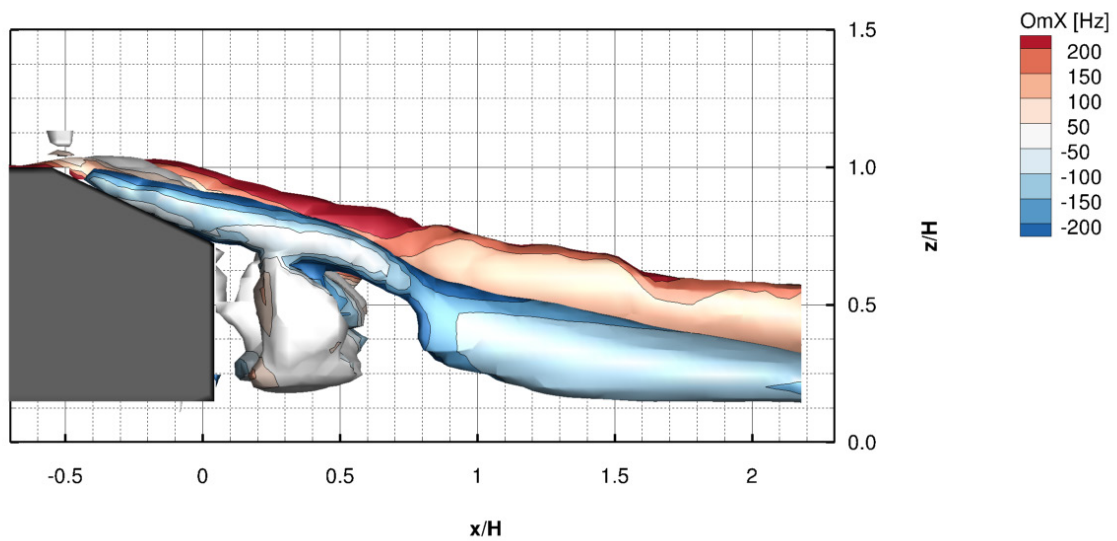
(b) Side view.

Figure 6.9: Iso-surfaces of Q=4000 s^{-2} coloured by streamwise vorticity ω_x. $\beta = +4°$.

that the windward secondary vortex has been almost entirely suppressed while the leeward one has gained some strength. More interestingly, two new vortices appear, namely a roof vortex, generated by the pressure differential between the roof and the leeward (suction) surface, and a counter-rotating ground vortex, originated upstream, again by the pressure differential between the lower and the leeward surfaces. The present brief and qualitative analysis of the flowfield topology is further extended with quantitative data in section 6.4, where the low and high cross-wind cases are compared against each other and, together, against the headwind case.
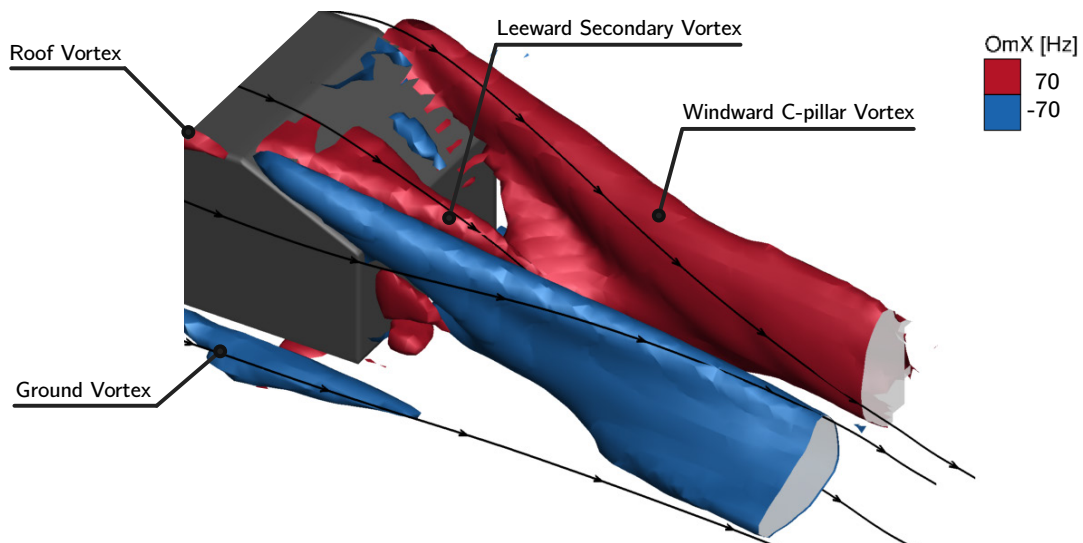
Figure 6.10: Iso-surfaces of streamwise vorticity $\omega_x = \pm70 \ s^{-1}$. $\beta = +4°$.

6.3 $+8°$ Yaw Case

6.3.1   Three-dimensional Flowfield

At the high-yaw set point, some of the new characteristics highlighted for the low-cross-wind case are present again and, as expected, they even result strengthened. On the other hand, new features appear which once again do modify the flow topology. As seen for moderate yaw angles, due to the asymmetry of the flow field, new structures such as ground and roof vortices now reach the rear end of the model. It, therefore, results of interest to track them back to their origin in order get a complete snapshot of the flow around the test object. For this purpose, the standard sweep used for the two previous measurements has been extended upstream and a larger volume has been investigated. The outcome is presented in figure 6.11.

Starting from the front of the model, a limited recirculation area is present on the leeward side wall, straight after the curved leading edge. Evidence of such kind of separation can be found for the headwind case in the literature, mostly in computational studies (Krajnovic & Davidson, 2005; Minguez et al., 2008), although few experimental investigations are reported as well (Zhang et al., 2015). Moving downstream, three new vortices appear close to the longitudinal edges of the body which are related to the yaw condition.
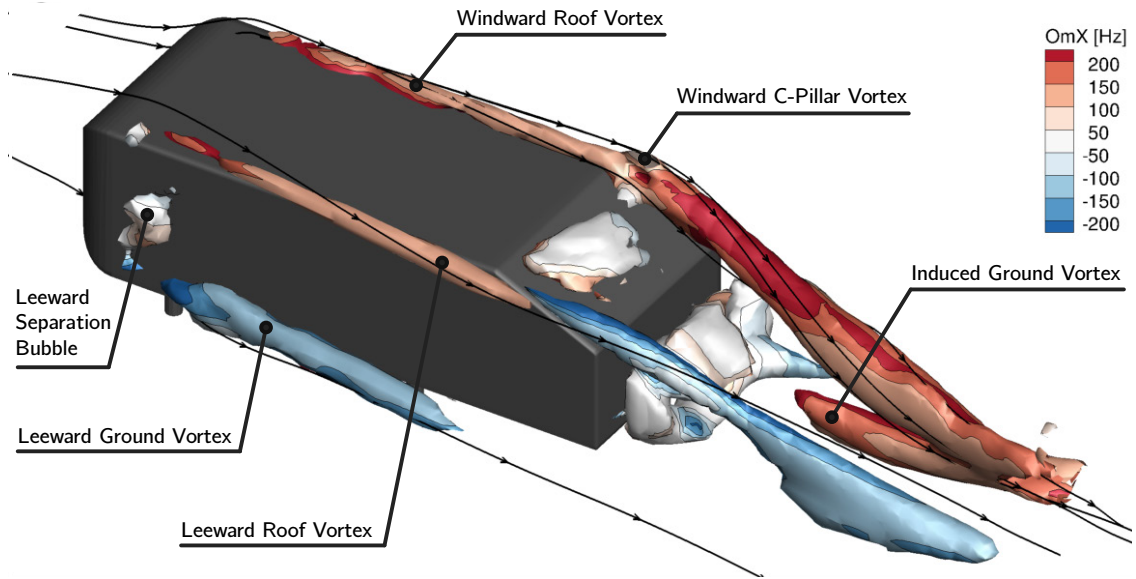
(a) 3D view.
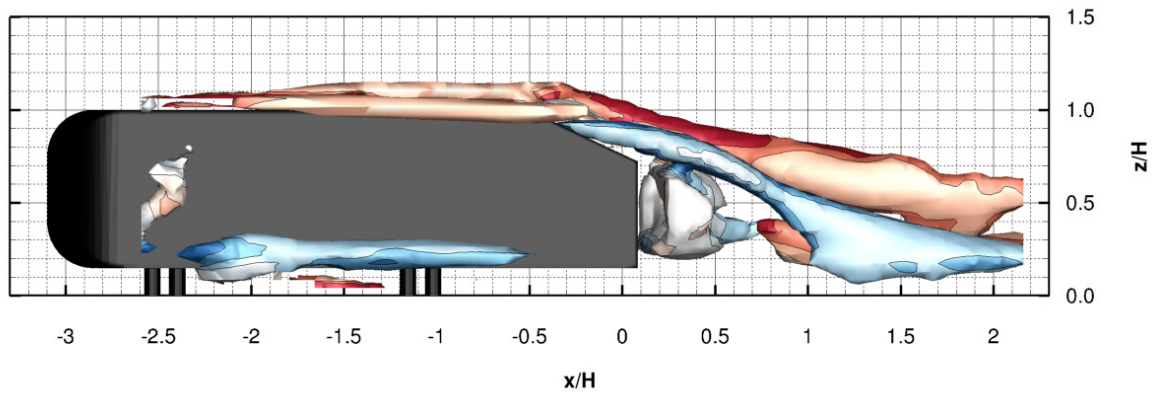
(b) Side view.
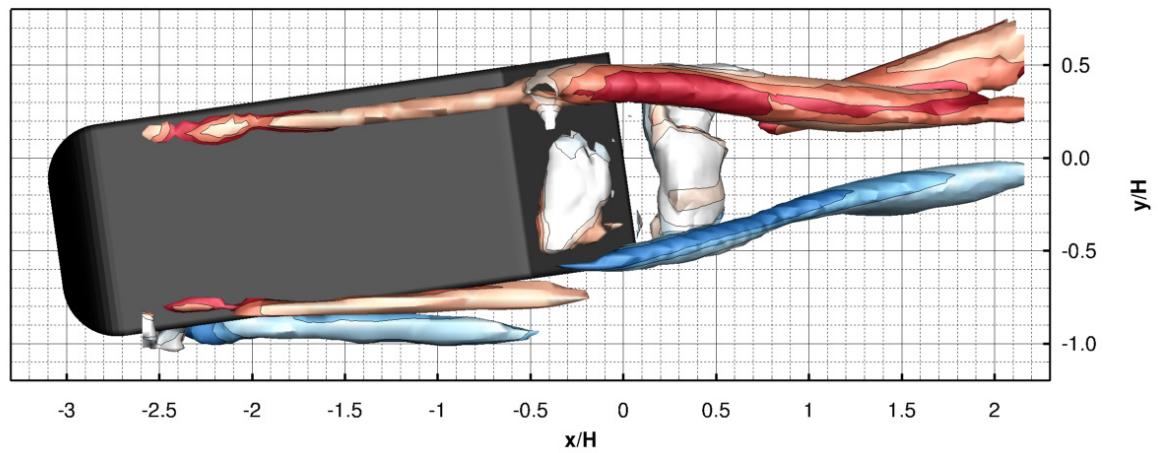
(c) Top view.

Figure 6.11: Iso-surfaces of Q=4000 s^{-2} coloured by streamwise vorticity ω_x. $\beta = +8°$.

On the upper side of the model, the high pressure on the right, windward wall moves the air towards the roof and because of the presence of the sharp top side edge, this results into a positive vortex rolling up and moderately gaining strength while been convected downstream. The same occurs because of the pressure differential between the roof and the left side wall. The leeward side, in fact, as said before is expected to show a drop in static pressure which draws flow towards its boundaries. As a positive vortex rolls up from the top edge of the leeward side surface, an opposite one generates from the lower edge, fed by the higher pressure coming from underneath the model and driven by the low pressure on the suction, leeward side. Both the aforementioned two roof vortices and the last leeward ground vortex can be appreciated in figure 6.11 (a). By looking at the slant area, in agreement with what found for the lower yaw angle case, the C-pillar on the windward side grows in strength once more while the weakened C-pillar on the leeward side is downwashed and drawn inboard once more, as figures 6.11 (b) and (c) show, respectively. As for the slant separation bubble results once again partially suppressed in the proximity of the windward C-pillar where a stronger downwash promotes reattachment. More interestingly, in the wake of the model, a new strong vortex appears. As highlighted by 6.11 (a), indeed, a positive vortex originates in close proximity with the ground, downstream the model, which strongly interacts with the windward C-pillar vortex, being by it considerably swept outboard. The generation of such new ground vortex has been further investigated and a detail of the interested region is illustrated in figure 6.12. By decreasing the Q-criterion value for the iso-surfaces, indeed, the new ground vortex appears to have a bifurcated head. A lower branch draws flow from a ground boundary layer separation, induced by the low pressure and upward movement impressed to the flow by the lower spanwise filament of the toroidal wake vortex. On the other hand, an upper branch is fed by the flow coming from the roof of the model and passing over the slant, under the downwash of the windward C-pillar vortex. When the two aforementioned flows merge, just downstream the wake recirculation bubble saddle point, the
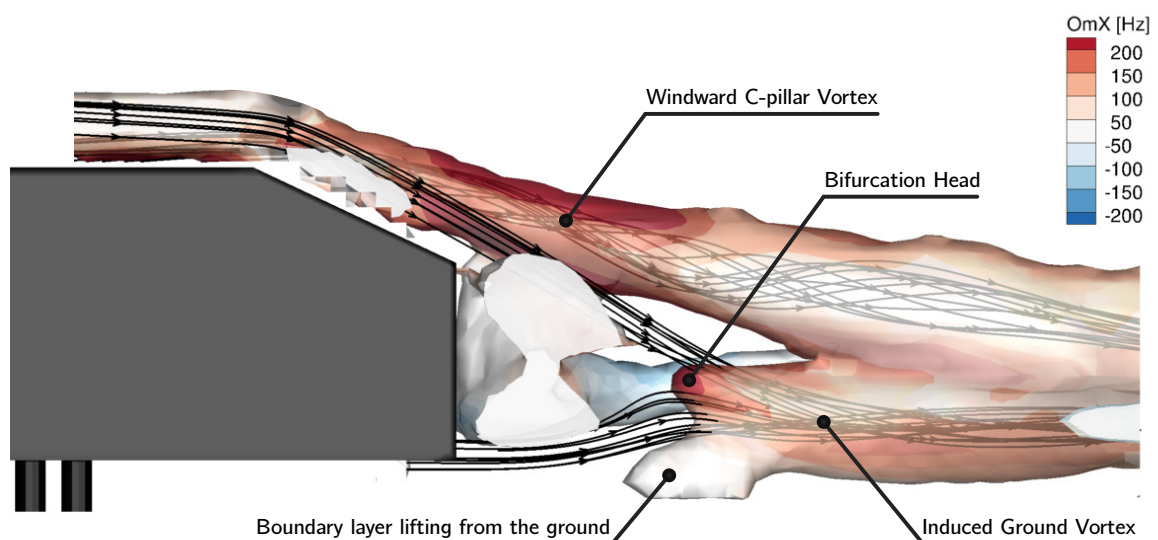
Figure 6.12: Iso-surfaces of Q=2000 s^{-2}. Windward vortical structures at $y/H \geq 0$. $\beta = +8°$.

proximity with the strong C-pillar vortex induces some positive rotation and outwashes the just formed ground vortex.

As with the moderate cross-wind case, this brief analysis further extended and supported with quantitative data in section .

6.4   Cases Comparison

Before digging into a more quantitative analysis of the different flowfields obtained with varying the cross-wind angle β, for the sake of interest, some information about the three investigated cases are reported in table. For the three different cases, among the other things, the total number of measurements is indicated, ranging from a minimum of 8 measurements volumes for the low-cross-wind case to a maximum of 15 measurements cones for the high-cross-wind case, where the investigation has been extended upstream the slant area. For such case, the total investigated volume resulted in approximately 130 litres, which required less than 6 hours of CPU time on the acquisition computer to move from the acquired raw data to the presented one. As it is immediately clear when comparing the used CVV technique to conventional tomographic PIV, not only the investigated volume results conspicuously larger, but also the time required for processing the data makes the present technique particularly interesting.

Table 6.3: General information about the three study cases.

	Bin Size [mm^3]	# of CVV Measurements	Measured Volume [l]	# of Particles	# of Particles per Bin	Processing Time [h]
$\beta = 0°$	30^3	9	81.1	3.05×10^9	1.59×10^4	3.3
	20^3	-	-	-	0.47×10^4	3.4
$\beta = +4°$	30^3	8	80.8	2.45×10^9	1.28×10^4	2.9
	20^3	-	-	-	0.38×10^4	3.0
$\beta = +8°$	30^3	15	130.7	4.59×10^9	1.48×10^4	5.4
	20^3	-	-	-	0.44×10^4	5.6

6.4.1   Flowfields Comparison

The qualitative effects on the near-wake vortical structures produced by the introduction of a cross-wind angle β different from zero are clearly appreciable from a simple visual inspection. To ease this task, the three studied configurations and the relative flowfields have been juxtaposed in figure 6.13 and 6.14. By looking at figure 6.13, a clear trend can be inferred with regards the strength and the vertical position of the two C-pillar vortices with varying the cross-wind angle. With increasing β, indeed, not only the windward vortex (red) increases its size and moves upward, but at the same time, the leeward vortex (blue) weakens and, while stretching, moves downward, under the effect of an increased downwash produced by the now stronger windward C-pillar vortex.
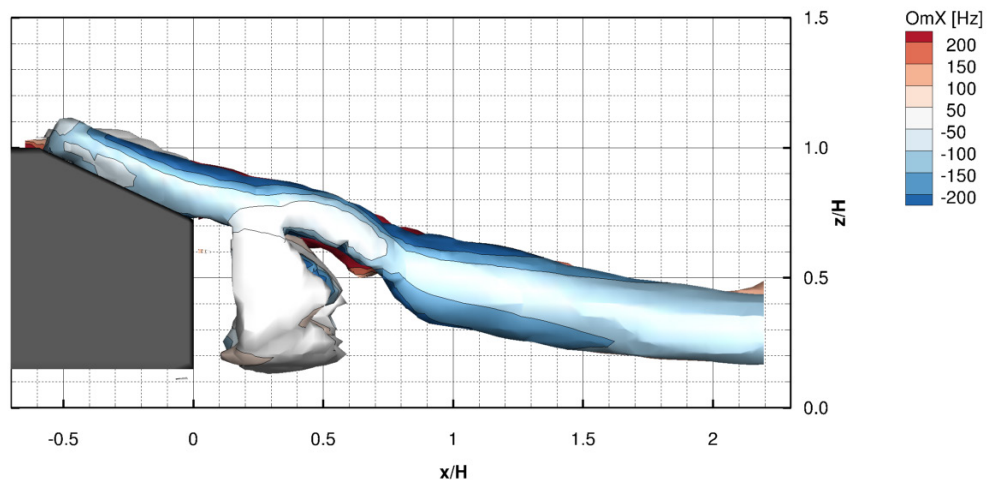
(a) $\beta = 0°$.
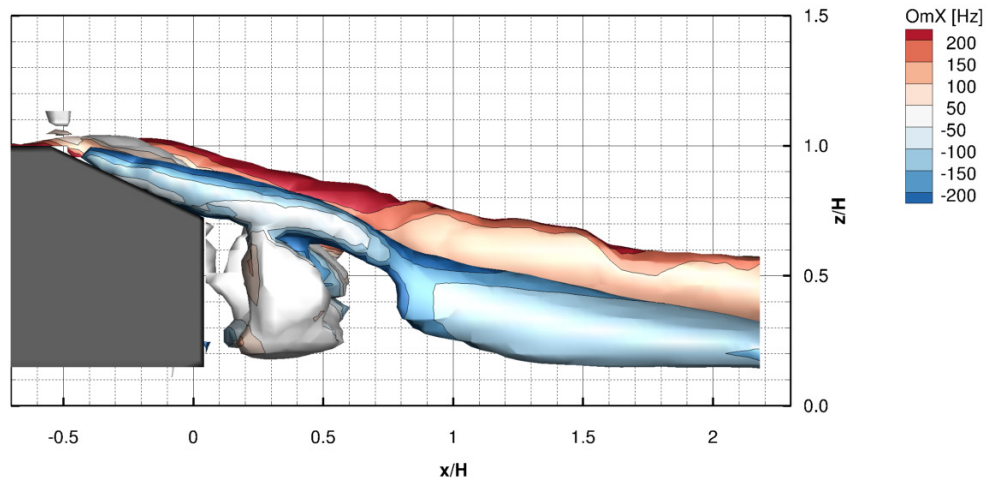
(b) $\beta = +4°$.
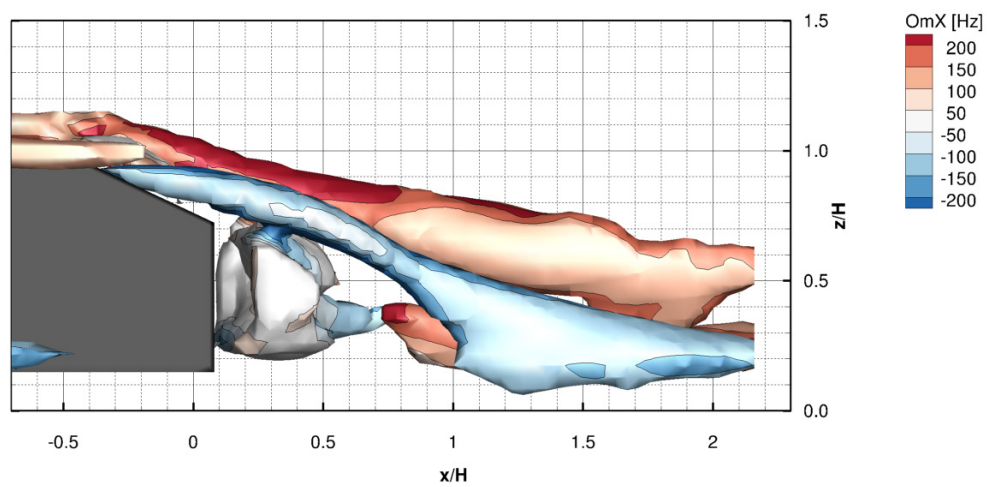
(c) $\beta = +8°$.

Figure 6.13: Iso-surfaces of Q=4000 s^{-2} coloured by streamwise vorticity ω_x vs β. Side view.

(a) $\beta = 0°$.

(b) $\beta = +4°$.

(c) $\beta = +8°$.
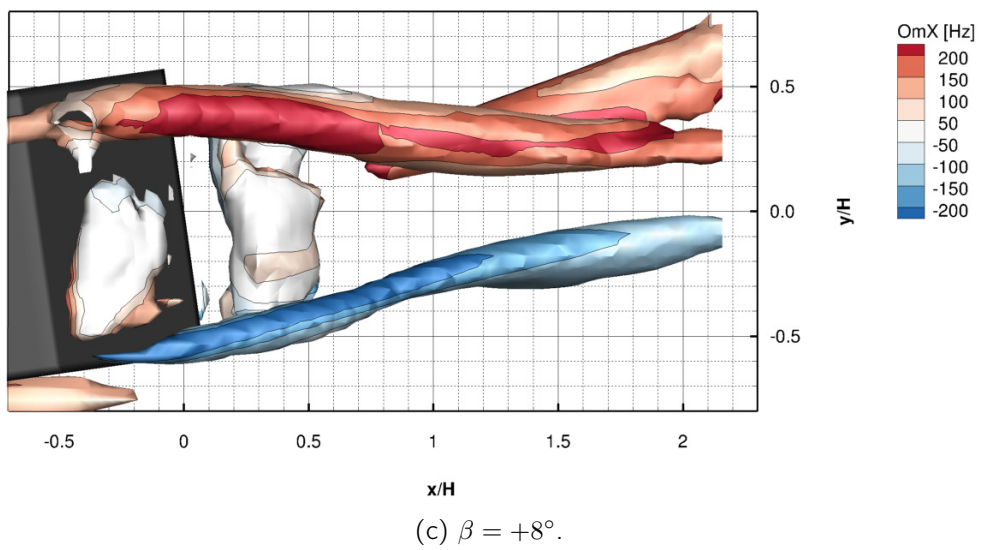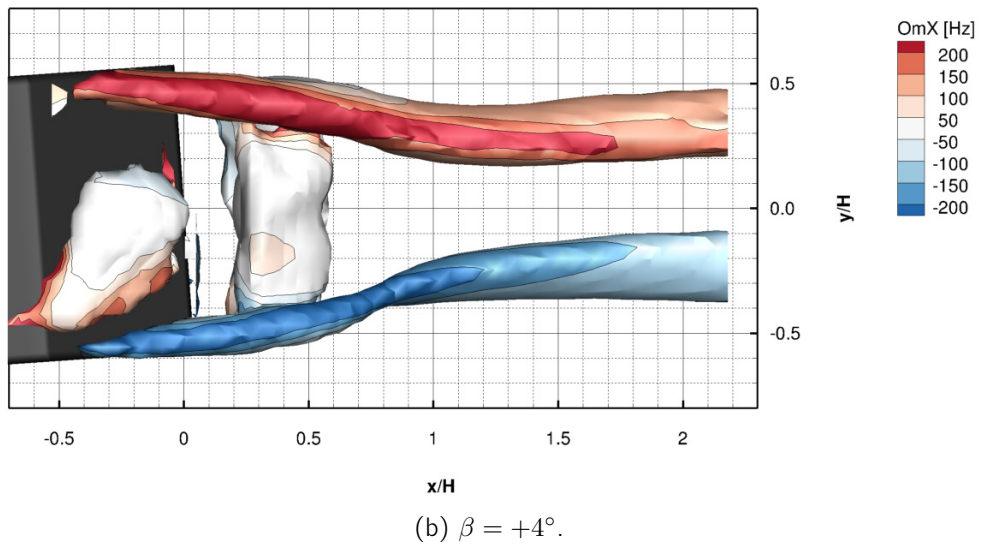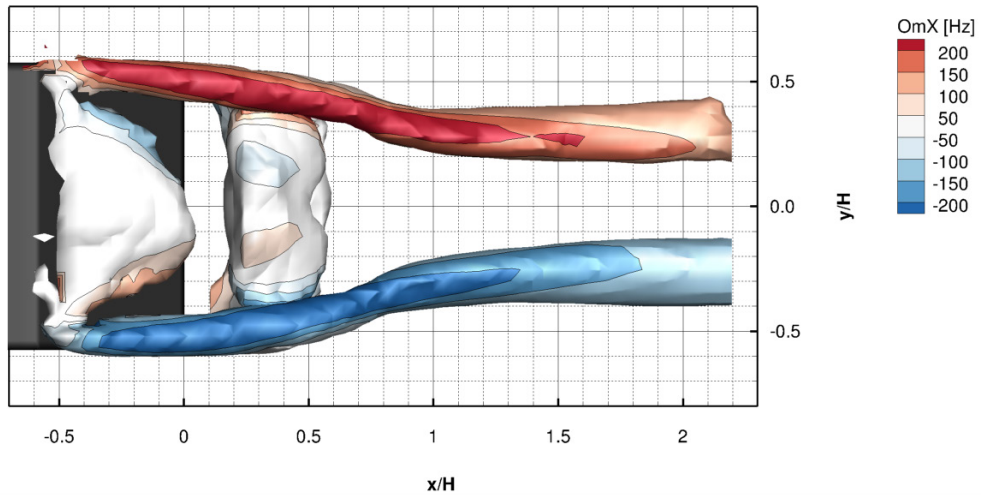
Figure 6.14: Iso-surfaces of Q=4000 s^{-2} coloured by streamwise vorticity ω_x vs β. Top view.

As already seen, by introducing a yaw angle, new flow structures arise as well. If the presence of roof and ground vortices on the side-edges of the model is somehow expected and not difficult to justify, the presence of a strong positive ground vortex trailing the Ahmed body appears as a totally original flow structure, not reported elsewhere and before to the best knowledge of the author. Such ground trailing vortex appears induced by the stronger windward C-pillar vortex and its interaction with both the boundary layer lifting from the ground, behind the wake recirculation bubble and the flow moving downward coming from the slant. For the sake of completeness, a small negative vortex stretching from the lower windward side of the toroidal recirculation vortex must be reported. From figure 6.14, what looks like a perfectly symmetric flow field in absence of yaw (a) begins to present some asymmetries at low cross-wind angles (b). The difference in size between the two C-pillar vortices is already evident, especially downstream the wake recirculation. Moreover, the increased strength of the windward C-pillar can also be inferred by the partial suppression of the slant separation bubble. If the inboard movement of the leeward C-pillar can barely be spotted at low yaw angles (b), it results obvious at $\beta = +8°$ (c). This appears as the result of multiple factors: the increased suction generated by the stronger windward C-pillar vortex,the inwash due to its higher vertical position, a weaker image effect with the ground of the interested vortex due to the lower content of vorticity, the straightening effect of the side walls of the model on the freestream which leaves the model trailing edge in a tangent direction with respect to its side walls and therefore generates a velocity component from the leeward side towards the symmetry plane. As for the recirculation downstream the model, the toroidal vortex appears to slightly move in spanwise direction, possibly moved by the pressure differential between the leeward and windward side. Finally, the already introduced trailing ground vortex generated at high-cross-wind conditions (c) appears to grow while moving downstream, fed by the vorticity of the near co-rotating C-pillar vortex.

6.4.2   C-Pillar Vortices Intensity

The streamwise vorticity peak $\omega_{x,max}$ of the two C-pillar vortices is plotted against the x/H coordinate for the three different cases in figure 6.15. In general, the vorticity content increases during the vortex roll-up and reaches its maximum just downstream the base surface. The vorticity peak then reduces with the same slope until reaching roughly the end of the recirculation bubble. At this point, the C-pillar vortices elongate vertically and the rate of vorticity reduction decreases, with the slope of the curve halving.

By looking at the right vortices (red lines), as expected, the vorticity content increases with increasing the cross-wing angle β. Despite being consistently above the $\beta_{+0°}$ curve, some overlap between the $\beta_{+4°}$ and $\beta_{+8°}$ curves occurs behind x/H=1, where, for the high-cross-wind condition the flowfield is affected by the presence of the trailing ground vortex.

As expected, the opposite occurs with the leeward side (blue lines) and the C-pillar vortices become weaker and weaker with increasing the yaw. The presented data has been evaluated on the three downstream planes proposed by Lienhart & Becker (2003) and, to ease a quantitative analysis, has been reported in table 6.4. In here, the change in vorticity has been referred to the $\beta = 0°$ case. The maximum intensity reduction for the leeward C-pillar is of the order of 9% for the low-cross-wind case while it reaches approximately the 21% for the maximum yaw condition.
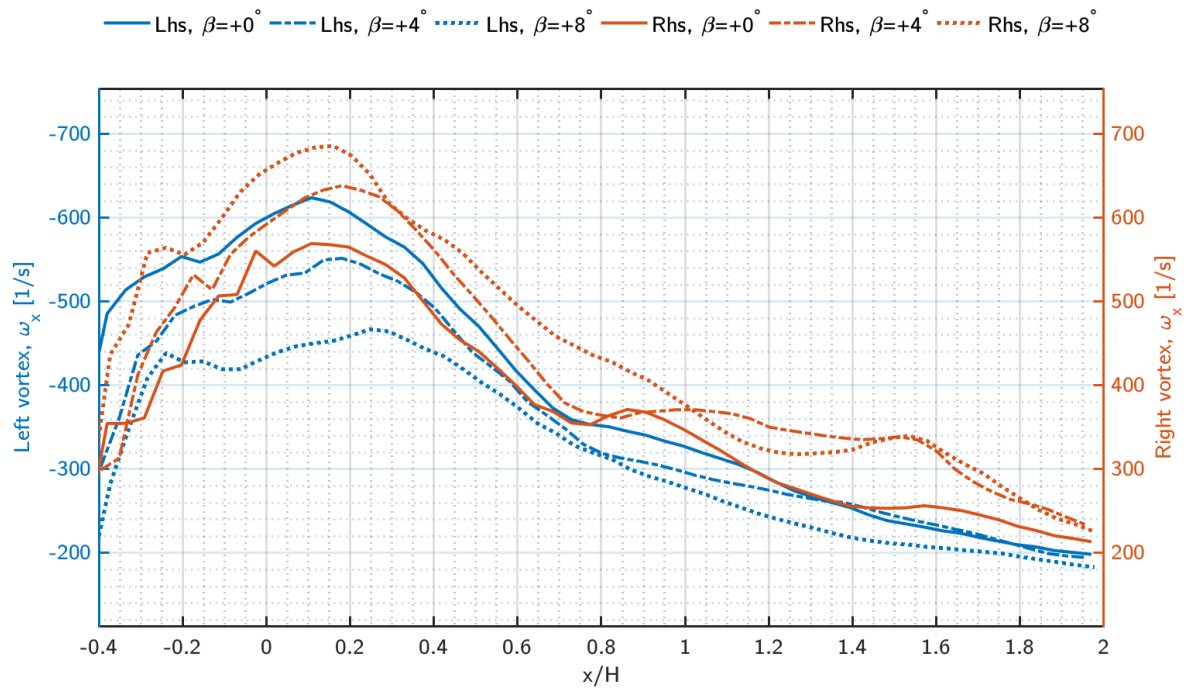
Figure 6.15: Vortices core peak streamwise vorticity $\omega_{x,max}$ with varying cross-wind angle β.

On the other hand, although in near proximity the intensity increase of the windward C-pillar is greater for the high-cross-wind case, far downstream the model the two different cross-wind cases seem to converge towards a similar value of the order of 33%. Remember that, due to the finite bin size, the data presents some modulation and the absolute vorticity values should be regarded as affected as well. Nevertheless, by changing the bin size, the same trends and comparable deltas result.

For the sake of completeness, it must be reported that for the headwind case $\beta = 0°$, the leeward C-pillar looks stronger, especially during the roll-up stage. Although such asymmetry is not evident when looking at the flowfield, see figure 6.14 (a), it may be related to a slightly greater than zero cross-wing angle due to the uncertainty introduced by the manually actuated rotating disk.

6.4.3   C-Pillar Vortices Position

Moving forward with the position of the studied vortices, the core location on the vertical and horizontal planes has been plotted against the x/H coordinate for the three different cases in figure 6.15 (a) and (b), respectively. As expected, again, the windward vortices (red lines) consistently rise with increasing β while, at the same time, the leeward vortices (blue lines) move downward, under the effect of an increased downwash. This downward movement is limited, in a first stage, due to the proximity with the solid slant surface and the wake recirculation, but becomes evident straight after. Moreover, the stronger the vortex, the further away from the surface the core is, due to an already greater diameter of the C-pillar vortex during the roll-up

stage. Moving from the vertical to the horizontal position of the vortices, the characteristic trajectory is immediately appreciable: the vortices roll-up near to the slant side edges and, while convected downstream, they move towards the symmetry plane under the effects of their own low-pressure cores. However, two main trends are inferable which relate to the yaw angle β. The bigger the yaw, the more inboard the windward C-pillar moves. This is due to the higher static pressure on the windward side and to the increased diameter of the vortex, as already said, other than to a small displacement of the slant side edge due to the model rotation. The opposite is true for the leeward C-pillar. On the other hand, although the windward C-pillar does not change its trajectory downstream, with increasing β the leeward vortex consistently moves inboard, under the effect of the suction and the inwash generated by the opposite, higher and stronger vortex.

As done with the vortices intensity, also the displacement has been evaluated on three downstream x/H locations and is presented in table 6.4. In here, it appears that the maximum inboard displacement of the leeward C-pillar vortex is of the order of approximately 10% for the high-crosswind case[4]. For the same vortex and the same case, the maximum vertical displacement is reported of the order of -13% while the windward C-pillar rises above the nominal trajectory as much as approximately the 18% of H.

To conclude the present analysis, although a much more comprehensive parametric study should be carried on to say something about the intensity and position polars of the studied vortices, from the acquired data no linear trend emerges, in agreement, among the other things, with a considerably different flow topology for the high-cross-wind condition.

Table 6.4: Cases comparison, vortices position and intensity with respect to the $\beta = 0°$ case a the three x/H location proposed by Lienhart & Becker (2003). Data binned with binsize $30 \times 30 \times 30$ mm^3

		$\beta = +4°$			$\beta = +8°$		
		Δ_y [%]	Δ_z [%]	Δ_{ω_x} [%]	Δ_y [%]	Δ_z [%]	Δ_{ω_x} [%]
Plane x/H = 0.24	L	+0.1	-1.7	-8.6	+0.3	+1.7	-21.3
	R	-2.8	+4.4	+13.7	-7.8	+9.9	+18.4
Plane x/H = 0.59	L	+0.1	-3.3	-5.0	+1.9	-2.9	-10.2
	R	-2.8	+5.2	+11.7	-7.2	+8.3	+23.8
Plane x/H = 1.48	L	+2.4	-10.2	+3.3	+9.8	-13.2	-11.3
	R	-0.1	+13.3	+33.2	-2.1	+17.8	+32.4

---

[4]Remember the displacement is expressed in percentage of the reference length H.
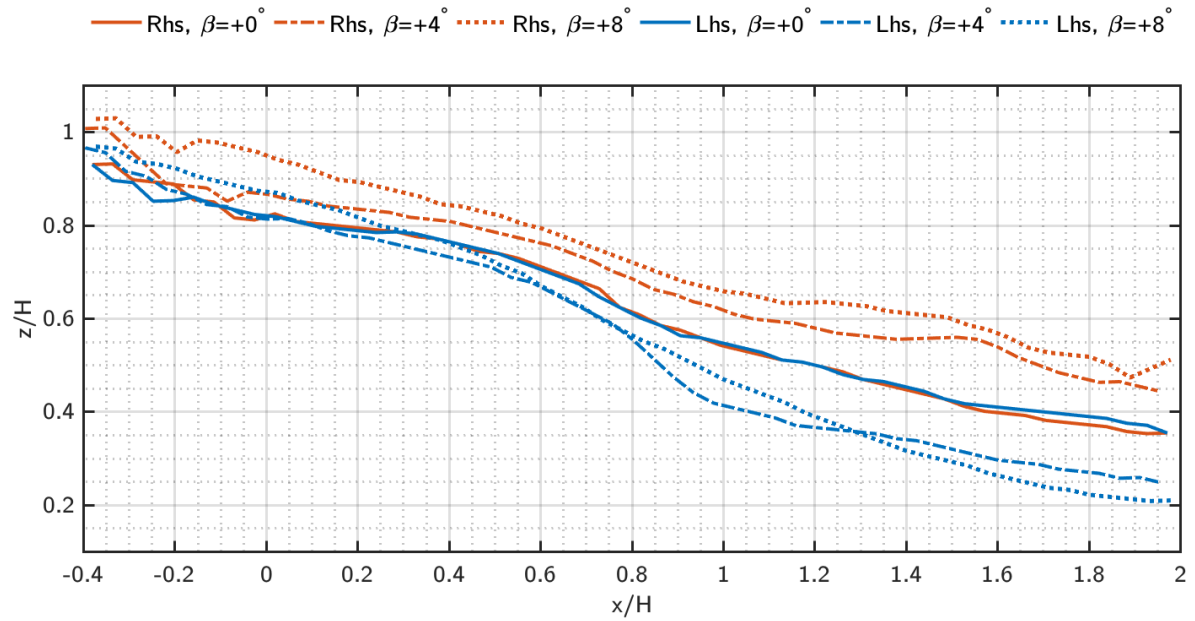
(a)   Side view.
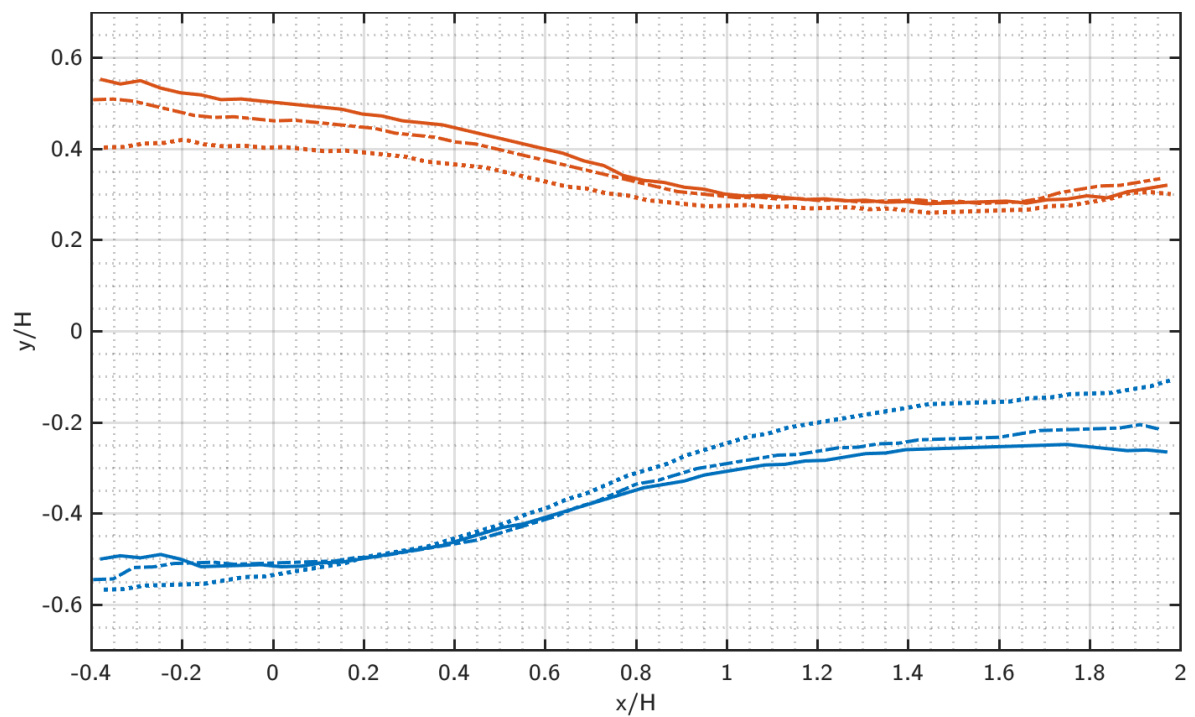
(b)   Top view.

Figure 6.16: Vortices position with varying cross-wind angle β.

6.5   Proposed Flow Topology

A conceptual model for the flow around a $25°$ slant Ahmed body in cross-wind is proposed in figure 6.17. The model covers the roof, the leeward side and the rear of the Ahmed body and it is based both on the present data ($\beta = +8°$) and on those in the literature (dashed lines). The flow separates and reattaches near the roof leading edge, generating a small recirculation bubble. Even though only partial traces of such recirculation are detected with the employed technique[5], both numerical (Krajnovic & Davidson, 2005; Minguez et al., 2008) and experimental investigations (Zhang et al., 2015) have described such structure. For completeness, it has therefore been added to the presented scheme with dashed lines. Similarly, and according once again to the aforementioned literature, another separation bubble is present on the leeward side wall. Being this recirculation slightly thicker, since on a suction side, it is clearly measured by the CVV system and has therefore been sketched with continuous line. Because of the pressure differential between the windward wall (pressure side) and the roof, a positive vortex rolls up from the roof windward side edge over the roof. Similarly, from the roof leeward side edge, a positive vortex emerges due to the pressure differential between the roof and the leeward wall (suction side). The low pressure on the leeward side draws some flow from underneath the model, which generates a strong negative ground vortex. This leeward ground vortex keeps growing close to the lower side edge, fed by the flow coming from underneath the model, until it reaches the rear end of the body and gets advected downstream, realigning with the free stream direction. The windward roof vortex finally reaches the slant area, where it merges with a stronger C-pillar vortex, increased in strength by the augmented static pressure on the windward side wall. The larger and stronger windward C-pillar suppresses the close secondary vortex and reduces the extension of the near slant separation bubble thanks to its increased downwash. On the other side, the positive leeward roof vortex reaches the slant side edge, where a negative C-pillar vortex rolls up, weakened by the decrease in pressure differential between the low-pressure leeward side and the slant surface. Close to the C-pillar, the secondary vortex gains strength and results larger than the one found in headwind condition. Moving downstream, the windward, larger, C-pillar vortex follows a risen trajectory while the leeward one, moves downward, under the effect of an increased induced downwash. Furthermore, the leeward vortex also shifts inboard, moved by the increased low pressure generated by the stronger windward C-pillar and by its inwash, being the two vortices staggered in vertical direction. Due to its increased strength, the windward C-pillar vortex strongly interacts with the floor boundary layer when getting close to the ground. Under the effects of the suction generated by both the recirculation bubble and the C-pillar, part of the boundary layer lifts from the floor and rolls into a positive induced ground vortex. Such structure gets swept outboard by the co-rotating C-pillar vortex and while interacting with it, grows until becoming dominant downstream. As per the toroidal vortex inside the recirculation bubble, it retains its nominal characteristics, slightly moving in spanwise direction towards the low pressure leeward side and stretching in streamwise direction[6] when interacting with the strong and close windward C-pillar vortex.

---

[5]This is most likely due to the proximity with the walls, a limited thickness of the recirculation bubble and a reduced number of acquired samples caused by the absence of measurement overlap.

[6]A small negative vortex arises from the lower windward corner, stretching in streamwise direction.
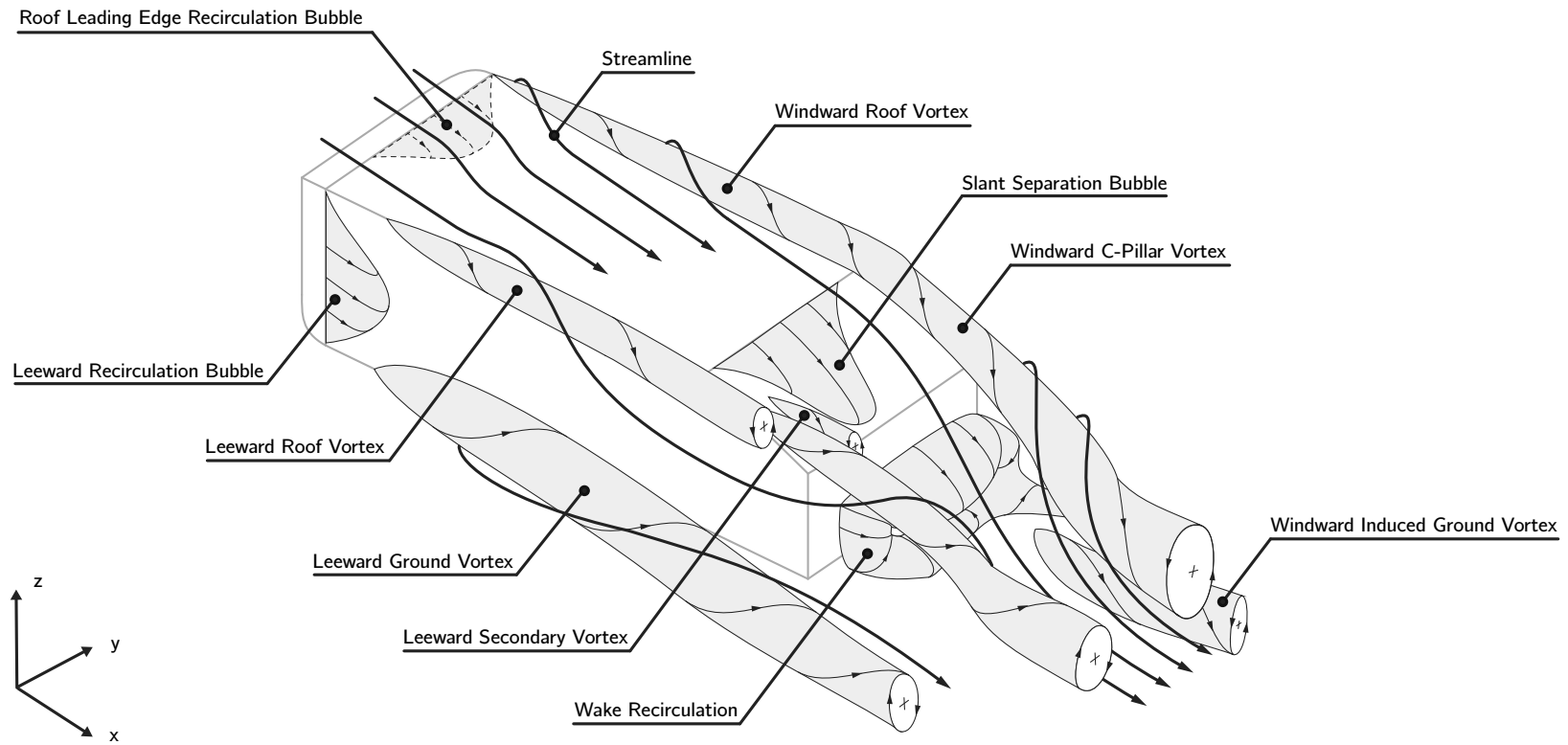
Figure 6.17: Proposed flow topology for a 25-degrees slant Ahmed body in cross-wind ($\beta = +8°$). The light lines on the vortices do represent the vortex rotation while streamlines are represented with bold lines.

7

Conclusions and Recommendations

In this chapter, the findings produced by the present investigations are briefly summarized, with respect both to the Ahmed body flow topology in cross-wind and the performances of the novel experimental technique in use. Following, some recommendations are proposed, which aim at suggesting possible future developments concerning, again, both the Ahmed body and the experimental technique.

Contents

7.1   Conclusions

The near wake of a 25 degrees slant Ahmed body in steady cross-wind has been experimentally investigated by means of a novel measurement technique, namely Robotic Coaxial Volumetric Velocimetry. As introduced in the first chapter, the objective of the present work is twofold: if from one hand it aims at the flowfield characterization for the aforementioned model in presence of a cross-velocity component, from the other hand it proposes to assess the capabilities of the novel measurement technique in use.

With respect to the first topic, the present investigation successfully managed to capture the flowfield differences in the proximity of the studied model under the effect of a steady yaw angle. Particular attention has been paid to the main vortical structures, namely the C-pillar vortices, measuring their variation in position and intensity with increasing the cross-wind angle β. As a result of a yaw angle different from zero, indeed, a pressure differential arises between the two side walls of the Ahmed body. The windward side, manifests an increased static pressure, while the leeward side exhibits a drop in static pressure, in analogy with the pressure and suction sides of a symmetric airfoil at an angle of attack different from zero. The increased static pressure on the windward side increases the strength and the dimension of the windward C-pillar vortex, which raises its trajectory. On the other side, the reduced pressure differential between the leeward wall and the slant surface weakens the leeward C-pillar, which moves downward under the effect of the downwash of the stronger windward C-pillar and shifts its trajectory towards the symmetry plane, drawn inboard by the low pressure and the velocity induced by the other vortex. Under the effect of a yaw angle of 8 degrees, for instance, the windward C-pillar can increase its strength up to approximately 30% the nominal intensity, while, for the same cross-wind condition the leeward C-pillar vortex weakens, loosing roughly 20% of its vorticity content. As expected, new structures arise from the longitudinal edges of the model due to the pressure differential generated by the non-symmetrical flowfield. Furthermore, for the high-cross-wind condition, a ground vortex is induced by the powerful windward C-pillar vortex which strongly interacts with the ground boundary layer and rolls it into a coherent structure. Minor differences, concerning the recirculation bubble behind the model and the slant separation, have been addressed as well. All in all, the present study successfully permitted a first large-scale three-dimensional quantitative mapping of the flowfield around the model in cross-wind, making easy to track every detected structure back to its origin.

As per the technique itself, Robotic CVV has proved to be an extraordinarily powerful investigation tool. Similarly to tomographic PIV, Coaxial Volumetric Velocimetry produces a fully three-dimensional mapping of the investigated volume. Moreover, the use of HFSB as tracer particles, not only considerably increases the characteristic length scale of the measurement volume but, because of the reduced power of the laser, dramatically decreases the reflections due to solid walls. The compactness of the CVV probe and the robotic actuation make it extremely easy to move the system around the investigated object, easily partitioning a very large volume into smaller domains. Being the cameras inside a compact enclosure fixed with respect to each other, indeed, the system relies upon a single optical calibration. This means that between one measurement and another, just a few seconds are necessary to reposition the system, which is then immediately ready to perform the following acquisition, without having to arrange a totally

new setup, as for conventional PIV techniques. A further point of strength of the used system concerns the required processing time for the analysis of the acquired data. Because of the smart Lagrangian particle tracking approach in use, the required computational time drops by roughly two orders of magnitude, being comparable to that of two-dimensional PIV. Not only this allows the user to process the data while performing the experiment, interactively improving the acquisition campaign, but also permits to produce three-dimensional large-scale results in few hours. The very small tomographic aperture which characterizes the optical system increases considerably the visual access, although introducing a significant in-depth uncertainty. Such drawback is, however, successfully mitigated by the use of a smart Lagrangian particle tracking algorithm which exploits time information to improve the system accuracy. As part of the proposed research questions, the performances of the system, in terms of dynamic spatial and velocity range, and its intrusiveness, in terms of velocity and pressure perturbations, have been assessed. For a single measurement, the $\overline{\text{DSR}}$ of the time-averaged results produced by the CVV system is of the order $\mathcal{O}(30)$, based on a bin size of $20 \times 20 \times 20$ mm while, considering the whole measured domain, it increases up to $\mathcal{O}(60)$, approximately. Similarly, with taking into account the limitations posed by the dominant in-depth uncertainty, the $\overline{\text{DVR}}$ is $\sim \mathcal{O}(30)$. Although such numbers do not impress if compared to more conventional PIV techniques, both the dynamic ranges do depend upon the number of particles collected in the measurement bin and, therefore, both the resolutions can be increased by collecting a larger number of samples. Clearly, the need for moving to larger measurement scales required some trade-off, and, the consequential introduction of larger tracer particles, decreased the system resolution. This, for instance, makes the CVV technique less suitable for the resolution of thin boundary layers. As per the aerodynamic intrusiveness, the velocity perturbations induced by the measurement system do fall under 1% at approximately 30 cm of distance from the CVV probe. This still allows measuring a large domain without introducing any relevant interference.

In conclusion, because of all the aforementioned qualities, the Robotic CVV system allowed an unparalleled three-dimensional and large-scale quantitative mapping of the flow around the Ahmed body with introducing an unprecedented ergonomic hardware and software interface.

7.2   Recommendations

Given the successful outcome of the present experimental investigation, different future developments can be thought of. First of all, given the limitations of the present study in terms of boundary layer characterization, a more exhaustive description can be obtained by means of hot-wire anemometry or conventional planar PIV. Furthermore, given the close proximity of some flow structures with the ground, a measurement of the ground boundary layer may be meaningful as well, yielding useful information for CFD correlation purposes. A further improvement with respect to the present experiment could be represented by an additional increase of the measurement volume. Indeed, the movement of the robot base further upstream the model would allow an improved measurement of the flow ahead of the body with a better description of the stagnation area and the recirculation bubbles behind the roof and side walls leading edges. A further movement of the robot base in a specular position with respect to the symmetry plane

would allow a complete mapping of the volume around the model, with the possibility to measure the flow about the windward side as well. Even if no particular flow structures are expected, apart from a roof and a ground vortex rolling up from the longitudinal edges of the side wall, the velocity measurement could prove useful for pressure reconstruction purposes. Another interesting possibility entails the extension of the yaw angle envelope. As the change in strength, position and size of the main flow structures proved not to be linear with varying the cross-wind angle, a further increase in sideslip could modify the proposed flow topology and be, once more, of interest for assessing CFD capabilities for automotive applications. As a side remark, with respect to the yawing movement of the model, the use of a remotely controlled rotating disk together with the use of a balance system could guarantee the perfect alignment with the flow, reducing to the minimum the uncertainty introduced otherwise by the user's manipulation of the circular platform. Clearly, everything just said could be repeated with a different slant angle.

As far as the employed measurement technique is concerned, an immediate improvement could pertain to the data processing and in particular the binning procedure. Analogously to the philosophy adopted by conventional PIV with respect to the consecutive refinement of interrogation windows, a progressive bin size refinement based on the number of particles per bin could be introduced. In so doing, the spatial resolution could be locally increased by means of an automatic mesh refinement algorithm. For a further enhancement of the spatial resolution, more advanced averaging techniques can be introduced, which would produce more accurate results with improving, among the other things, the data extrapolation up to solid walls. Despite the author's inclination to limit the acquired images pre-processing to the bare minimum, a slightly more advanced pre-processing strategy could be thought of. For instance, a moderate normalization procedure has proved to be effective in increasing the number of particles detected nearby the boundaries of the acquisition volume. However, although useful to increase the extension of the measurement as well as the number of the resulting tracks, such operation should be carefully evaluated in order to assess potential drawbacks. Finally, many further improvements are currently underway, among which a more aerodynamic and less intrusive probe housing, an enhanced set of cameras, a larger and more reliable seeder, and a more integrated software interface, just to name few. Robotic CVV is therefore intended to extend its applicability envelope while becoming gradually more suitable for inexperienced users.

Bibliography

Adrian, R. J. (1997). Dynamic ranges of velocity and spatial resolution of particle image ve- locimetry. *Measurement Science and Technology*, *8*(12), 1393.

Agüera, N., Cafiero, G., Astarita, T., & Discetti, T. (2016). Ensemble 3d ptv for high resolution turbulent statistics. *Measurement Science and Technology*, *27*.

Ahmed, S. R., Ramm, G., & Faltin, G. (1984). Some salient features of the time-averaged ground vehicle wake. *SAE Technical Paper no. 840300*.

Aider, J.-L., Beaudoin, J.-F., & Wesfreid, J. E. (2010). Drag and lift reduction of a 3d bluff-body using active vortex generators. *Experiments in Fluids*, *48*(5), 771–789.

Ashton, N., West, A., Lardeau, S., & Revell, A. (2016). Assessment of rans and des methods for realistic automotive models. *Computers and Fluids*, *128*, 1–15.

Aubrun, S., McNally, J., Alvi, F., & Kourta, A. (2011). Separation flow control on a generic ground vehicle using steady microjet arrays. *Experiments in Fluids*, *51*(5), 1177–1187.

Beaudoin, J.-F. & Aider, J.-L. (2008). Drag and lift reduction of a 3d bluff body using flaps. *Experiments in Fluids*, *44*(4), 491–501.

Beaudoin, J.-F., Cadot, O., Aider, J.-L., Gosse, K., Paranthoen, P., Hamelin, B., Tissier, M., Allano, D., Mutabazi, I., Gonzales, M., & Wesfreid, J. E. (2004). Cavitation as a complementary tool for automotive aerodynamics. *Experiments in Fluids*, *37*(5), 763–768.

Caridi, G. C. A., Ragni, D., Sciacchitano, A., & Scarano, F. (2016). Hfsb-seeding for large-scale tomographic piv in wind tunnels. *Experiments in Fluids*, *57*(12), 261.

Elsinga, G. E., Scarano, F., Wieneke, B., & van Oudheusden, B. W. (2006). Tomographic particle image velocimetry. *Experiments in Fluids*, *41*(6), 933–947.

Evrard, A., Cadot, O., Sicot, C., Herbert, V., Ricot, D., & Vigneron, R. (2017). Comparative effects of vortex generators on ahmed's squareback and minivan car models. *Proceedings: Institution of Mechanical Engineers, Part D: Journal of Automobile Engineering*, *231*(9), 1287–1293.

Fares, E. (2006). Unsteady flow simulation of the ahmed reference body using a lattice boltz- mann approach. *Computers and Fluids*, *35*(8-9), 940–950.

Gambuzza, S. (2017). Flow topology around an ahmed body, Master's Thesis, Roma La Sapienza.

Gillieron, P. (1999). Modelling of stationary three-dimensional separated air flows around an ahmed reference model. *In: Third International Workshop on Vortex Flows and Related Numerical Methods*, *7*, 173–182.

Gohlke, M., Beaudoin, J. F., Amielh, M., & Anselmet, F. (2007). Experimental analysis of flow structures and forces on a 3d-bluff-body in constant cross-wind. *Experiments in Fluids*, *43*(4), 579–594.

Grandemange, M., Cadot, O., Courbois, A., Herbert, V., Ricot, D., Ruiz, T., & Vigneron, R. (2015). A study of wake effects on the drag of ahmed's squareback model at the industrial scale. *Journal of Wind Engineering and Industrial Aerodynamics*, *145*, 282–291.

Grandemange, M., Gohlke, M., & Cadot, O. (2013). Turbulent wake past a three-dimensional blunt body. part 1. global modes and bi-stability. *Journal of Fluid Mechanics*, *722*, 51–84.

Guilmineau, E. (2008). Computational study of flow around a simplified car body. *Journal of Wind Engineering and Industrial Aerodynamics*, *96*(6-7), 1207–1217.

Guilmineau, E., Chikhaoui, O., Deng, G., & Visonneau, M. (2013). Cross wind effects on a simplified car model by a des approach. *Computers and Fluids*, *78*, 29–40.

Guilmineau, E., Deng, G., & Wackers, J. (2011). Numerical simulation with a des approach for automotive flows. *Journal of Fluids and Structures*, *27*(5-6), 807–816.

Herman, G. T. & Lent, A. (1976). Iterative reconstruction algorithms. *Computers in biology and medicine*, *4*, 273–294.

Hucho, W. (1978). The aerodynamic drag of cars current understanding, unresolved problems, and future prospects. In G. Sovran, T. Morel, & W. T. J. Mason (Eds.), *Aerodynamic Drag Mechanisms of Bluff Bodies and Road Vehicles* (pp. 7–44). Boston, MA: Springer.

Hucho, W. & Sovran, G. (1993). Aerodynamics of road vehicles. *Annual review of fluid mechanics*, *25*, 485–537.

Hunt, J. C. R., Wray, A. A., & Moin, P. (1988). Eddies, streams, and convergence zones in turbulent flows. *Center for Turbulence Research. Proceeding: Summer Program 1988*, *Report N89-24555*.

Joseph, P., Amandolèse, X., & Aider, J.-L. (2012). Drag reduction on the 25 degrees slant angle ahmed reference body using pulsed jets. *Experiments in Fluids*, *52*(5), 1169–1185.

Jux, C. (2017). Robotic volumetric particle tracking velocimetry by coaxial imaging and illumination, Master's Thesis, TU Delft.

Jux, C., Sciacchitano, A., Schneiders, J. F. G., & Scarano, F. (2017). Full-scale cyclist aerodynamics by coaxial volumetric velocimetry. *Proceedings: 12th Int. Symp. Particle Image Velocimetry, Busan, Republic of Korea.*

Keogh, J., Barber, T., Diasinos, S., & Graham, D. (2016). The aerodynamic effects on a cornering ahmed body. *Journal of Wind Engineering and Industrial Aerodynamics*, *154*, 34–46.

Krajnovic, S. & Davidson, L. (2004). Large-eddy simulation of the flow around simplified car model. *SAE Technical Paper*, *2004-01-0227*.

Krajnovic, S. & Davidson, L. (2005). Flow around a simplified car, part 1: Large eddy simulation. *Journal of Fluids Engineering, Transactions of the ASME*, *127*(5), 907–918.

Lienhart, H. & Becker, S. (2003). Flow and turbulence structure in the wake of a simplified car model. *SAE Technical Paper*, *2003-01-0656*.

Lignarolo, L. E. M., Ragni, D., Krishnaswami, C., & Chen, Q. (2014). Experimental analysis of the wake of a horizontal-axis wind-turbine model. *Renewable Energy*, *70*, 31–46.

Meile, W., Ladinek, T., Brenn, G., Reppenhagen, A., & Fuchs, A. (2016). Non-symmetric bi-stable flow around the ahmed body. *International Journal of Heat and Fluid Flow*, *57*, 34–47.

Minguez, M., Pasquetti, R., & Serre, E. (2008). High-order large-eddy simulation of flow over the "ahmed body" car model. *Physics of Fluids*, *20*(9).

Morel, T. & Sovran, G. (1978). The effect of base slant on the flow pattern and drag of three-dimensional bodies with blunt ends. In G. Sovran, T. Morel, & W. T. J. Mason (Eds.), *Aerodynamic Drag Mechanisms of Bluff Bodies and Road Vehicles* (pp. 191–226). Boston, MA: Springer.

Morias, K. L. L., Caridi, G. C. A., Sciacchitano, A., & Scarano, F. (2016). Statistical characterization of helium-filled soap bubbles tracing fidelity for piv. *Proceeding: 18th International Symposium on Application of Laser and Imaging Techniques to Fluid Mechanics.*, Lisbon, Portugal: Springer.

Pujals, G., Depardon, S., & Cossu, C. (2010). Drag reduction of a 3d bluff body using coherent streamwise streaks. *Experiments in Fluids*, *49*(5), 1085–1094.

Raffel, M., Willert, C. E., Scarano, F., Kähler, C. J., Wereley, S. T., & Kompenhans, J. (2018). *Particle image velocimetry: a practical guide*. Springer International Publishing.

Scarano, F. (2013). Tomographic piv: Principles and practice. *Measurement Science and Technology*, *24*(1).

Scarano, F., Ghaemi, S., Caridi, G. C. A., Bosbach, J., Dierksheide, U., & Sciacchitano, A. (2015). On the use of helium-filled soap bubbles for large-scale tomographic piv in wind tunnel experiments. *Experiments in Fluids*, *56*(2), 159.

Schanz, D., Gesemann, S., & Schröder, A. (2016). Shake-the-box: Lagrangian particle tracking at high particle image densities. *Experiments in Fluids*, *57*(5), 1393.

Schanz, D., Gesemann, S., Schröder, A., & Wienecke, B. (2013). Particle reconstruction with optical transfer functions applied to tomo-piv-experiments. In K. H. N. W. P. I. Dillmann A., Heller G. (Ed.), *New Results in Numerical and Experimental Fluid Mechanics VIII. Notes on Numerical Fluid Mechanics and Multidisciplinary Design, vol 121* (pp. 623–631). Springer, Berlin, Heidelberg.

Schanz, D., Schröder, A., Gesemann, S., Michaelis, D., & Wieneke, B. (2013). Shake the box: A highly efficient and accurate tomographic particle tracking velocimetry (tomo-ptv) method using prediction of particle positions. *Proceedings: 10th International Symposium on Particle Image Velocimetry*, 1–13.

Schneiders, J. F. G. (2017). *Bridging PIV spatial and temporal resolution using governing equations and development of the coaxial volumetric velocimeter*. PhD thesis, TU Delft.

Sciacchitano, A. & Scarano, F. (2014). Elimination of piv light reflections via a temporal high pass filter. *Measurement Science and Technology*, *25*(8), 084009.

Soloff, S. M., Adrian, R. J., & Liu, Z.-C. (1997). Distortion compensation for generalized stereoscopic particle image velocimetry. *Measurement Science and Technology*, *8*(12), 1441.

Sovran, G., Morel, T., & Mason, W. T. J. (1978). Preface. In G. Sovran, T. Morel, & W. T. J. Mason (Eds.), *Aerodynamic Drag Mechanisms of Bluff Bodies and Road Vehicles* (pp. 1–4). Boston, MA: Springer US.

Spohn, A. & Gillieron, P. (2002). Flow separations generated by a simplified geometry of an automotive vehicle. *IUTAM Symposium: Unsteady Separated Flows*.

Strachan, R. K., Knowles, K., & Lawson, N. J. (2007). The vortex structure behind an ahmed reference model in the presence of a moving ground plane. *Experiments in Fluids*, *42*(5), 659–669.

Thacker, A., Aubrun, S., Leroy, A., & Devinant, P. (2012). Effects of suppressing the 3d separation on the rear slant on the flow structures around an ahmed body. *Journal of Wind Engineering and Industrial Aerodynamics*, *107-108*, 237–243.

Tounsi, N., Mestiri, R., Keirsbulck, L., Oualli, H., Hanchi, S., & Aloui, F. (2016). Experimental study of flow control on bluff body using piezoelectric actuators. *Journal of Wind Engineering and Industrial Aerodynamics*, *9*(2), 827–838.

Tunay, T., Sahin, B., & Ozbolat, V. (2014). Effects of rear slant angles on the flow characteristics of ahmed body. *Experimental Thermal and Fluid Science*, *57*, 165–176.

Venning, J., Lo Jacono, D., Burton, D., Thompson, M., & Sheridan, J. (2015). The effect of aspect ratio on the wake of the ahmed body. *Experiments in Fluids*, *56*(6), 126.

Vino, G., Watkins, S., Mousley, P., Watmuff, J., & Prasad, S. (2005). Flow structures in the near-wake of the ahmed model. *Journal of Fluids and Structures*, *20*(5), 673–695.

Wieneke, B. (2008). Volume self-calibration for 3d particle image velocimetry. *Experiments in Fluids*, *45*(4), 549–556.

Wieneke, B. (2013). Iterative reconstruction of volumetric particle distribution. *Measurement Science and Technology*.

Zhang, B. F., Zhou, Y., & To, S. (2015). Unsteady flow structures around a high-drag ahmed body. *Journal of Fluid Mechanics*, *777*, 291–326.

A
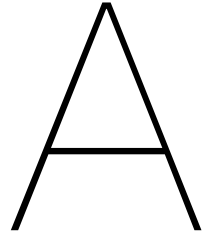
Appendix: Boundary Layer

As introduced in chapter 6, the boundary layer has been evaluated in order to be sure the zigzag trip successfully managed to trigger transition. Because no other technique was available at the time of the experiment, a pitot tube mounted on a traverse system has been used to carry on the measurements.

The boundary layer has been measured on the symmetry plane, 50 mm before the slant leading edge and the results are presented in figure A.1. The experimental data has been fitted through a logarithmic law and the obtained profile has been used for computing the shape factor
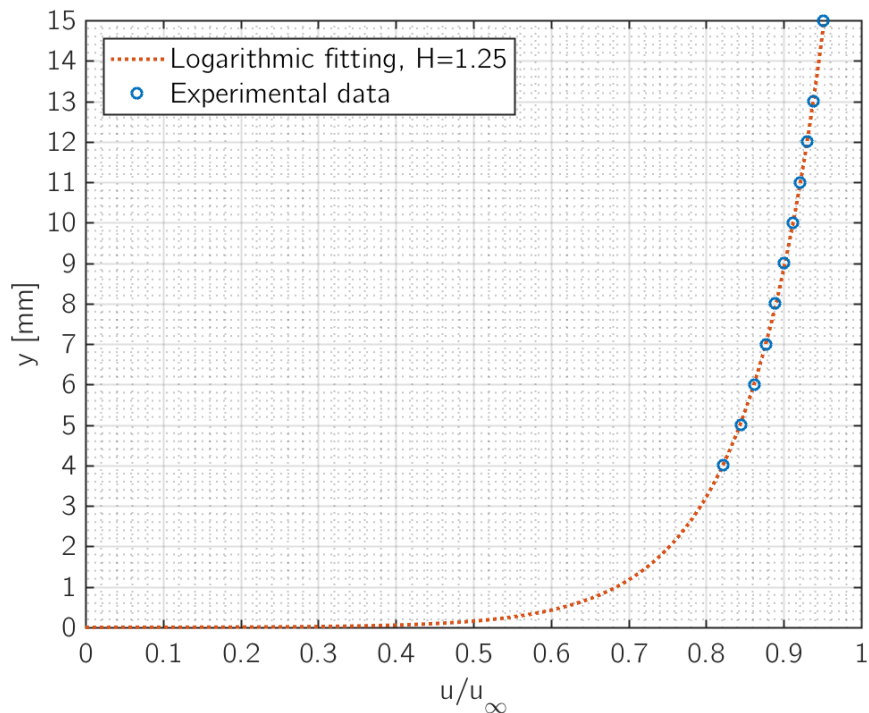
Figure A.1: Boundary layer profile, experimental data and logarithmic fitting.

H_{BL}, defined as

$$H_{BL} = \frac{\delta^*}{\theta} \tag{A.1}$$

being δ^* the displacement thickness, defined as

$$\delta^* = \int_0^\infty \left(1 - \frac{u(y)}{u_\infty}\right) dy \tag{A.2}$$

and θ the momentum thickness, defined as

$$\theta = \int_0^\infty \frac{u(y)}{u_\infty} \left(1 - \frac{u(y)}{u_\infty}\right) dy \tag{A.3}$$

As expected, a fully developed boundary layer resulted, whose thickness and shape factor are $\delta_{.95} = 14.7$ mm and $H_{BL} = 1.25$. These values are in good agreement with the one measured by Gambuzza (2017) for the very same model at the same Reynolds number, although in a different wind tunnel[1]. Moreover, the experimental data acquired for the present experiment do overlap precisely with the velocity profile proposed by Gambuzza (2017). For such experiment, the boundary layer ahead of the slant leading edge has been measured by means of planar PIV and the reported thickness and shape factor resulted $\delta_{.95} = 13.2$ and $H_{BL} = 1.22$, respectively.

However, although the present boundary layer characterization may not be totally satisfactory from a CFD user point of view, it is sufficient to guarantee the present results are not affected by a qualitatively different (i.e. laminar) boundary layer if compared to the rest of the literature.

Finally, as pointed out in the recommendations chapter, a possible future development of the present work should include an improved boundary layer characterization, possibly by means of hot wire or planar PIV measurements.

---

[1]The measurements have been undertaken at the W-Tunnel of the High-speed Lab of TU Delft with a similar measured turbulence intensity, i.e. 1.1%, but a different blockage, namely 7.8%.

B

Appendix: Q-criterion

B.1   Definition

The Q-criterion has been firstly introduced by Hunt et al. (1988) as a possible way to detect a vortex. The authors defined an eddy as the region with positive second invariant Q of the velocity gradient tensor $\boldsymbol{\nabla u}$, with the further requirement of a pressure lower than the free-stream value. Q is defined as

$$Q = \frac{1}{2}\left(||\boldsymbol{\Omega}||^2 - ||\boldsymbol{S}||^2\right) \tag{B.1}$$

where

$$||\boldsymbol{\Omega}|| = [\text{trace}(\boldsymbol{\Omega\Omega}^t)]^{1/2}, \quad ||\boldsymbol{S}|| = [\text{trace}(\boldsymbol{SS}^t)]^{1/2} \tag{B.2}$$

being $\boldsymbol{S}$ and $\boldsymbol{\Omega}$ the symmetric and antisymmetric components of the velocity gradient tensor, respectively, defined as

$$\Omega_{ij} = \frac{1}{2}\left(u_{i,j} - u_{j,i}\right), \quad S_{ij} = \frac{1}{2}\left(u_{i,j} + u_{j,i}\right) \tag{B.3}$$

The second invariant Q, therefore, represents the balance between the shear strain rate and the vorticity magnitude and, when positive, highlights regions where rotation dominates over shear.

B.2   Limitations

An interesting phenomenon occurred while analysing the acquired data. Iso-surfaces of Q-criterion do detect a spanwise coherent structure connecting the two C-pillar vortices, as illustrated in figure B.1 (a). Not only such arc-shaped vortex has never been reported before in the literature but its position appears also suspicious, since not advected downstream by the flow coming from the roof of the model. An inspection of the velocity field on the symmetry plane, sectioning the studied structure, does not highlight any reversed flow in proximity of the vortex nor any velocity deficit. This corroborates the idea of a false positive produced by the Q-criterion failing in detecting an actual vortex under certain conditions.
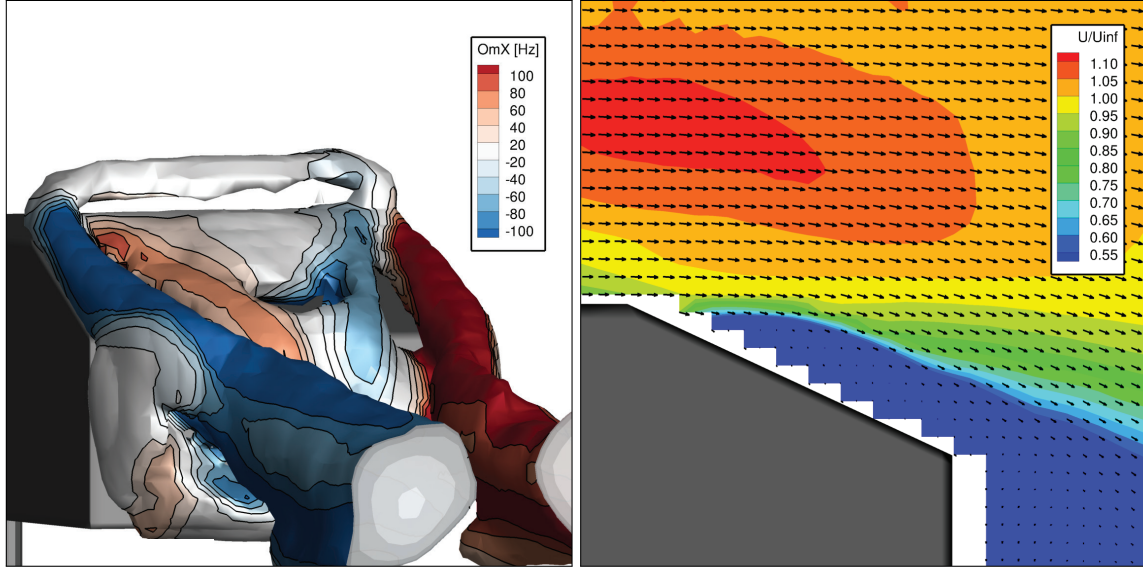
(a) Iso-surfaces of Q=1250 s^{-2}.

(b) Velocity field on the symmetry plane.

Figure B.1: Fictitious coherent structure identified by the Q-criterion between the two C-pillar vortices (a) and velocity field on the symmetry plane which shows no reversed flow in correspondence of the assumed arc vortex (b).

To further dig into this matter, and for the ease of computation, the quasi-two-dimentional flow on the symmetry plane has been investigated by deriving the Q-criterion formula for a 2D flow. Starting from the velocity gradient tensor $\boldsymbol{\nabla u}$ and its decomposition into antisymmetric and symmetric part, $\boldsymbol{\Omega}$ and $\boldsymbol{S}$, respectively,

$$\boldsymbol{\nabla u} = \boldsymbol{\Omega} + \boldsymbol{S} \tag{B.4}$$

or, in expanded form,

$$\begin{pmatrix} \frac{\partial u}{\partial x} & \frac{\partial u}{\partial y} \\ \frac{\partial v}{\partial x} & \frac{\partial v}{\partial y} \end{pmatrix} = \begin{pmatrix} 0 & \frac{1}{2}\left(\frac{\partial u}{\partial y} - \frac{\partial v}{\partial x}\right) \\ \frac{1}{2}\left(\frac{\partial v}{\partial x} - \frac{\partial u}{\partial y}\right) & 0 \end{pmatrix} + \begin{pmatrix} \frac{\partial u}{\partial x} & \frac{1}{2}\left(\frac{\partial u}{\partial y} + \frac{\partial v}{\partial x}\right) \\ \frac{1}{2}\left(\frac{\partial v}{\partial x} + \frac{\partial u}{\partial y}\right) & \frac{\partial v}{\partial y} \end{pmatrix}, \tag{B.5}$$

recalling the definition of Q presented in equation B.1 together with formulas B.2, it results

$$Q = \frac{1}{2}\left[\text{trace}\begin{pmatrix} \frac{1}{4}\left(\frac{\partial u}{\partial y} - \frac{\partial v}{\partial x}\right)^2 & 0 \\ 0 & \frac{1}{4}\left(\frac{\partial v}{\partial x} - \frac{\partial u}{\partial y}\right)^2 \end{pmatrix} + \right.$$

$$\left. -\text{trace}\begin{pmatrix} \left(\frac{\partial u}{\partial x}\right)^2 + \frac{1}{4}\left(\frac{\partial v}{\partial x} + \frac{\partial u}{\partial y}\right)^2 & \frac{1}{2}\left(\frac{\partial u}{\partial y} + \frac{\partial v}{\partial x}\right)\left(\frac{\partial u}{\partial x} + \frac{\partial v}{\partial y}\right) \\ \frac{1}{2}\left(\frac{\partial u}{\partial y} + \frac{\partial v}{\partial x}\right)\left(\frac{\partial u}{\partial x} + \frac{\partial v}{\partial y}\right) & \left(\frac{\partial v}{\partial y}\right)^2 + \frac{1}{4}\left(\frac{\partial v}{\partial x} + \frac{\partial u}{\partial y}\right)^2 \end{pmatrix}\right]$$

which finally yields

$$Q = -\frac{1}{2}\left[\left(\frac{\partial u}{\partial x}\right)^2 + 2\frac{\partial u}{\partial y}\frac{\partial v}{\partial x} + \left(\frac{\partial v}{\partial y}\right)^2\right] \tag{B.6}$$

According to equation B.6, in order for Q to be positive, the double product $2u_y v_x$ must be negative and outweigh the positive contribution of the two squared velocity gradients $(u_x)^2$ and $(v_y)^2$. Before the slant leading edge, near the wall, u_y is expected to be positive, since describing the boundary layer velocity profile. As per v_x, usually negligible near a straight horizontal wall, after the slant leading edge it is actually expected to become negative, because of the downwash of the vortices and the flow curving downward. This can be confirmed by looking at figure B.2, where the aforementioned quantities have been plotted on the symmetry plane. By plotting the
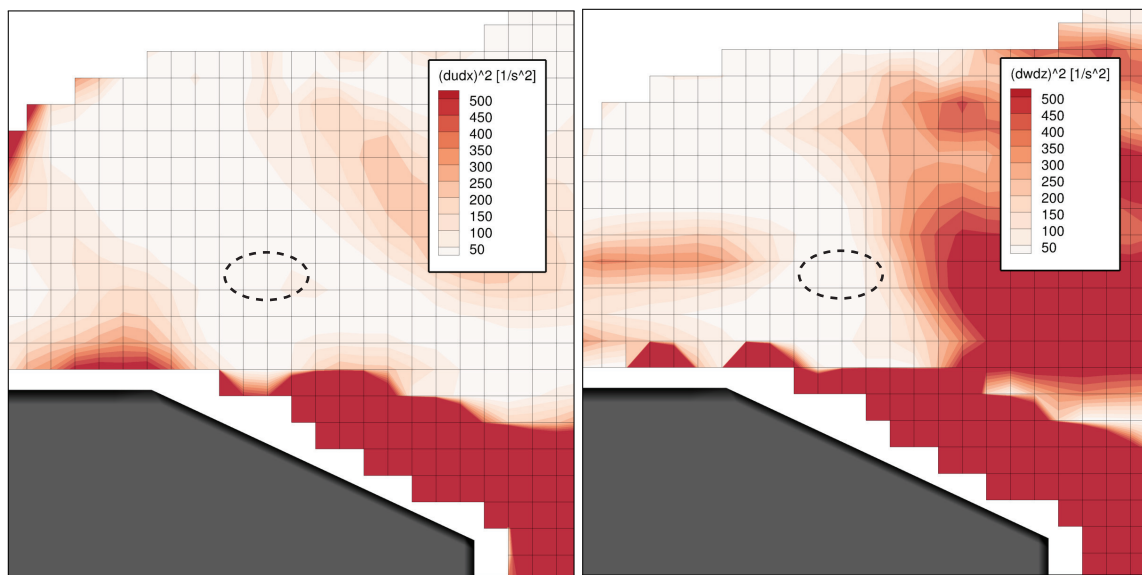
(a) $(\frac{\partial u}{\partial x})^2$ (or $(\frac{\partial u}{\partial x})^2$ in the 3D reference system). (b) $(\frac{\partial v}{\partial y})^2$ (or $(\frac{\partial w}{\partial z})^2$ in the 3D reference system).
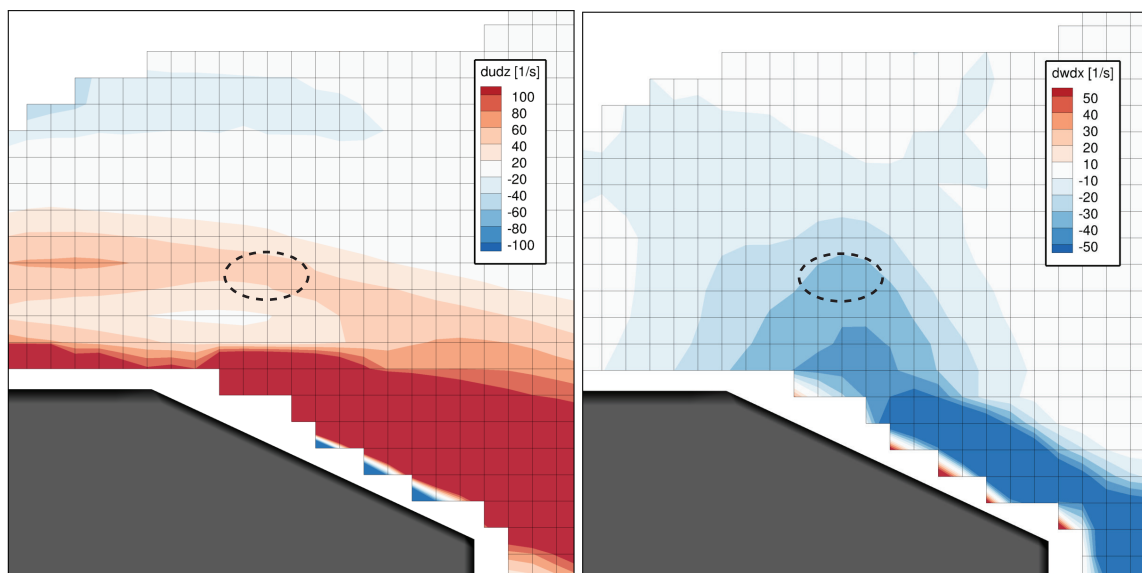
(c) $\frac{\partial u}{\partial y}$ (or $\frac{\partial u}{\partial z}$ in the 3D reference system). (d) $\frac{\partial v}{\partial x}$ (or $\frac{\partial w}{\partial x}$ in the 3D reference system).

Figure B.2: Velocity gradients on the symmetry plane. Fictitious vortex area is highlighted with dashed line.

remaining two squared velocity gradients of equation B.6, namely $(u_x)^2$ and $(v_y)^2$, they have been found rather homogeneous above the model upper surface and never exceeding $+100 \; s^{-2}$ in the proximity of the vortex. The double product $2u_y v_x$, instead, can be as low as $-2500 \; s^{-2}$ in the proximity of the fictitious arc vortex, outweighing the two aforementioned squared gradients and yielding therefore a positive Q, despite no recirculation is present.

It therefore appears that, with the right combination of flow deflection in presence of a boundary layer gradient, the second invariant of the velocity gradient tensor may not be a reliable criterion for vortex detection (q.e.d.).